ABSTRACT

Title of dissertation: MATERIALS FOR LARGE-AREA ELECTRONICS: CHARACTERIZATION OF PENTACENE AND GRAPHENE THIN FILMS BY AC TRANSPORT, RAMAN SPECTROSCOPY, AND OPTICS

Daniel Roy Lenski, Doctor of Philosophy, 2010

Dissertation directed by: Professor Michael S. Fuhrer, Department of Physics

This dissertation explores techniques for fabricating and characterizing two classes of novel materials which may be useful for large-area electronics applications: organic semiconductors and graphene.

Organic semiconductors show promise for large-area electronics because of their low cost, compatibility with a variety of substrates, and relative ease of fabricating and patterning thin-film transistors (TFTs). Nearly all published work has focused on the dc electronic transport properties of these materials, rather than their ac behavior, which could be affected by their polycrystalline, granular structure. To address this, I have constructed a model of organic TFTs based on lossy transmission lines, and determined

the relationship between the film conductivity and the overall device behavior for a bottom-contacted TFT.

I apply this transmission-line framework to interpret my experiments on pentacene TFTs designed in a special long-channel geometry to hasten the onset of high-frequency effects. The experiments reveal an intrinsic frequency-dependent conductivity of polycrystalline pentacene, which can be understood within the context of the universal dielectric response model of ac conduction in disordered solids. The results are important for establishing practical limits on pentacene's ac performance.

Graphene is a two-dimensional crystalline form of carbon, with a remarkably simple structure. It is a gapless semiconductor with an extremely high mobility and very high optical transparency, attracting great interest both for its possible uses as a replacement for silicon and as a transparent conducting material.

I have synthesized large-area films of graphene via atmospheric-pressure chemical vapor deposition (CVD) on copper substrates, adapting a low-pressure CVD method previously reported to produce exclusively monolayer graphene films. I have transferred the graphene films to insulating SiO_2, and characterized them using optical transparency, Raman spectroscopy, and atomic-force microscopy, observing significant differences from the measured properties of widely studied mechanically-exfoliated graphene. I analyze the strengths and weaknesses of these three techniques for distinguishing films of different layer number, and relate them to uncertainties in the known properties of one- and few-layer graphene. I conclude that atmospheric-pressure CVD of graphene on copper produces significant areas of multilayer, rotationally-misoriented graphene, in a significant departure from results on low-pressure CVD of graphene on copper.

MATERIALS FOR LARGE-AREA ELECTRONICS: CHARACTERIZATION OF PENTACENE AND GRAPHENE THIN FILMS BY AC TRANSPORT, RAMAN SPECTROSCOPY, AND OPTICS

by

Daniel Roy Lenski

Dissertation submitted to the Faculty of the Graduate School of the
University of Maryland, College Park, in partial fulfillment
of the requirements for the degree of
Doctor of Philosophy
2010

Advisory Committee:

Professor Michael S. Fuhrer, Chair
Professor Steven Anlage
Dr. William Cullen, Research Scientist
Professor John Cumings
Professor Neil Goldsman

Acknowledgments

First, I am grateful to my advisor, Professor Michael Fuhrer, for his incredible patience, support, and insight over the years I have spent in his research group. When I have been totally stumped or stuck, and there have been many times, he has always been able to suggest new avenues of research, new experiments, new ideas to think about, and new people to talk to. He has a vast and detailed understanding of physics, and he has helped me enormously to become a better and more careful thinker, writer, and presenter.

I could not have done my research without the help of so many members of our group here at Maryland. My thoughts go back to those who helped me in the earliest days after I first showed up in the lab, totally clueless. Stephanie Getty, Yung-Fu Chen, Tobias Dürkop, Gokhan Esen, Anthony Ayari, Enrique Cobas, and above all Todd Brintlinger were incredibly patient and willing to share their time and expertise to teach me many of the basic experimental techniques used in nanoelectronics research.

I worked with Brad Conrad and Adrian Southard extensively over the years, as our research on organic electronics materials frequently overlapped. We shared many long discussions on our work, gave each other ideas, and both of them helped me with sample preparation and other experimental methods. More than that even, I am extremely grateful to them for providing me with real, live examples of how to struggle to understand such fast-moving and complex research, and to persevere in it.

More recently, Alexandra Curtin has spent many hours (and saved me even more) sharing her expertise in atomic force microscopy, which has been a crucial tool for me. I

am lucky not to have been the first graduate student in the group to work on graphene, but to have benefited hugely from those who had a head start. Sung Jae Cho taught me the basics of Raman microscopy, another tool that has been critical in this research, and I have learned from the expertise of Chaun Jang and Shudong Xiao as well. Jianhao Chen has always been easy to talk to, full of insight and knowledge about graphene, ready to share samples and data with me, and an outstanding example of hard work and great thinking. Samitha Kulathunga, an undergrad who worked with me for two summers, helped me a lot in fine-tuning the CVD growth process for graphene.

I am very grateful to Professor John Cumings, who has given me helpful advice and ideas for graphene research, and to his student Kamal Baloch, who has not only been a great friend and a fascinating person to talk to, but has spent a lot of time (including several late nights!) working with me on transmission electron microscopy of graphene.

So many of the other denizens of the group and university have made this a fun, interesting place to work—whether with their advice and help in the lab or just a good, distracting conversation about politics, bikes, science, or the best place to get a beer in whichever city the APS March Meeting was held—including Bill Cullen, Masa Ishigami, Michelle Groce, Kristen Burson, Andrew Tunnell, Jake Tosado, and Norvik Voskanian.

I also want to thank Dr. Tom Clinton and Dr. Werner Scholz, who taught a summer class in data storage technology at Georgetown, nominated me for an internship with Seagate Technology in Pittsburgh in Summer 2008, and served as my mentors there. I had a fantastic and productive time, and learned a lot about magnetic physics and materials. The experience helped me decide where I wanted to go with my career.

The most unexpected lesson I have learned from getting my Ph.D. in physics is that I am much more of a “people person” than I realized before. I would have given up without the support and inspiration of so many friends in the DC area and beyond. Tracy Moore has been a great friend and a colleague literally since the day we both moved here for grad school. Tauno Palomaki (also in physics), Rachel Cook, Carrie Soltanoff, Payam Delgoshaei, Briana Dukas, Nathan Smoot, and Alexandra Hoff have all somehow managed to live with me and yet to remain very good friends. Mariel Kerr has given me more trustworthy and thought-provoking insight and advice than anyone else for many years. Rob Morris has shared lots of good times and introduced me to some truly fascinating people, including Jon Clark and Decker Ringo. All of us have had a blast making short movies in the 48 Hour Film Project’s weekend-long sprints. Summer Saraf gave me friendship and a shining example of the excitement and fun of being a scientist at a crucial point for me in graduate school. Friends from home and college, including Mark Tarquini, Colin Stynes, Dan Jones, the Sendiches, Natalia Wilczek, Amy Ruszkiewicz, and Laura Reis, have provided lots of fun escapes and visits over the years.

Finally, I want to thank my family. My grandfathers, Arny and Artie, got me hooked on physics and math at a young age and have inspired me ever since. My parents, Richard and Madeleine, have done the most maddening, endless, and invaluable thing for me: throughout my whole life, they have set such a good example for me, one which I’ve never been able to ignore for long. Along with my sisters Shoshannah and Natalie, they have always believed in me, even when they probably shouldn’t have, and asked me all the right questions, even when I haven’t wanted to answer.

Table of Contents

Abstract.....
Acknowledgments.....ii
Table of Contents.....v
List of Figures.....viii
1. Transport and device structure of organic semiconductors.....1
1.1 Motivation.....1
1.2 Organic semiconductors.....1
1.3 Field-effect transistors.....2
1.3.1 Metal-oxide-semiconductor FET.....3
1.4 MOSFET circuit model.....5
1.4.1 Field-effect mobility.....5
1.4.2 Quadratic MOSFET model.....7
1.4.3 Saturation.....9
1.5 Application to organic thin-film transistors.....12
1.6 Pentacene.....15
1.6.1 Deposition.....16
1.6.2 Film morphology.....17
1.6.3 Effects of temperature and impurities on film morphology.....20
1.6.4 Effects of substrate.....23
1.7 Charge transport in organic thin films.....24
1.7.1 Thermally-activated hopping.....25
1.7.2 Other models of conduction.....29
1.8 Conclusions.....29
1.9 Structure of this dissertation.....30
2. Measuring the ac transport properties of pentacene.....33
2.1 Motivation.....33
2.2 Transmission line model.....34
2.2.1 Semi-infinite RC transmission line.....36
2.2.2 Finite transmission line.....38
2.2.3 Limiting cases of finite-length transmission line.....40
2.2.4 Expected device behavior.....41
2.3 Devices studied.....43
2.4 Measurement setup.....43
2.5 Results of transmission-line measurements.....48
2.6 Possible explanations for the discrepancies.....51
2.6.1 Contact resistance.....53
2.6.2 Frequency-dependent contact impedance.....54
2.6.3 Interface-trap capacitance.....56
2.7 Generalization of transmission-line model.....57
2.7.1 Extraction of complex conductivity.....58

2.7.2 Description of results....61
2.8 Theoretical explanations....63
2.8.1 Universal dielectric response....64
2.8.2 Applying UDR to my data on pentacene....68
2.9 Implications for practical applications....73
2.10 Conclusions and Future Work....74
2.10.1 Measurement technique....74
2.10.2 Frequency-dependent conductivity of pentacene....75
3. Introduction to graphene....78
3.1 Motivation....78
3.2 The structure of graphene....78
3.3 Electronic properties of graphene....79
3.3.1 High mobility, zero-gap semiconductor....82
3.4 Band gap engineering....85
3.4.1 Graphene nanoribbons....86
3.4.2 Bilayer graphene in a non-uniform electric field....87
3.5 Optical properties of graphene....91
3.6 Raman spectroscopy of graphene....92
3.6.1 Basics of Raman spectroscopy....92
3.6.2 Raman modes of graphene....93
3.7 Graphene synthesis methods....97
3.7.1 Mechanical exfoliation....98
3.7.2 Unzipping carbon nanotubes....99
3.7.3 Graphene nanoribbons from chemical precursors....100
3.7.4 Epitaxial growth on silicon carbide....100
3.8 Chemical vapor deposition of graphene....103
3.8.1 Formation of graphene on nickel and copper....105
3.9 My graphene CVD growth techniques....109
3.9.1 On thin films of nickel....109
3.9.2 On copper foils....114
4. Optical properties of graphene....119
4.1 History....119
4.2 Quantitative model....120
4.2.1 Transfer-matrix method....121
4.3 Application to graphene....126
4.4 Sources of error in optical contrast measurements....129
4.4.1 Non-normal incidence of light....130
4.4.2 Finite light source bandwidth....131
4.4.3 Measuring the index of refraction of graphene....132
4.5 Measuring the thickness of multilayer graphene....135
4.5.1 Dependence on oxide thickness....135
4.5.2 Change in contrast due to additional graphene layers....137
4.6 Measuring the optical contrast of CVD-grown graphene....142
4.6.1 Image acquisition....143

4.6.2 Optical contrast data....144
4.6.3 Possible effect of impurities on graphene contrast....151
4.7 Conclusions....155
5. Raman and atomic force microscopy study of CVD-grown graphene....157
5.1 Motivation....157
5.2 Raman D and 2D modes....158
5.3 Raman on CVD-grown graphene....161
5.4 Evidence for misoriented multilayers....167
5.4.1 Similar results in other forms of graphene....170
5.5 Atomic force microscopy....171
5.5.1 Caveats for graphene....171
5.5.2 Graphene steps....172
5.6 Conclusions....174
5.7 Future work....175
5.8 Raman data summary....177
Glossary of acronyms....178
Bibliography....179
Daniel R. Lenski....190

List of Figures

Figure 1.1....3
Figure 1.2....4
Figure 1.3....9
Figure 1.4....11
Figure 1.5....14
Figure 1.6....15
Figure 1.7....17
Figure 1.8....18
Figure 1.9....20
Figure 1.10....21
Figure 1.11....22
Figure 1.12....28
Figure 2.1....35
Figure 2.2....35
Figure 2.3....37
Figure 2.4....42
Figure 2.5....46
Figure 2.6....47
Figure 2.7....49
Figure 2.8....50
Figure 2.9....52
Figure 2.10....54
Figure 2.11....61
Figure 2.12....63
Figure 2.13....67
Figure 2.14....69
Figure 2.15....70
Figure 2.16....72
Figure 3.1....79
Figure 3.2....81
Figure 3.3....85
Figure 3.4....86
Figure 3.5....88
Figure 3.6....90
Figure 3.7....95
Figure 3.8....97
Figure 3.9....102
Figure 3.10....106
Figure 3.11....109
Figure 3.12....111

Figure 3.13....113
Figure 3.14....117
Figure 4.1....120
Figure 4.2....121
Figure 4.3....122
Figure 4.4....123
Figure 4.5....126
Figure 4.6....128
Figure 4.7....129
Figure 4.8....132
Figure 4.9....133
Figure 4.10....136
Figure 4.11....141
Figure 4.12....143
Figure 4.13....146
Figure 4.14....148
Figure 4.15....150
Figure 4.16....152
Figure 4.17....154
Figure 5.1....159
Figure 5.2....162
Figure 5.3....164
Figure 5.4....166
Figure 5.5....168
Figure 5.6....169
Figure 5.7....173

Note on figures: I produced most of my line and point graphs using Scientific Python and Matplotlib. I drew all of my circuit diagrams and other schematic illustrations using the Inkscape vector graphics editor.

1. Transport and device structure of organic semiconductors

1.1 Motivation

In this chapter, I will introduce organic thin-film transistors (TFTs), the type of device on which my research has been focused, and their similarities to and differences from conventional metal-oxide-semiconductor field-effect transistors (MOSFETs). Organic semiconductors resemble conventional inorganic semiconductors (such as silicon) in some of their bulk electrical properties, although the microscopic origins of their charge transport may be very different, as I discuss below in Section 1.7.

In the latter part of this chapter, I will focus on methods for fabricating organic thin-film transistors using pentacene, which is a particularly well-studied and high-performance organic semiconductor, whose ac transport properties I will investigate in Chapter 2.

1.2 Organic semiconductors

Organic semiconductors are carbon-based materials with semiconducting properties; their conductivity can be adjusted by application of an external electric field, and for some materials by exposure to light.

Organic semiconductors can be divided into two major classes based on the size of the constituent molecules. The first, termed small-molecule semiconductors, comprises van der Waals-bonded solids of small organic molecules. Examples of small-molecule semiconductors include polycyclic aromatic hydrocarbons such as tetracene,

pentacene, and rubrene; short oligomers such as sexithiophene; and fullerenes, such as C_{60}. All of these may be chemically modified with various functional groups to modify their properties such as solubility or reactivity. The second class, polymer semiconductors, comprises solids formed from long-chain organic molecules. Examples include polyacetylene, polyaniline, and poly(3-hexylthiophene).

While inorganic semiconductors such as silicon are covalently bonded crystals, organic semiconductors are typically molecular crystals held together by much weaker van der Waals bonds. Extended forms of covalently-bonded graphitic carbon, such as graphene or carbon nanotubes, are not typically considered organic semiconductors.

1.3 Field-effect transistors

Organic thin-film transistors, such as those on which I will focus in Chapter 2, belong to the class of semiconductor devices known as field-effect transistors (FETs). Broadly, these are devices in which the semiconductor channel is capacitively coupled to a gate electrode, and the gate electric field controls the conductivity of the channel.

Field-effect transistors are useful both as analog amplifiers and as switching elements in digital circuits. In digital applications, field-effect transistors function as voltage-controlled switches, conceptually equivalent to electromechanical relays, which are much slower and larger but were used for similar purposes in the earliest digital computers. Figure 1.1 shows an enhancement-mode *n*-channel FET and a normally-open single-pole single-throw relay side-by-side. For either device, the resistance R_{BC} will be nearly infinite when $V_{AC}=0$ (open switch), but application of a sufficient positive

voltage V_{AC} will result in a very low R_{BC}. Realistic FETs and relays will differ vastly in power consumption, switching speed, and physical size, however.

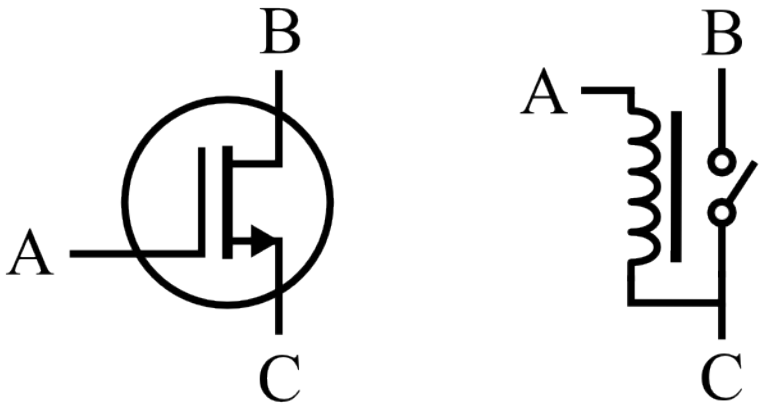

Figure 1.1: An enhancement-mode n-channel field-effect transistor (left) and a normally-open single-pole single-throw relay (right) serve very similar functions as digital circuit elements.

Since the late 1970s, FET-based digital integrated circuits have almost totally supplanted older designs based on bipolar junction transistors (BJTs), because FETs can achieve much lower power usage and heat dissipation. In particular, complementary metal-oxide-semiconductor (CMOS) logic pairs *n*-channel and *p*-channel FETs in such a way that one device is always configured as a closed switch while the other is an open switch. In CMOS circuits, nearly zero current flows except when switching from one state to another.

1.3.1 Metal-oxide-semiconductor FET

Figure 1.2 shows the cross-section of an enhancement-mode, *n*-channel metal-oxide-semiconductor (NMOS) FET, perhaps the archetypal example of a field-effect

transistor. This device consists of a *p*-doped silicon substrate, in which are embedded two highly *n*-doped regions, which are contacted via the external metal electrodes, termed source and drain (they are symmetrical and interchangeable in most designs). The third electrode, termed the gate, sits above the *p*-doped channel which lies between the source and drain regions; the gate electrode, however, is separated from the silicon by a thin layer of non-conducting, dielectric silicon dioxide (SiO_2). A fourth electrode, usually termed body or substrate, may be present, and sets the voltage reference with respect to which the source, gate, and drain biases are applied. In the three-terminal devices which I will discuss in this thesis, the voltages are instead referenced to the source electrode.

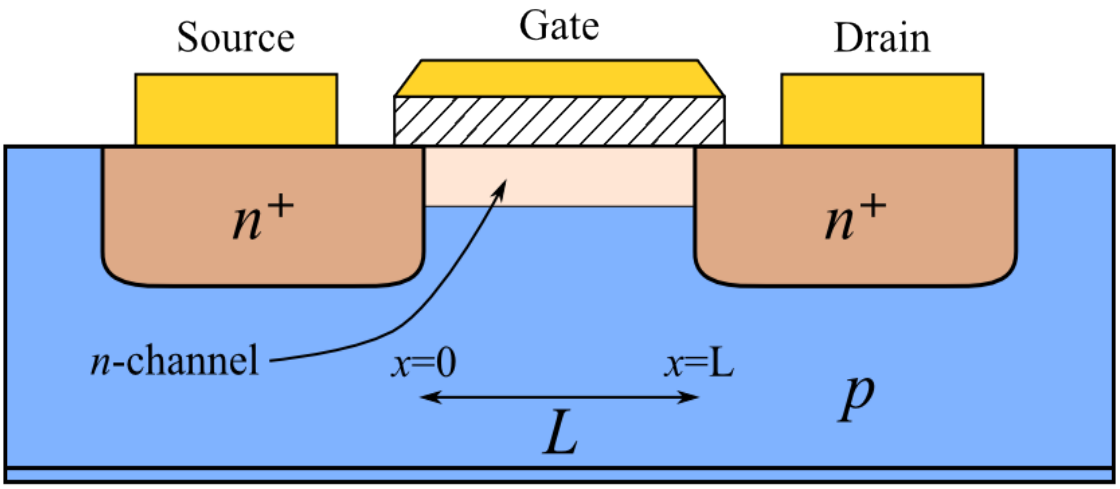

Figure 1.2: Cross-sectional diagram of an enhancement-mode n-channel MOSFET, indicating doping of substrate, source, and drain regions. The light red area underneath the gate oxide (diagonal lines) indicates the region where the n-type conducting channel forms in the presence of a positive gate bias.

In the absence of a gate-source voltage, $V_{GS}=0$ (or equivalently $V_{GD}=0$), very little current can flow between the source and drain contacts, because there are few *n*-

type carriers (electrons) in the *p*-doped substrate. When a positive gate-source voltage is applied, the gate electrode is capacitively coupled to the silicon below it. As V_{GS} is increased, *p*-type carriers (holes) are depleted from this channel region, and with further increase significant numbers of *n*-type carriers are available in the channel. Once $V_{GS} > V_T$, where V_T is termed the threshold voltage, *n*-type carriers are in the majority in this inversion layer, and the conductivity between source and drain is greatly increased.

1.4 MOSFET circuit model

The circuit behavior of an ideal MOSFET can be described in terms of the flow of free carriers in the semiconductor channel, and the effect of gate-source and drain-source bias voltages on the density and velocity of these carriers. Before deriving this model, I will introduce mobility, which is used to characterize the macroscopic behavior of field-effect transistors.

1.4.1 Field-effect mobility

The field-effect mobility is a commonly used figure of merit for field-effect transistors. Its definition assumes a linear relationship between electric field and majority carrier drift velocity, without reference to the possible microscopic origins of this relationship.

Whereas conductivity, σ, expresses the ratio of applied electric field, $\boldsymbol{E}$, to current density, $\boldsymbol{J}$, mobility, μ, expresses the ratio of applied electric field to majority carrier drift velocity, $\boldsymbol{v}$:

$$\boldsymbol{J} = \sigma \boldsymbol{E}$$
$$\boldsymbol{v}_d = \mu \boldsymbol{E} \tag{1.1}$$

In the case of "ordinary" unipolar semiconductors with electrons or holes as the charge carriers ($q = \pm e$), the mobility is related to the conductivity by:

$$\sigma = n e \mu \tag{1.2}$$

where n is the number density of carriers. The mobility is thus the conductivity normalized by the charge density of carriers. Since carrier density can be tuned by varying the FET's gate voltage, within limits imposed by the breakdown strength of the gate dielectric as well as the semiconductor itself, the mobility gives a sense of the performance of a semiconductor device independent of the adjustable carrier density.

While the SI units of mobility are $m^2/V{\cdot}s$, those of $cm^2/V{\cdot}s$ ($=10^{-4}$ $m^2/V{\cdot}s$) are more commonly encountered in the literature. Mobility of commercial crystalline silicon varies based on doping, but room-temperature values are around $\underline{\mu_e}$=1400 $cm^2/V{\cdot}s$ (for electrons) and $\underline{\mu_h}$=450 $cm^2/V{\cdot}s$ (for holes) at optimal doping levels [1]. Novel carbon-based semiconductors such as carbon nanotubes ($\underline{\mu}=10^5$ $cm^2/V{\cdot}s$ reported at room temperature [2]) and graphene ($\underline{\mu}=1.2\times10^5$ $cm^2/V{\cdot}s$ reported at 240 K [3]) offer extremely high mobilities. Organic semiconductors typically have much, much lower mobilities, with typical room-temperature values in the range of 10^{-4}-10^0 $cm^2/V{\cdot}s$ for polymers and 10^{-2}-10^1 $cm^2/V{\cdot}s$ for small-molecule semiconductors. These latter are comparable to amorphous silicon, with room-temperature mobility in the range of 10^0-10^1 $cm^2/V{\cdot}s$.

Mobility is closely related to the rate at which a field-effect transistor can switch the direction of current flow. For a semiconductor with a channel length L, it takes time $t = L/v_d$ for current to traverse the channel. If bias voltage across the length of the

channel is limited to $\pm V$, $|E| \leq V/L$, and thus $v_d \leq \mu V/L$. This gives an upper bound on the frequency with which an FET can switch current flow completely back-and-forth:

$$f = \frac{1}{2t} \leq \frac{\mu V}{2L^2} \tag{1.3}$$

1.4.2 Quadratic MOSFET model

The quadratic model of a MOSFET explains its behavior as a circuit element, in the regime where the gate voltage is large enough to produce charge inversion in the semiconductor channel. For an *n*-channel MOSFET, for example, the channel is dominated by *n*-type carriers and this model neglects the *p*-type carriers; the quadratic model does not describe sub-threshold behavior. The derivation that follows is adapted from that of Bart van Zeghbroeck's *Principles of Semiconductor Devices* [4].

Consider an *n*-channel MOSFET with a channel having a rectangular cross section with width *W* and length *L*, such as that depicted in Figure 1.2. First, the equilibrium current that flows between the source and drain of a MOSFET is straightforwardly given by the total charge of free carriers in the channel, divided by the time that it takes them to traverse the channel:

$$I_D = \frac{q_{inv}}{t_r} \tag{1.4}$$

Here, q_{inv} represents the total free charge in the inversion layer. The simplest model of MOSFET behavior (the linear model, see Section 7.3.1 of [4]) assumes this charge to be uniformly distributed throughout the channel. However, in a real MOSFET this is clearly not the case: the charges in the inversion layer are produced by the capacitive coupling of the gate electrode to the channel. As the voltage along the channel

varies from V_D to V_S, the voltage across the gate dielectric varies from V_{GD} at the drain end to V_{GS} at the source end, and thus the inversion layer charge density varies accordingly. Taking into account the threshold voltage (discussed in Section 1.4.2) beyond which changes in gate voltage affect the charge density,

$$Q_{inv}(x)=C_g(V_G-V_T-V(x)) \tag{1.5}$$

Here C_g is the capacitance per unit area of the gate dielectric (the oxide in a conventional silicon MOSFET), while $Q_{inv}(x)$ and $V(x)$ are the voltage and charge density, respectively, at a distance x from the source end of the channel. The current in the channel is constant (in the absence of leakage to the gate) so Equation 1.4 should apply to a short segment of the channel over which the charge density is nearly constant:

$$\begin{aligned} I_D &= \frac{Q_{inv}(x)W\,dx}{t_r} \\ &= \frac{C_g W(V_G-V_T-V(x))\,dx}{t_r} \end{aligned} \tag{1.6}$$

Now, the transit time t_r for this short segment is given by the drift velocity $v_d(x)$, which in turn is related to the mobility and the electric field by Equation 1.1. Since the electric field in the channel is given by the gradient of the channel voltage,

$$\begin{aligned} v_d(x) &= \mu \boldsymbol{E}(x) \\ &= \mu \left.\frac{dV}{dx}\right|_x \end{aligned} \tag{1.7}$$

Substituting Equation 1.7 into Equation 1.6,

$$\begin{aligned} I_D &= \frac{C_g W(V_G-V_T-V(x))\,dx}{dx/(\mu\,dV/dx)} \\ &= \mu C_g \frac{W}{dx}(V_G-V_T-V(x))dV \end{aligned} \tag{1.8}$$

Integrating this equation from source to drain, and again taking advantage of the fact that I_D is constant,

$$\begin{aligned}\int_0^L I_D dx &= \int_{V_S}^{V_D} \mu C_g W (V_G - V_T - V(x)) dV \\ &= \mu C_g \int_0^{V_{DS}} W (V_{GS} - V_T - V(x)) dV \\ I_D L &= \mu C_g W \left((V_{GS} - V_T) V_{DS} - \frac{V_{DS}^2}{2} \right)\end{aligned} \tag{1.9}$$

Finally, the drain current is found to be

$$I_D = \mu C_g \frac{W}{L} \left((V_G - V_T) V_{DS} - \frac{V_{DS}^2}{2} \right) \tag{1.10}$$

1.4.3 Saturation

The result of Equation 1.10 only applies in the case where $V_{DS} < V_G - V_T$. If the bias voltage is greater than this, then according to Equation 1.5, the charge density in the inversion layer will change sign along the channel. This is illustrated in Figure 1.3:

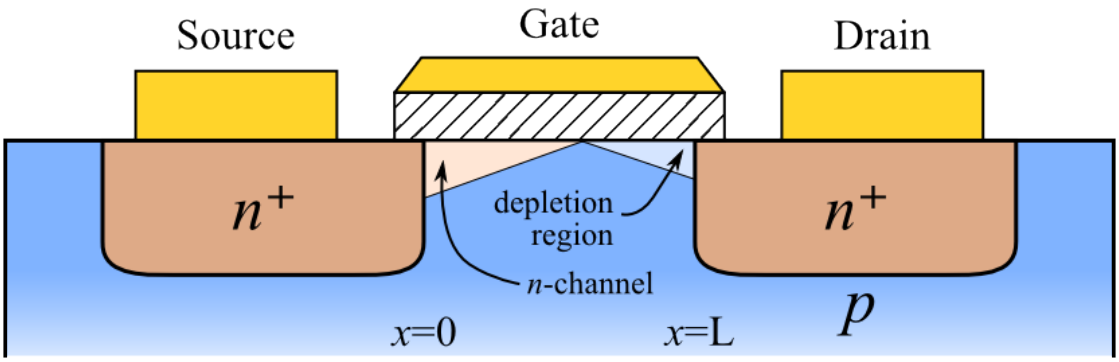

Figure 1.3: Enhancement-mode n-channel MOSFET with $V_{DS} > V_G - V_T$. The depth and color of the channel visually represent the magnitude and sign of the free charge density in the inversion layer.

The region of inverted charge density (*p*-type in the case of an NMOS device) near the drain will form a *pn* junction with the *n*-doped drain region. This behaves like a *reverse-biased* diode, so free holes (*p*-type carriers) will not be able to flow from this

region into the drain. Therefore there is little current contribution from this region. At the point where $Q_{inv}=0$, the channel voltage will be $V(x)=V_G-V_T$, and beyond this point there will be a high-resistance depletion region which contributes the remaining voltage drop ($V_{DS}-(V_G-V_T)$) [4].

As a result, the MOSFET reaches a state known as current saturation, wherein the current is limited to its value for $V_{DS}=V_G-V_T$:

$$I_D=\mu C_g\frac{W}{L}\begin{cases}(V_G-V_T)V_{DS}-\dfrac{V_{DS}^2}{2} & V_{DS}<V_G-V_T\\ \dfrac{(V_G-V_T)^2}{2} & V_{DS}\geq V_G-V_T\end{cases} \tag{1.11}$$

In Figure 1.4(a), I plot the drain current predicted by Equation 1.11 for an *n*-channel MOSFET with $\mu C_g(W/L)=10^{-3}\ \mathrm{A/V^2}$ and a threshold voltage of $V_T=+1\ \mathrm{V}$:

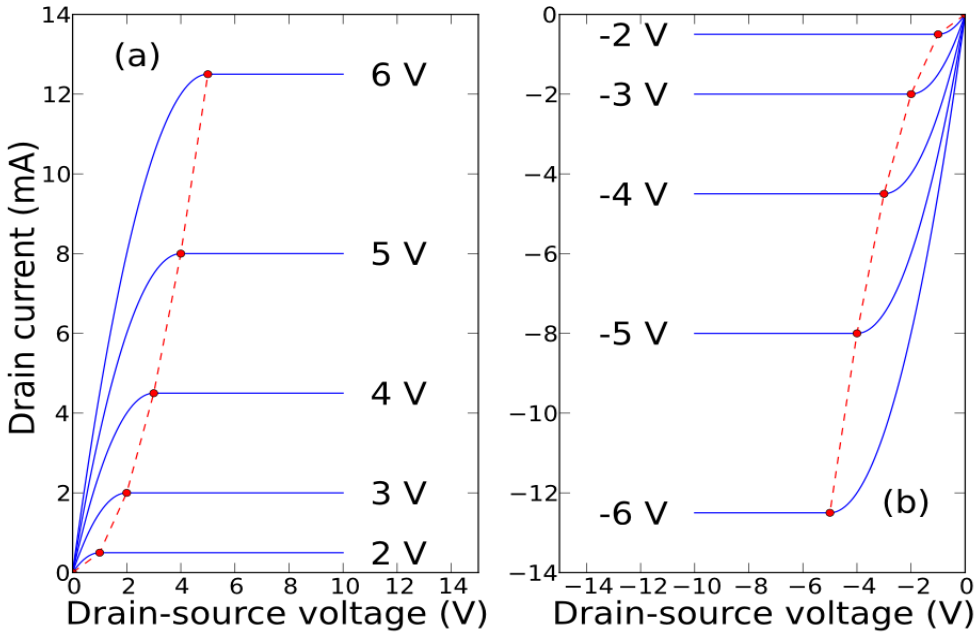

Figure 1.4: Characteristic current-voltage curves for (a) an NMOS transistor with $\mu C_g(W/L)=10^{-3}\ \mathrm{A/V^2}$ *and* $V_T=+1\ \mathrm{V}$*, and (b) a PMOS transistor with* $\mu C_g(W/L)=10^{-3}\ \mathrm{A/V^2}$ *and* $V_T=-1\ \mathrm{V}$*, at* $V_G=\pm 2, \pm 3, \pm 4, \pm 5, \pm 6\ \mathrm{V}$*, respectively. Drain currents are from (a) Equation 1.11 and (b) Equation 1.12. Dashed lines and symbols indicate the saturation current, which is quadratic with respect to drain-source bias voltage.*

The formula for the drain current, Equation 1.11, applies equally to *n*-channel or *p*-channel MOSFETs, except that in a *p*-type MOSFET, the condition for saturation is reversed:

$$I_D=\mu C_g\frac{W}{L}\begin{cases}-(V_G-V_T)V_{DS}-\dfrac{V_{DS}^2}{2} & V_{DS}>V_G-V_T\\ -\dfrac{(V_G-V_T)^2}{2} & V_{DS}\le V_G-V_T\end{cases} \tag{1.12}$$

This result may be derived using the procedure described above for an *n*-channel MOSFET, but realizing that the gate-channel voltage ($V_G - V_T - V(x)$) must be *negative* rather than positive to produce the desired *p*-type charge density in the inversion layer. In Figure 1.4(b), I plot the drain current predicted by Equation 1.12 for a *p*-channel MOSFET with $\mu C_g (W/L) = 10^{-3}\ \mathrm{A/V^2}$ and a threshold voltage of $V_T = -1\ \mathrm{V}$. This is simply the inverse of the *n*-channel MOSFET plotted in Figure 1.4(a).

1.5 Application to organic thin-film transistors

The microscopic mechanisms by which organic thin semiconductors conduct electric current, such as those discussed in Section 1.7, are often very different from the band-like transport typical of crystalline inorganic semiconductors. Unlike the case of crystalline silicon semiconductors, which show band-like conduction, carriers in most organic semiconductors are localized by the granular or amorphous structure of the material, and transport occurs via hopping or percolative conduction. The mobility of organic semiconductors tends to be more strongly gate-dependent than that of silicon. As described by Vissenberg and Matters [5] and discussed in Section 1.7, this is because energy barriers to hopping conduction are reduced as low-energy states (charge traps) fill up and free carriers occupy higher-energy states.

Furthermore, some organic semiconductors exhibit electric field-dependent mobility; like many insulating materials, they are susceptible to the Poole-Frenkel effect in which a strong electric field acts to reduce the localization of carriers and thereby to increase conductivity [6]. This effect is particularly noticeable as the channel length of

TFT devices is reduced, increasing the longitudinal electric field for a given drain-source bias, and was studied by my colleague Adrian Southard and described in detail in his doctoral dissertation [7].

Although it is possible to use heavily-doped semiconductor regions as contacts in an organic TFT, similar to the conventional MOSFET of Figure 1.2, the contact resistance of these structures is much higher than those of conventional MOSFET contacts, and also extremely sensitive to changes in the doping level of the organic semiconductor [8],[9]. In practice the contacts are most often made by direct contact between a metal electrode and the lightly-doped organic film. Thus additional contact effects, some of which are not easy to control, may be present in organic TFTs. For example, depending on the work function of the electrode metal, the source or drain electrodes may form either Schottky barrier or Ohmic contacts [10]. Moreover, some organic semiconductors, such as pentacene, adopt drastically different film morphology on different surfaces, which can result in highly resistive structural boundaries where pentacene deposited on the oxide substrate meets pentacene deposited on the metal electrodes (see Section 1.6.2). Because of these properties, it is not always straightforward to separate the transport behavior of the organic semiconductor itself from that of the contacts and interfaces.

Despite these significant differences, organic semiconductors can be fabricated into organic thin-film transistor devices, which have a three-terminal structure reminiscent of a conventional silicon MOSFET, and can show electrical characteristics that are fairly well described by Equations 1.12, which give the drain current of a *p*-channel MOSFET.

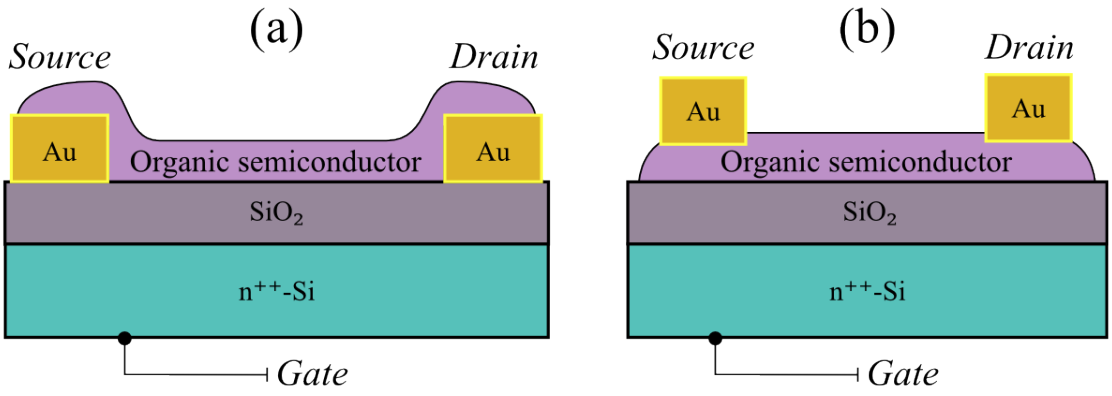

Figure 1.5: Structure of (a) a bottom-contacted organic thin-film transistor and (b) a top-contacted organic thin-film transistor on a heavily n-doped silicon substrate.

An example of the bottom-contact TFT structure is shown in Figure 1.5(a): this device consists of an organic semiconductor deposited over metal contacts, on an oxidized, highly doped silicon wafer (the doped silicon provides a low-resistance back gate electrode). The thin film of organic semiconductor may be deposited via spin-coating, solution-casting, ink-jet printing, transfer printing, or thermal evaporation, depending on the specific material and application. Top-contact TFTs (such as that shown in Figure 1.5(b)) are also fabricated and studied; in the case of pentacene, they tend to be higher-performing because depositing the semiconductor on the uniform silicon substrates does not introduce the structural faults that occur when pentacene is deposited over metal electrodes. However, top-contact devices also can be more difficult to model, because of the thick layers of low-conductivity organic semiconductor which separate the electrodes from the semiconducting channel close to the gate dielectric.

As in the MOSFET structure, the gate of an organic TFT is capacitively coupled to the organic semiconductor, so a change in gate voltage, V_{GS}, can add or remove

carriers. Most organic semiconductors are strongly *p*-type ($\mu_h \gg \mu_e$), so gate voltages must be more negative than the threshold voltage in order to populate the semiconductor channel with large numbers of carriers ($V_G < V_T$). Despite the differences in transport mechanisms, the dc circuit behavior of many *p*-type organic semiconductors is well-approximated by Equation 1.12, which expresses the drain current, I_D, in terms of the gate-source and drain-source voltages, the threshold voltage, and the field-effect mobility of the semiconductor.

1.6 Pentacene

Pentacene ($C_{22}H_{14}$) is a small-molecule organic semiconductor that has been extensively studied [11-15]. (I will focus on its ac transport properties in Chapter 2.) It is a polycyclic aromatic hydrocarbon with a molecular structure that consists of five fused benzene rings arranged in a straight line, as shown in Figure 1.6:

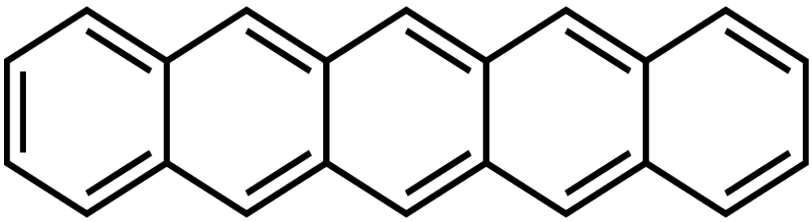

Figure 1.6: The chemical structure of a pentacene molecule. (From Wikipedia.)

Pentacene's dc transport properties have been thoroughly investigated, as it is one of the highest-mobility organic semiconductors. The record *p*-type field-effect mobility (μ_{FET}) for thin-film pentacene devices exceeds 3.0 cm²/V·s [16], which is close to the performance of the best amorphous-silicon (a-Si:H) thin-film transistors [17]. Pentacene's high mobility is attributed especially to its large grain size, band-like

transport in single crystal samples [18], and the tendency of adjacent grains to align their crystal axes so as to form a single crystal, under the right growth conditions [11]. Below I discuss the preparation of thin films of pentacene, and the conditions that affect disorder in pentacene films and lead to a wide range of observed mobilities and transport behaviors.

1.6.1 Deposition

Because pure pentacene has a low solubility, and because its transport characteristics are often degraded by exposure to common solvents, it is not amenable to deposition techniques such as ink-jet printing or spin-coating, which are often used to pattern other organic semiconductors [12]. (Soluble functionalized derivatives of pentacene have been synthesized, however, and have achieved high mobility [19].) Pentacene is usually deposited by thermal evaporation from a powder source, and sublimes at approximately 195°C in high-vacuum conditions [20].

The morphology of pentacene thin films is sensitive to conditions including the deposition rate and temperature, as well as the quality of the source material and the particular substrate. Film morphology has strong effects on electrical transport: a wide range of transport phenomena have been reported for pentacene, from band-like transport in high-purity single crystals [18],[21], to thermally-activated hopping conduction in disordered polycrystalline samples.

1.6.2 Film morphology

Bulk pentacene crystals have a well-known triclinic structure, but thin films of pentacene on SiO_2 form in a significantly different thin-film phase, reported in 1996 by Dimitrakopoulos et al. [22]. In this phase, which also has a triclinic unit cell, pentacene molecules do not lie flat on the substrate, but rather stand up almost vertically, like blades of grass, with an angle of 17° to the normal, as shown in Figure 1.7(a). In each layer, pentacene molecules arrange themselves into a herringbone structure, with two molecules per unit cell, as shown in Figure 1.7(b) [15]:

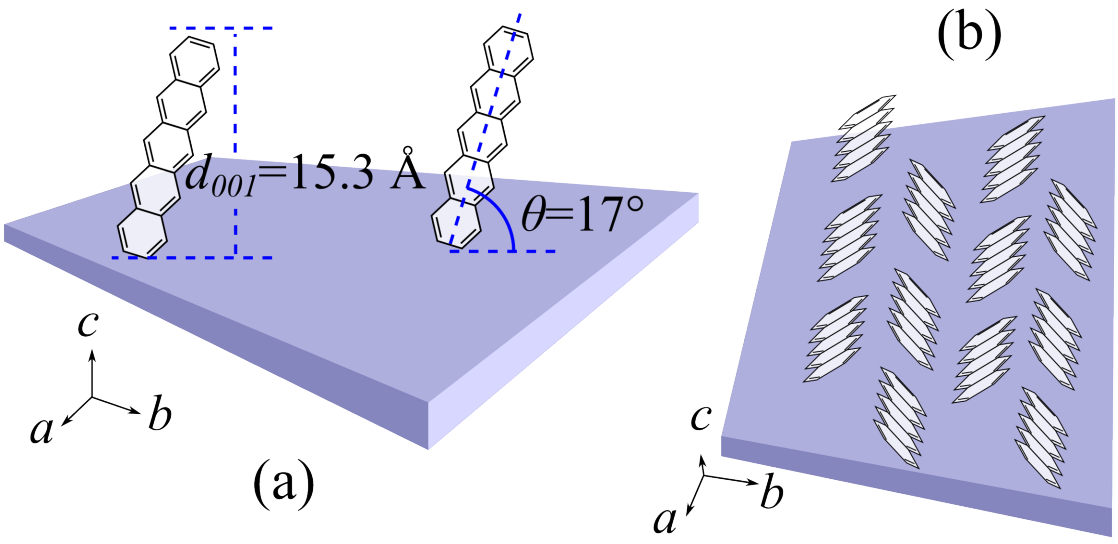

Figure 1.7: Thin-film phase of pentacene on SiO_2 substrate, showing (a) the vertical arrangement of pentacene molecules and the layer spacing (from [22]), and (b) the herringbone arrangement of pentacene molecules in individual layers, with two pentacene molecules per unit cell.

The early, sub-monolayer stages of pentacene deposition on Si and SiO_2 have been studied extensively, by techniques including *in-situ* low-energy electron microscopy

(LEEM) and photoemission electron microscopy (PEEM) of growing pentacene [23], [24], as well as atomic force microscopy of sub-monolayer pentacene coverage on SiO_2 [25-27]. As it deposits, pentacene nucleates single monolayer islands on the substrate, which acquire a fractal shape. Figure 1.8 shows AFM images of pentacene at various early stages of deposition on reduced (hydrogen-terminated) and oxidized (SiO_2) silicon:

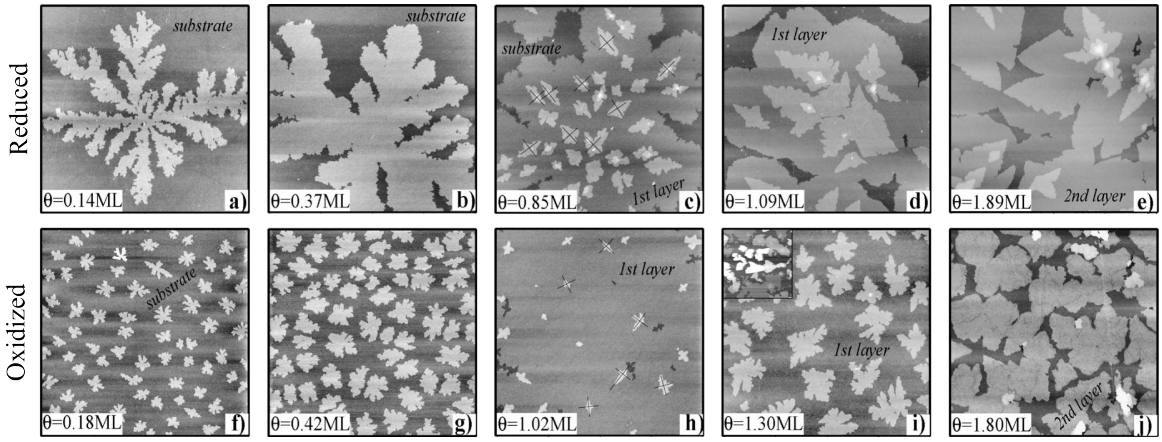

Figure 1.8: AFM topography images of 0-2 monolayer pentacene growing on reduced (a-e) and oxidized (f-j) silicon substrates. Each image shows an area of 10 μm×10 μm. (From [26])

The nucleation and growth of pentacene islands is described in terms of deposition, diffusion, and aggregation (DDA) [23],[26]. The theory of diffusion-limited aggregation has been used to describe clusters deposited by metal and other inorganic vapors. This very simple model starts with a single seed particle at the origin of a large two-dimensional lattice. Subsequent particles are deposited one-by-one on the lattice at random locations, and engage in random walks (diffusion) on the surface until they touch the boundaries of the cluster, after which point their positions remain fixed [28].

Numerical simulations [29] and analytical modeling [30] have shown that this process results in a cluster with a Hausdorff dimension of $d_f = 5/3 \approx 1.67$.

Observations of pentacene deposition show islands which expand outwards in dendritic shapes; submonolayer pentacene islands on clean SiO_2 have fractal dimensions around $d_f = 1.82$, estimated by box-counting (which gives an upper bound on the true Hausdorff dimension) [27]. Because the diffusion-limited aggregation model assumes only a single mobile particle in the vicinity of each growing cluster, these results are only applicable to extremely slow deposition of pentacene; Ruiz et al. deposited pentacene at 0.75 Å/minute, equivalent to 20 minutes for a complete monolayer [27]. Their X-ray reflectivity measurements of the first monolayer also show only about 75% of the electron density of bulk pentacene, indicating a lower packing density [26]. This result is likely to be very significant for transport in pentacene TFTs on SiO_2, where only one or two monolayers of pentacene closest to the oxide carry nearly all the current.

As seen in Figure 1.8, pentacene islands remain exclusively monolayer until 60%-80% coverage of the surface has been achieved, whether on reduced Si, SiO_2, or clean Si(001) [23],[26]. This is probably because the diffusion constant of pentacene on pentacene (D_p) is much higher than that of pentacene on these substrates (D_s) [23]. The location of initial nucleation sites may be determined by impurities which pin pentacene molecules, but these produce different aggregations of pentacene than those observed on clean SiO_2 [26]. The nucleation density does vary greatly between reduced silicon and SiO_2, however; it is 10^2-10^3 times higher on the latter, probably because of much reduced diffusion of pentacene on SiO_2 [26]. This can be seen in Figure 1.8, where islands of

pentacene on reduced silicon are much larger than on SiO_2, but both have similar fractal shapes.

1.6.3 Effects of temperature and impurities on film morphology

On thermal oxide (SiO_2) substrates, pentacene forms larger grains when deposited at higher temperatures, up to the point where other effects such as nucleation of the bulk phase [31]. For example, Jin et al. showed that pentacene deposited on thermal oxide held at a substrate temperature of 20°C formed grains of approximately 200-300 nm, while increasing the temperature to 80°C allowed the formation of 2000-4000 nm grains [32]:

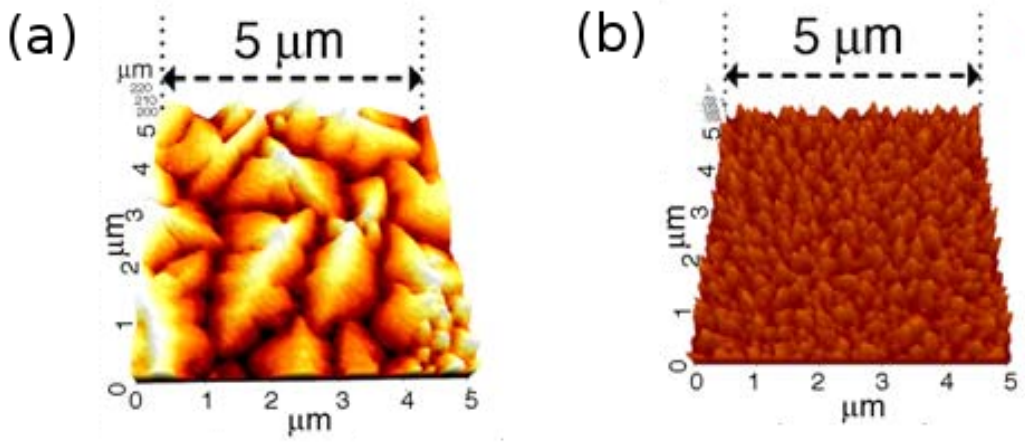

Figure 1.9: Atomic-force microscopy (AFM) images of pentacene deposited on SiO_2 substrates held at (a) 80°C and (b) 20°C. (From [32])

Grain size has a very strong effect on the mobility of thin-film transistors, as shown by Horowitz and Hajiaoui for small-molecule organic semiconductors such as α-sexithiophene (α-6T) [33]. Ruiz et al. demonstrated that monolayer islands of pentacene

on SiO_2 have randomly-oriented crystal axes [26]. Since subsequent layers grow epitaxially on the layers below, the orientation of multilayer grains in the thin-film phase is random as well. Therefore, they argued that in order to achieve aligned crystal axes over neighboring grains (as seen by Laquindanum et al. [11]), it is necessary to grow monolayer islands of pentacene as large as possible, and that on clean substrates this essentially requires making the diffusion constant of pentacene as large as possible.

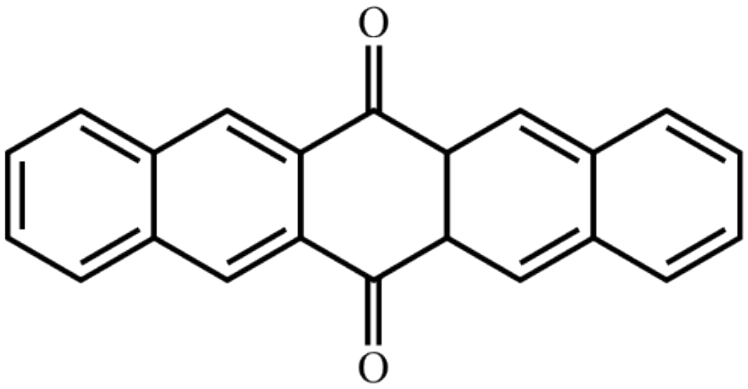

Figure 1.10: The chemical structure of 6,13-pentacenequinone, a by-product of pentacene synthesis and a common impurity in commercial pentacene.

The morphology of pentacene single crystals [18] and thin films [20] is also very sensitive to the purity of the source material. The dominant impurity in commercially produced pentacene is typically 6,13-pentacenequinone (PnQ), which is a by-product of the synthesis process; PnQ is found at a concentration of 0.68% in the pentacene supplied by Aldrich, which is used by many groups including my own [18]. Gomar-Nadal et al. showed that pentacene and PnQ phase-separate during deposition with PnQ concentrations above 0.8% [20]. Because PnQ grows in a 3D fashion that is very different from the layer-by-layer growth of pentacene, the morphology of sub-monolayer pentacene films changes at higher concentrations, with increased density of nucleation

sites and correspondingly smaller islands sizes. At lower impurity levels there is no apparent change in film morphology at early growth stages [20], but thin-film transistor devices show a strong dependence of field-effect mobility on PnQ concentration nevertheless, as reproduced in Figure 1.11:

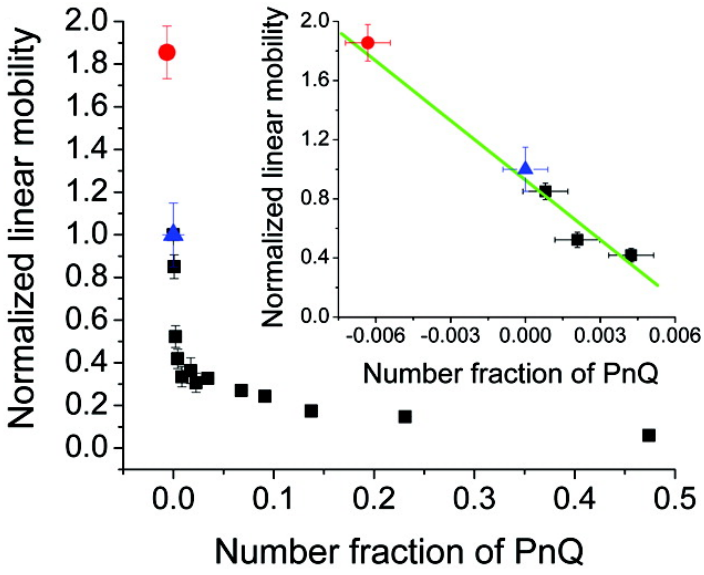

Figure 1.11: Field-effect hole mobility of top-contacted, thin-film transistors made from pentacene containing various relative concentrations of the 6,13-pentacenequinone (PnQ) impurity. Red circles show pentacene "cleaned" by sublimation of PnQ, while black squares show pentacene with added PnQ, and blue triangles show as-purchased commercial pentacene from Aldrich. (From [20])

This result shows that PnQ has an effect not only on the large-scale morphology of pentacene, but on its electronic transport as well. Gomar-Nadal et al. suggest that this is due to charge traps introduced by local structural changes around PnQ molecules, and this is supported by Jurchescu et al. who find that the hole mobility of *single-crystal* pentacene islands depends strongly on PnQ concentration as well [20],[18].

1.6.4 Effects of substrate

The mobility of pentacene-based TFTs is also affected by the substrates on which the devices are fabricated. As described in Section 1.6.2, different types of silicon substrates allow the formation of larger or smaller grains by varying the diffusion parameters and the density of sites at which monolayer islands of pentacene nucleate.

The substrate can also affect the mobility of pentacene in other ways, such as by reducing the density of charge traps in the oxide. Self-assembled monolayers (SAMs) such as octadecyltrichlorosilane (OTS), applied to SiO_2 substrates prior to the deposition of pentacene, have been shown to increase the mobility of the TFTs [34]. Interestingly, OTS seems to *decrease* the size of pentacene grains, but in so doing also causes more pentacene molecules to lie flat on the SiO_2 substrate, rather than standing on end as described in Section 1.6.2. Thus part of the effect of the SAM is due to changes in film morphology.

However, SAMs such as OTS also reduce the density of charge traps at the interface between the SiO_2 substrate and the pentacene semiconductor layer. This effect has been shown to be independent of changes in the film morphology. The sub-threshold behavior of MOSFET devices depends on electric field (or equivalently on drain-source bias, for a constant channel length): MOSFETs with high interfacial trap density do not turn off (i.e. I_D does not fall to zero) as rapidly or as fully when $V_G > V_T$, in the case of a *p*-channel device [35]. Yagi et al. showed that pentacene TFTs on bare SiO_2 exhibit far higher sub-threshold currents, and greater field-dependence, that those on SiO_2 treated with 1,1,1,3,3,3-hexamethyldisilazane (HMDS), another SAM surface treatment [36].

They argued that this was due to elevated interfacial trap density in the devices on untreated substrates. Subsequent reports have confirmed this by observing changes in threshold voltage and hysteresis in pentacene TFTs undergoing different surface treatments [37].

In summary, the mobility of pentacene thin-film transistors is sensitive to a variety of defects and non-uniformities resulting from their preparation, including point defects such as pentacenequinone impurities and substrate-induced interfacial charge traps, as well as extended defects such as grain boundaries and stacking faults due to changes in substrate.

1.7 Charge transport in organic thin films

Several models have been proposed to explain microscopic charge transport in polycrystalline thin films of small-molecule organic semiconductors. Variations in the electrical transport mechanisms can have large effects on bulk film mobility, and other macroscopic properties relevant to the development of practical and reliable organic semiconductor devices.

Studying α-sexithiophene, Horowitz et al. observed temperature-dependent conductivity consistent with a thermal trapping and release model, in which most p-type carriers (holes) are trapped in localized states due to grain boundaries, but which are thermally activated or released into a long-range transport level (equivalent to the valence band) [38]. Below 150 K, however, they observed a different temperature dependence of the conductivity, which they attributed to thermally-activated hopping.

1.7.1 Thermally-activated hopping

Vissenberg and Matters used a thermally-activated hopping model, in which carriers hop between localized states without a long-range transport band, to analyze polycrystalline pentacene and polythienylene vinylene (PTV) [5]. Despite the fact that their field-effect mobilities (μ_{FE}) differ by three orders of magnitude, both showed good agreement with this model. The authors attributed the vast difference in mobility primarily to a difference in the overlap parameter governing the probability of tunneling between neighboring localized sites. As the length scale of this overlap parameter is smaller than the size of a single molecule, they noted that it was likely due to the film morphology, and that pentacene thin films had better stacking properties than those of PTV.

The hopping model of Vissenberg and Matters begins with the notion of a localized, exponential density of states:

$$g(\epsilon)=\frac{N_t}{k_B T_0}\exp\left(\frac{\epsilon}{k_B T_0}\right) \tag{1.13}$$

where N_t is the number of states per unit volume, k_B is Boltzmann's constant, and T_0 is a fitting parameter with units of temperature.

This density of states is related to the charge carrier occupation fraction, δ, by the Fermi-Dirac distribution:

$$\begin{aligned}\delta &= \frac{1}{N_t}\int_{-\infty}^{+\infty} d\epsilon\, g(\epsilon)\, f(\epsilon, \epsilon_F) \\ &= \frac{1}{k_B T_0}\int_{-\infty}^{+\infty} d\epsilon\, \frac{e^{\epsilon/k_B T_0}}{e^{(\epsilon-\epsilon_F)/k_B T}+1} \\ &= \frac{e^{\epsilon_F/k_B T_0}}{k_B T_0}\int_{-\infty}^{+\infty} d\epsilon\, \frac{e^{(\epsilon-\epsilon_F)/k_B T_0}}{e^{(\epsilon-\epsilon_F)/k_B T}+1}\end{aligned} \tag{1.14}$$

Making the substitutions $x = e^{(\epsilon - \epsilon_F)/k_B T_0}$ and $dx/d\epsilon = x/k_B T_0$:

$$\begin{aligned}\delta &= \frac{e^{\epsilon_F/k_B T_0}}{k_B T_0}\int_0^{+\infty}\frac{dx\,k_B T_0}{x}\frac{x}{x^{T_0/T}+1} \\ &= e^{\epsilon_F/k_B T_0}\int_0^{+\infty}\frac{dx}{x^{T_0/T}+1}\end{aligned} \tag{1.15}$$

For $T \ll T_0$, the integral is very nearly equal to a product of gamma functions,

$$\delta = e^{\epsilon_F/k_B T_0}\Gamma(1-T/T_0)\Gamma(1+T/T_0) \tag{1.16}$$

From here, Vissenberg and Matters treat the system using percolation theory, which models the system as a random 3-dimensional network of sites, with a randomized distribution of connectivity among the neighboring sites. From this model, and Equations 1.15 and 1.16, they derive the conductivity of as a function of occupation fraction and temperature [5]:

$$\sigma(\delta, T) = \sigma_0\left(\frac{\pi N_t \delta (T_0/T)^3}{(2\alpha)^3 B_c \Gamma(1-T/T_0)\Gamma(1+T/T_0)}\right)^{T_0/T} \tag{1.17}$$

Here, α is the overlap parameter which governs the effective tunneling distance between neighboring sites, while B_c is the critical "bond density" (roughly 2.8 in three dimensions) which specifies the minimum connectivity required for continuous percolation paths through the system. The authors observe that this formula for the conductivity follows an Arrhenius-like temperature dependence (that is, $\sigma \sim \exp[-E_a/(k_B T)]$), but with an activation energy that is logarithmically dependent on temperature [5]:

$$E_a = k_B T_0 \ln\left(\frac{\pi N_t \delta (T_0/T)^3}{(2\alpha)^3 B_c \Gamma(1-T/T_0)\Gamma(1+T/T_0)}\right) \tag{1.18}$$

From the formula for the conductivity, Equation 1.17, and by modeling the thin charge accumulation layer above the interface between the semiconductor and gate

dielectric, Vissenberg and Matters arrived at a formula for the field-effect mobility (μ_{FE}) of a thin-film transistor governed by variable-range hopping. This mobility is itself dependent on the magnitude of the gate bias, V_G:

$$\mu_{FE} = \frac{\sigma_0}{e}\left(\frac{\pi (T_0/T)^3}{(2\alpha)^3 B_c \Gamma(1-T/T_0)\Gamma(1+T/T_0)}\right)^{T_0/T} \times \left[\frac{(C_i V_G)^2}{2 k_B T_0 \epsilon_s}\right]^{T_0/T-1} \tag{1.19}$$

Here ϵ_s is the dielectric constant of the semiconductor film itself, and C_i is the capacitance per unit area of the gate dielectric. The increased mobility at higher absolute gate voltage occurs because carrier density increases with increasing gate voltage. This causes the lower-energy states (i.e. charge trips) to fill up, resulting in a higher density states at the Fermi energy, thus reducing the energy barrier for activated jumps to neighboring sites [5].

Vissenberg and Matters fit Equation 1.19 to experimental temperature-dependent mobility data for the organic semiconductors pentacene and polythienylene vinylene (PTV) on silicon dioxide (SiO_2) substrates. They assumed a dielectric constant of $\epsilon_s = 3\epsilon_0$ for both organic materials, leaving σ_0, α, and T_0 as fitting parameters. They found that they could obtain good fits to the experimental data:

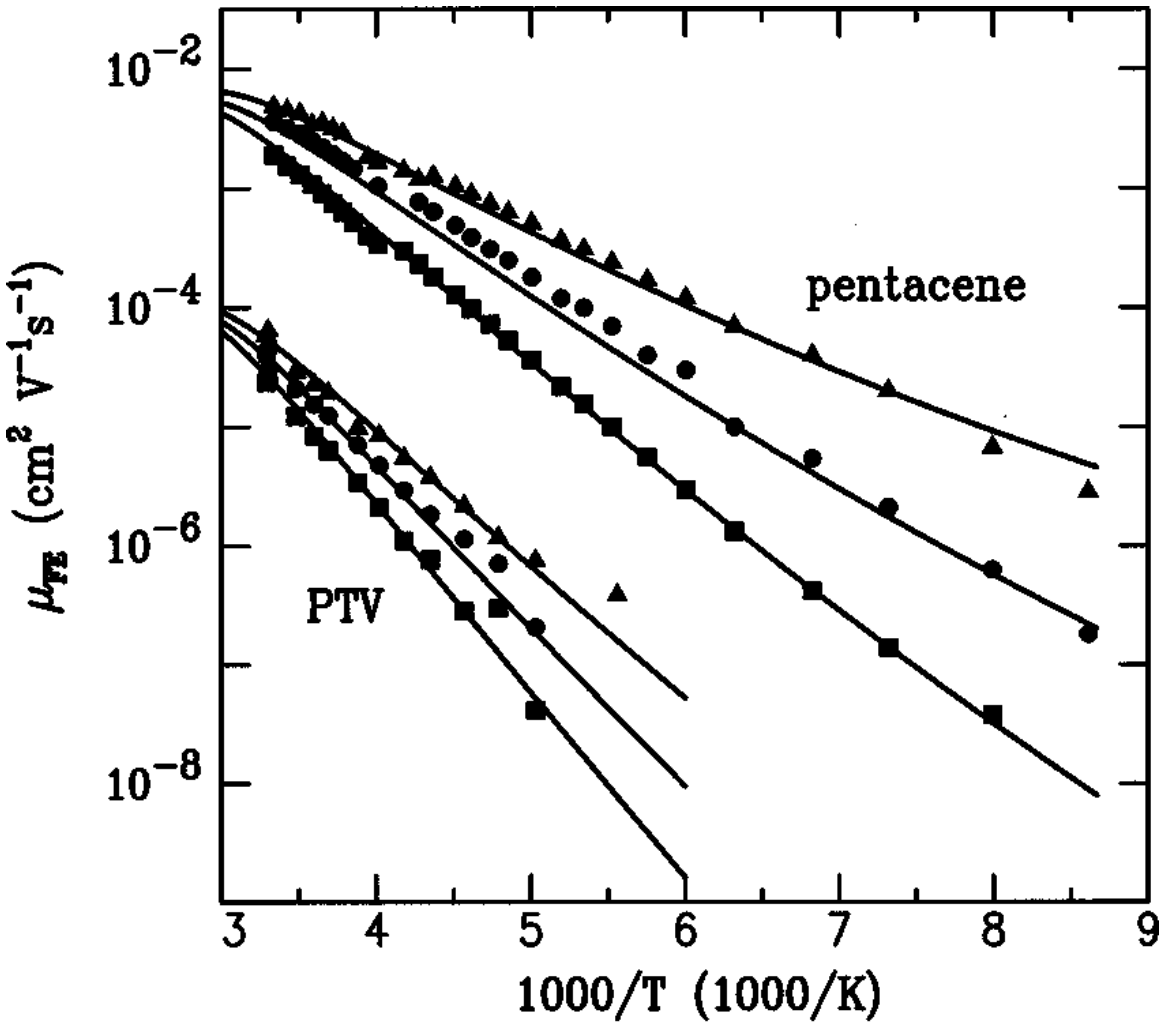

Figure 1.12: Field-effect mobility as a function of temperature for spin-cast pentacene and polythienylene vinylene (PTV). Symbols show experimental data at gate voltages of -20 V (triangles), -10 V (circles), and -5 V (squares), while solid lines show fits using Equation 1.19. (From [5])

Their fits produce the notable result that the overlap parameter α^{-1} is significantly larger for pentacene (about 2.2 Å) than for PTV (about 0.8 Å); this accounts for the difference in the mobilities of pentacene and PTV, which exceeds 10^2. They conjecture that pentacene molecules stack more closely than PTV molecules, leading to a

larger area of overlap in neighboring electronic wave functions, and thereby increasing [5].

1.7.2 Other models of conduction

Other models have been proposed to explain electronic transport in organic materials, including small-polaron hopping. A polaron is a quasiparticle which results from a slow-moving charge carrier that creates a significant distortion in the surrounding lattice. A small-polaron model assumes that this distortion is on the order of a single unit cell of the lattice. Early models assumed no correlations between successive hops [39], but this may will hold if hops proceed more rapidly than the lattice can relax. Emin showed that the uncorrelated model is inadequate for carrier mobility greater than approximately 0.1 cm²/V·s [40].

Nelson et al. subsequently provided evidence that neither an uncorrelated nor a correlated model of small-polaron hopping can satisfactorily explain the temperature-dependent transport properties of pentacene devices with mobilities of $\mu \geq 0.3 \text{ cm}^2/\text{V}\cdot\text{s}$.

1.8 Conclusions

In this chapter, I have summarized the framework within which organic semiconductor devices are modeled. First, I introduced the quadratic MOSFET model (Section 1.3) which describes the behavior of gated field-effect transistor devices, both those based on crystalline inorganic semiconductors and similarly-arranged organic thin film transistors. (in Section 1.4).

Various kinds of structural and electronic disorder can be present in organic thin films including grain boundaries; impurities, whether byproducts of synthesis, such as pentacenequinone, residue from fabrication, or environmental contaminants; and substrate-induced interfacial charge traps. The presence or absence of these defects can lead to variations in the carrier mobility over several orders of magnitude, likely by altering the dominant microscopic mechanisms by which charge transport proceeds in these materials (Section 1.7). In the case of pentacene, which is the focus of my experimental work described in the next chapter, research has shown that it is feasible to tune many of these sources of disorder. It is interesting to consider the effects of microscopic variations on the macroscopic circuit properties, and conversely to find out whether the latter can provide any new insights about the former.

1.9 Structure of this dissertation

In Chapter 2, I will describe my experiments on the ac transport properties of the organic semiconductor pentacene. I fabricated bottom-contacted pentacene TFTs of various geometries, focusing on devices with very long channels designed to hasten the onset of high-frequency behavior. I developed a novel method of characterizing the complex impedance of a thin film, by treating it as a finite-length resistor-capacitor transmission line (RCTL). I have applied this model to my pentacene TFTs, and extracted the complex impedance of the pentacene films. I analyze its unexpected frequency dependence and explain it in the framework of the universal dielectric response (UDR) model of ac conduction in disordered solids. The bulk of the experimental results of Chapter 2 have been published in *Applied Physics Letters* [41].

In Chapter 3, I introduce graphene, a two-dimensional crystalline allotrope of carbon, and describe its physical, electronic, and optical properties. I review established and emerging techniques for synthesizing graphene, and for characterizing its structure and quality. Finally, in Section 3.9, I describe in detail the techniques of atmospheric-pressure chemical vapor deposition (CVD) which I have used to synthesize films of graphene on nickel and copper substrates. While published reports of low-pressure growth on copper show only single-layer graphene, my CVD-grown graphene appears to contain regions of multilayer thickness, motivating further investigation.

In Chapter 4, I motivate the use of optical contrast for the identification of graphene and for the determination of its thickness. I derive the transfer-matrix method of thin film optics, used to calculate the optical reflectance and transmittance of multilayered structures. I use this method to make quantitative predictions about the contrast of graphene on SiO_2 substrates, and discuss experimental techniques to minimize errors due to uncertainty in the index of refraction of graphene (published reports show considerable variation) and the properties of the substrates against which its contrast is measured. I apply these techniques to my CVD-grown graphene and to reference samples of mechanically-exfoliated graphene, and demonstrate peaks in the optical contrast histograms of my samples which correspond to multilayer graphene.

Finally, in Chapter 5, I motivate the use of Raman spectroscopy as another tool for characterizing graphene. I review the literature on the Raman spectrum of graphene and of graphene multilayers and their dependence on the electronic band structure of the material. I show Raman spectra which I measured on my CVD-grown graphene, at

points where I also measured optical contrast, and find that the Raman *2D* band of these samples is invariably single-peaked, both in regions that I have identified as single-layer by their optical contrast, and in regions identified as multilayer. This is surprising, given numerous experimental and theoretical reports of a multi-peaked *2D* band for multilayer mechanically-exfoliated graphene. However, I demonstrate that there are systematic variations in the *2D* band of my CVD-grown graphene. I show that the unexpected combination of Raman and optical contrast which I observe is consistent with published reports of misoriented or turbostratic multilayer graphene. Finally, I show topography images of my CVD graphene samples, which I measured using atomic force microscopy (AFM). These show graphene-on-graphene steps, which further demonstrate the presence of multilayer graphene in my samples.

2. Measuring the ac transport properties of pentacene

2.1 Motivation

Organic thin-film transistors (TFTs) are among the most prominent and promising devices made from organic semiconductors. However, most studies of these devices' performance have used dc measurements exclusively, while many applications, such as flexible display back-planes [42],[14] and radio-frequency ID tags [43],[44] require ac operation. Bulk organic semiconductors show strongly frequency-dependent conductivity [45-48], typical of disordered solids [49-51], at frequencies in the range of 10^4-10^6 Hz. I know of only one attempt to extract the intrinsic conductivity of an organic thin film at finite frequency [52]; however, this study explicitly assumed no frequency dependence of the film conductivity.

In order to design TFTs for ac operation, it is useful to know if the ac transport properties of polycrystalline thin-film transistors are straightforwardly related to their dc transport properties. That is, given complete knowledge of a device's geometry and its dc characterization (in terms of field-effect mobility and threshold voltage, as outlined in Chapter 1), can one accurately predict its response to an applied ac voltage? And, are there significant deviations of the ac conductivity from its dc limit at frequencies relevant for device operation?

This chapter will develop an experimental method for characterizing the complex impedance of a thin film by treating the film over a gate electrode as a finite-length resistor-capacitor transmission line (RCTL). The RCTL model and technique will be

applied to pentacene TFTs, and used to extract the complex impedance of the pentacene film as a function of frequency from 50 Hz – 20 kHz. The experimental results of this chapter have been published in *Applied Physics Letters* [41].

2.2 Transmission line model

In dc analysis of organic thin film transistors, and indeed of MOSFETs in general, the semiconductor channel is modeled as a resistor, with its source-drain resistance, R_{SD}, considered to be a function of the gate voltage, that is $R_{SD}=R_{SD}(V_{GS})$. In the quadratic MOSFET model, R_{SD} is nearly linear with V_{GS} below saturation (see Section 1.4.2), while the dependence is more complex in other models [4]. However, regardless of the exact model used, the semiconducting channel coupling the source and drain contacts is considered to be resistive only (i.e. its reactance is ignored).

At non-zero frequency, both the space- and time-variation of the voltage in the semiconductor channel must be taken into account. The semiconductor channel and gate are capacitively coupled, so there is some frequency-dependent reactance distributed over the length of the channel. To model this, I make use of the transmission line model, which describes wires in which the voltage is varying on a time scale comparable to the time it takes for current to traverse the wire. That is, it applies when

$$\omega \sim L/v \tag{2.1}$$

where ω is the highest-frequency component of the applied voltage, L is the length of the semiconductor channel, and v the drift velocity of the carriers in the channel.

A transmission line is modeled as a series of infinitesimal elements, each containing an infinitesimal resistance R, inductance L, capacitance C, and leakage conductance G:

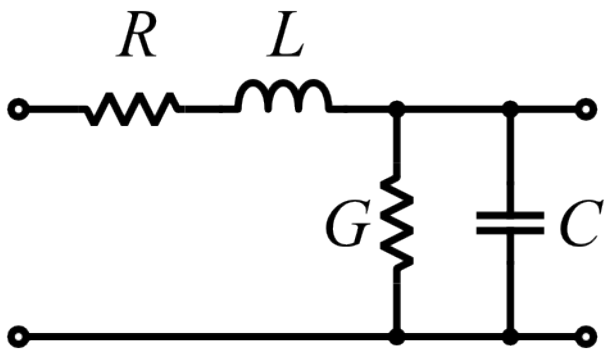

Figure 2.1: A single element of a transmission line.

To apply this model to a back-gated, bottom-contacted organic thin-film transistor, one can imagine the semiconductor channel sliced into a series of these infinitesimal elements, as in Figure 2.2:

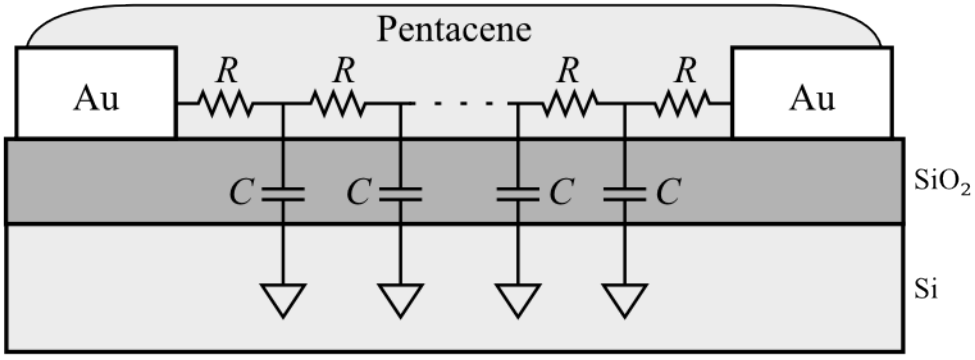

Figure 2.2: Schematic of bottom-contacted TFT modeled as an RC transmission line.

The capacitive coupling of the channel to the back gate is distributed over the entire length of the channel. From this point on, I neglect the leakage conductance of the

channel to the back gate, *G*, which I have found to be very small in comparison with the channel conductance when using standard 300 nm SiO_2 wafers. I will also neglect the self-inductance of the semiconductor channel, since the inductive reactance is much smaller than the channel resistance (that is, $\omega L \ll R$) in the frequency range I study, below 10^5 Hz. This assumption of negligible inductive reactance is confirmed when I generalize the sheet resistance to a complex impedance and measure its frequency dependence (discussed in Section 2.7).

To my knowledge, this resistive-capacitive transmission line (RCTL) model was first applied to thin-film transistor channels by Chow and Wang [53], whose derivation I follow and expand below.

2.2.1 Semi-infinite RC transmission line

I first consider the case of a long strip of conducting material with conductivity σ and capacitance per unit area *c*, treated as a semi-infinite RC transmission line. Let $v(x)$ be the voltage at a distance *x* from the left end of the strip, relative to the ground conductor, and let $i(x)$ be the current at the same point, as shown in Figure 2.3. The explicit time-dependence of $v(x)$ and $i(x)$ are omitted for simplicity:

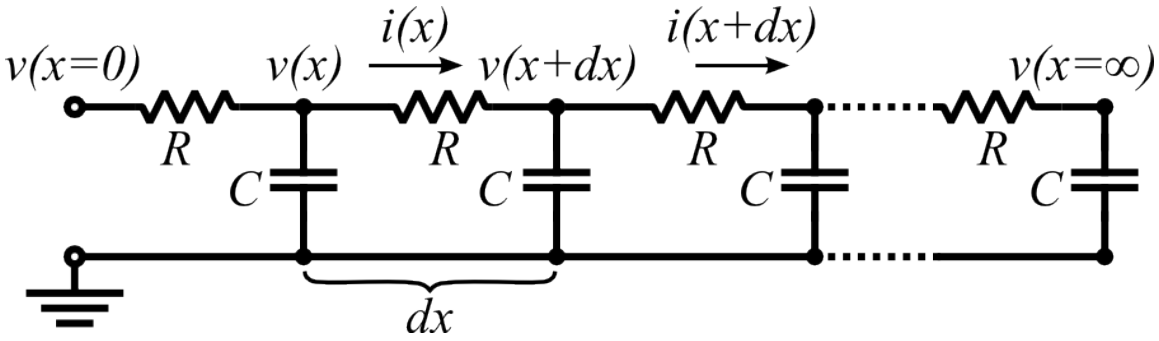

Figure 2.3: Infinite RC transmission line

Now, from Kirchoff's laws and the current-voltage relationship for a capacitor ($i = c\,dv/dt$),

$$\begin{aligned} v(x) - v(x+dx) &= (R\,dx)\cdot i(x) \\ i(x) - i(x+dx) &= (C\,dx)\,dv/dt \end{aligned} \tag{2.2}$$

R and *C* can be expressed in terms of the conductivity, σ, and capacitance per unit area, *c*:

$$\begin{aligned} R &= dx/(\sigma W) \\ C &= c\,dx\,W \end{aligned} \tag{2.3}$$

In the infinitesimal limit, where $dx \to 0$, Equations 2.2 can be simplified to

$$\begin{aligned} dv/dx &= -i/(\sigma W) \\ di/dx &= -(cW)\,dv/dt \end{aligned} \tag{2.4}$$

and by taking the derivative of the first equation with respect to *x* and substituting, one obtains

$$\frac{d^2 v}{dx^2} = \frac{c}{\sigma}\frac{dv}{dt} \tag{2.5}$$

This is the one-dimensional diffusion equation. Given $v(x=0) = v_0 e^{j\omega t}$ as the first boundary condition, which simply expresses the sinusoidal input signal, it can be solved with the ansatz $v(x,t) = v_0 e^{kx + j\omega t}$. Substituting this into Equation 2.5 yields

$$\begin{aligned} k^2 &= j\,c\,\omega/\sigma \\ k &= \sqrt{j\,c\,\omega/\sigma} = \pm(1+j)\sqrt{c\,\omega/2\sigma} \end{aligned} \tag{2.6}$$

The second boundary condition, stating that no current will reach the far end of an infinitely long, lossy transmission line, is $i(x=\infty)=0$. Taking this into account and integrating Equation 2.4 gives

$$\begin{aligned} i(x,t) &= \int -cW\frac{dv}{dt}dx \\ &= -cj\omega W v(x,t)/k \\ &= \mp\sqrt{jc\sigma\omega}\cdot W\cdot v(x,t) \end{aligned} \tag{2.7}$$

This result can be restated in terms of the characteristic transmission-line impedance, $Z_{TL}=v/i$:

$$\begin{aligned} Z_{TL} &= \mp\frac{1}{W\sqrt{jc\sigma\omega}} \\ &= \mp(1-j)\frac{1}{W\sqrt{2c\sigma\omega}} \end{aligned} \tag{2.8}$$

There are two orthogonal solutions for the time- and space-dependent voltage in this infinite transmission line, corresponding to right-moving and left-moving waves. Because *k* is complex (Equation 2.6), with equal real and imaginary parts, these are transient waves which decay with a characteristic decay length *equal* to their wavelength.

2.2.2 Finite transmission line

A real RC transmission line, such as the organic thin-film transistor shown in Figure 2.2, is not infinitely long. To simplify the boundary conditions, imagine the finite-length RC transmission line with its two ends shorted together. (This is the setup I use in my measurements, to be described in Section 2.4). This gives the boundary conditions,

$$\begin{aligned} v(x=0,t) &= v_0 e^{j\omega t} \\ v(x=L,t) &= v_0 e^{j\omega t} \end{aligned} \tag{2.9}$$

For this case, the expected solution is a sum of right-moving and left-moving waves. Exploiting the symmetry of the transmission line around the point $x = L/2$, the following ansatz, which includes an unknown constant *K*, can be used:

$$v(x,t) = v_0 e^{j\omega t} \cdot \left[e^{k(x-L/2)} + e^{-k(x-L/2)} \right] \cdot K \tag{2.10}$$

Substituting this formula into either of the two boundary condition in Equations 2.9 gives the value of the constant:

$$\begin{aligned} e^{kL/2} + e^{-kL/2} &= 1/K \\ K &= \frac{1}{2\cosh(kL/2)} \end{aligned} \tag{2.11}$$

The further substitution $\lambda = kL/2 = \sqrt{jc\omega/\sigma}\,(L/2)$ allows the voltage to be rewritten as

$$v(x,t) = v_0 e^{j\omega t} \frac{\cosh\lambda(1-2x/L)}{\cosh\lambda} \tag{2.12}$$

Again, integrating Equation 2.4 gives the current,

$$\begin{aligned} i(x,t) &= \int -cW\frac{dv}{dt}\,dx \\ &= -j\omega cW \int v(x,t)\,dx \\ &= -j\omega W c v_0 e^{j\omega t} \frac{-\frac{L}{2\lambda}\sinh\lambda(1-2x/L)}{\cosh\lambda} \\ &= \frac{1}{2} j\omega W c L v_0 e^{j\omega t} \frac{\sinh\lambda(1-2x/L)}{\lambda\cosh\lambda} \\ &\text{(substituting } j\omega c = 4\lambda^2\sigma/L^2\text{)} \\ &= 2\sigma\frac{W}{L} v_0 e^{j\omega t} \frac{\lambda\sinh\lambda(1-2x/L)}{\cosh\lambda} \end{aligned} \tag{2.13}$$

At the left end of the channel, the current is

$$i(0,t) = 2\sigma\frac{W}{L} v(0,t)\lambda\tanh\lambda \tag{2.14}$$

and at the right end, $i(L,t) = -i(0,t)$. Thus the total current through the semiconductor channel is twice the current at the left end, and the total admittance of the channel is

$$Y = \frac{2\,i(0,t)}{v(0,t)} = 4\sigma\,(W/L)\lambda\tanh\lambda \tag{2.15}$$

Exploiting the fact that $\mathrm{Re}\{\lambda\} = \mathrm{Im}\{\lambda\}$, analytical expressions for the real and imaginary parts of the admittance can be obtained after some lengthy algebra:

$$G = \mathrm{Re}\{Y\} = 2\sigma\, z\,(W/L)\cdot\frac{\sinh 2z - \sin 2z}{\sinh^2 z + \cos^2 z}$$
$$B = \mathrm{Im}\{Y\} = 2\sigma\, z\,(W/L)\cdot\frac{\sinh 2z + \sin 2z}{\sinh^2 z + \cos^2 z} \quad \text{where } z = \sqrt{c\,\omega/2\sigma}\,(L/2) \tag{2.16}$$

(The admittance, *Y*, is the complex generalization of the conductance, and its real and imaginary parts are known as the conductance, *G*, and the susceptance, *B*, respectively.) The parameter *z* is a unitless, real quantity which expresses the ratio of the *total* length of the transmission line to the decay length of the transient waves. That is, when $z \gg 1$, the applied voltage $v(0,t) = v(L,t)$ decays to near zero within a short distance from the ends of the transmission line, while when $z \ll 1$, the voltage remains nearly constant over the length of the device.

2.2.3 Limiting cases of finite-length transmission line

It is useful to consider the behavior of Equations 2.7 in the low frequency ($z \ll 1$) and high frequency ($z \gg 1$) limits. To derive the admittance of the transmission line in the $z \ll 1$ limit, I use the first-order Taylor expansions of the trigonometric and hyperbolic functions, $\sin x \approx \sinh x \approx x$ and $\cos x \approx \cosh x \approx 1$. Substituting these into Equations 2.7 yields,

$$\begin{aligned} G &= \mathrm{Re}\{Y\} \approx 0 \\ B &= \mathrm{Im}\{Y\} \approx 2\sigma\, z\,(W/L)\cdot 4z \\ &\approx 8\sigma\, z^2 (W/L) \\ &= \omega(c\,W\,L) \end{aligned} \tag{2.17}$$

In the low-*z* limit, where there is little spatial variation of the voltage in the transmission line, it behaves like a simple parallel-plate capacitor.

In the $z \gg 1$ limit, the difference between *G* and *B* is negligible, because $\sinh z \gg \sin z, \cos z$. Making the high-*z* approximation $\sinh z \approx e^z/2$ in Equations 2.7,

$$\begin{aligned} Y(z=\infty) &= 2\sigma z(W/L)\frac{e^{2z}/2}{e^{2z}/4} \\ &= (4\sigma W)\sqrt{jc\omega/8\sigma} \\ &= \left(\frac{1+j}{\sqrt{2}}\right)\frac{4W}{\sqrt{4/c\omega\sigma}} \\ &= 2W\sqrt{jc\sigma\omega} \\ &= 2/Z_{TL} \end{aligned} \tag{2.18}$$

where Z_{TL}, the classic result for the impedance of an infinite *RC* transmission line, was previously derived in Equation 2.8. In the high-*z* limit, the propagation distance of the wave into the transmission line is much shorter than the total length, and each end acts as an independent single-ended infinite transmission line. This case is thus equivalent to two infinite-length transmission lines in parallel.

2.2.4 Expected device behavior

Using Equations 2.7, the expected behavior of an RC transmission line can be plotted over a range of frequencies. According to this model, admittance depends only on frequency-independent *c* and *r*, with the entire frequency-dependence encapsulated by *z*, a unitless measure of effective device length.

The low-frequency regime corresponds to $z \ll 1$, while the high-frequency regime corresponds to $z \gg 1$. The crossover point is at $z = 1$ or $f = 4\sigma/\pi c L^2$ (where

$f = \omega/2\pi$ is the ordinary frequency). Figure 2.4 shows the scaling of G and B with respect to the frequency of the applied ac signal:

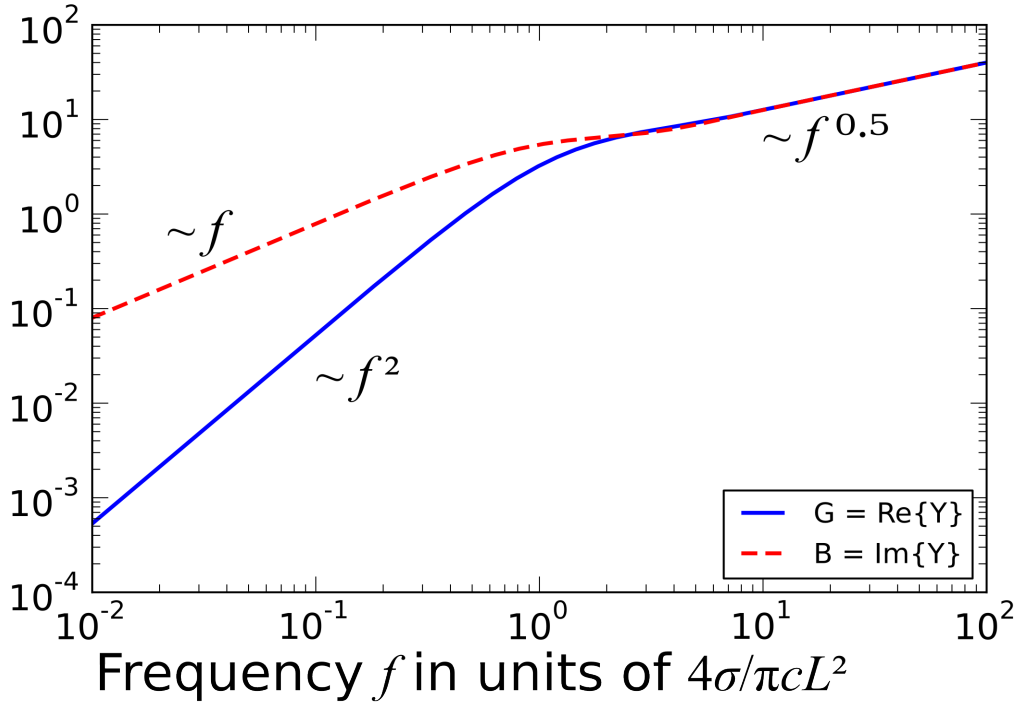

Figure 2.4: Scaling of real and imaginary components of the admittance of a finite-length RC transmission line with frequency, from Equations 2.7.

In the low-frequency or low-z limit, the characteristic decay length is much longer than the device length, so there is little spatial variation of $v(x,t)$ over the length of the device. Therefore, the device behaves like a large capacitor, $Y = j\omega(cWL)$, as shown in Section 2.2.4; the susceptance (B) is proportional to ω, and the conductance (G) falls off rapidly at low frequencies, so that the in-phase current is negligible.

In the high-frequency or high-z limit, on the other hand, the decay length is much shorter than the device length, so it is effectively an *infinite* RC transmission line, and

thus the real and imaginary parts of the admittance are equal. (This result was derived in Section 2.2.1 and confirmed as the limiting case of a finite transmission line in Section 2.2.4.)

2.3 Devices studied

I used the transmission-line framework introduced in Section 2.2 to study polycrystalline pentacene thin-film transistors (TFTs). I fabricated bottom-contacted pentacene devices on 300 nm thermally-grown SiO_2 on heavily doped silicon, which serves as the gate electrode. Gold electrodes of 50 nm thickness were deposited by thermal evaporation through a shadow mask.

As the source material, I used 99.9% pure powdered pentacene, purchased from Sigma-Aldrich (part number 684848). I followed the method of Gomar-Nadal et al. [20] to purify the pentacene: by heating the powder to just below its sublimation point before opening the shutter. The pentacenequinone impurity sublimates out of the pentacene prior to deposition. The pentacene was thermally evaporated through a shadow mask, depositing at a rate of roughly 0.006 nm/s to a thickness of 23 nm.

2.4 Measurement setup

After fabrication, I placed the devices in a Desert Cryogenics vacuum probe station ($P < 10^{-6}$ Torr) to maintain stability of the pentacene. My devices remained in this environment for the duration of the measurements. Devices were contacted via electrical feedthroughs connecting to mechanical probes mounted on micropositioners which I manipulated with the aid of a microscope and camera.

Because the goal of this research was to determine if ac transport in these devices is straightforwardly related to dc transport, it was crucial to measure the dc transport properties of the devices accurately. A number of features of organic semiconductors make this difficult. One problem is that of the bias stress effect, in which the prolonged application of a gate field causes significant shifts in the threshold voltage of a transistor. This effect has been variously explained by charge carrier trapping at the semiconductor-dielectric interface, slow movement of ions in the dielectric, and formation of defects in the semiconductor itself [54-57]. In my devices, I often observed shifts of around 10 V in V_T as the gate-source voltage was swept over the range of ±50 V during a period of 10^3-10^4 s. Regardless of the precise origin of the bias stress effect, it is difficult to compare the ac characteristics of a device to its dc characteristics, when it is likely that the measurement process itself is changing those characteristics. In order to accurately measure the very small ac admittance of my devices over several decades of frequency, it was necessary to use long integration times, with the result that a complete set of ac measurements could take several hours (~ 10^4 s) in some cases.

In addition to the mostly-reversible effect of bias stress, my thin-film transistors sometimes suffered permanent failures in the form of damaged contacts and short circuits between the semiconductor channel and the back gate. While dry thermal oxide has an average breakdown strength around 0.9 V/nm [58], there can be substantial variation and defects [59]. Thus I sometimes damaged the gate dielectric on 300 nm SiO_2 wafers while applying gate voltages of no more than ±70 V.

In my first experiments, I first measured a device's dc characteristics completely, over a range of gate and drain-source bias voltages, and then secondly measured its ac characteristics completely. I found this unsatisfactory, as it did not properly account for bias stress effect, breakdown, or other irreversible changes in the devices under test, making it nearly impossible to correlate the dc and ac transport data in a reasonable manner.

I subsequently developed a technique to interleave dc and ac measurements in order to minimize the delay between the collection of the two sets of data. The procedure is as follows:

(1) start at a certain gate-source voltage, V_{GS} (e.g. +50 V)

(2) sweep the drain-source bias voltage, V_{DS}, over the linear region (e.g. ±5 V) to measure dc conductance

(3) electronically reconfigure the circuit for ac measurement (see below)

(4) measure transmission-line ac conductance over the frequency range 50 Hz-20 kHz, without changing the gate bias

(5) adjust V_{GS} to the next value desired (typically 10 V steps) and repeat from step 1

I found that the bias stress effect was usually reduced when sweeping V_{GS} from more positive to negative values, and therefore made most of my measurements in this direction.

To measure dc transport properties, I used a pair of Keithley 2400 source-meters to apply V_{DS} and V_{GS}, and to measure I_D and I_G (though the gate leakage current

was negligible in non-damaged devices). I controlled them remotely via their GPIB interface. Figure 2.5 shows a schematic of this measurement setup:

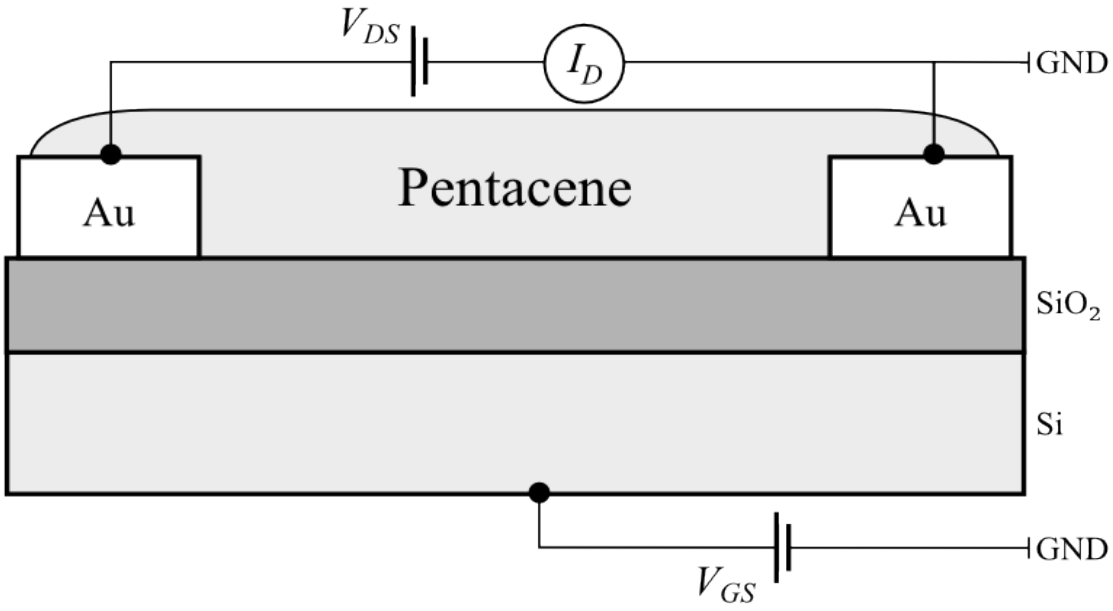

Figure 2.5: dc measurement setup for my pentacene TFTs

For ac characterization of these TFTs, I used a set of low-resistance mercury-wetted relays to electronically reconfigure the circuit to the transmission-line configuration, with the source and drain contacts shorted together, as described above in Section 2.2.2. Beyond allowing me to interleave and automate my measurements, this technique also has the important benefit of minimizing the need to mechanically manipulate the system, reducing contact cycles and thereby wear-and-tear on the gold electrodes, and helping to maintain consistent contact resistance and capacitance. Figure 2.6 shows a schematic of the ac measurement configuration for my devices:

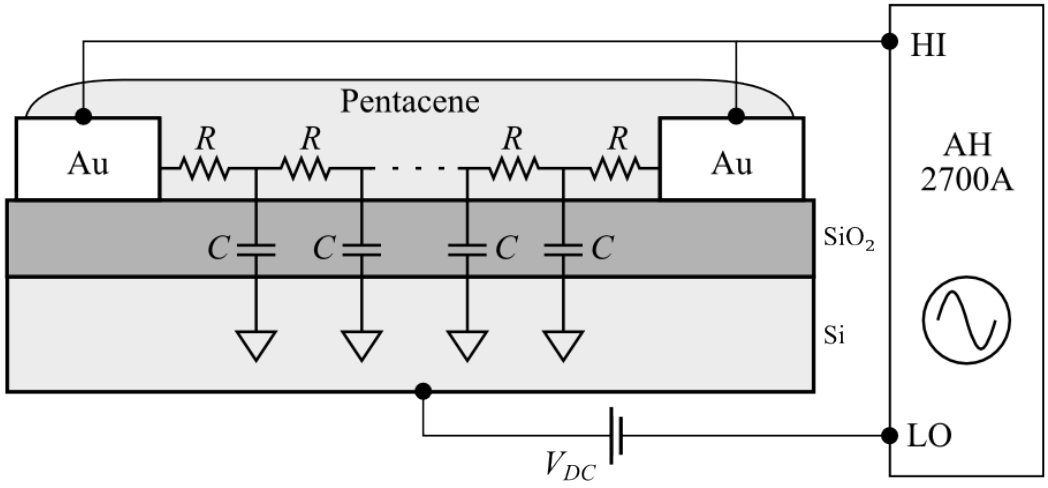

Figure 2.6: ac measurement setup for my pentacene TFTs

The schematic also shows the Andeen-Hagerling AH2700A capacitance bridge which I used to accurately measure ac admittance. The bridge is capable of measuring the complex admittance between its terminals, $Y(\omega)=G(\omega)+jB(\omega)$, to an extremely high precision, at 33 discrete logarithmically-spaced frequencies over the range $50\ \text{Hz} < f < 20\ \text{kHz}$. The source/drain electrodes were connected to the bridge's high terminal, while the back gate was connected to the bridge's low terminal, with a dc gate bias again provided by a Keithley 2400 source-meter. I kept the ac bias voltage under 1 V at all times to avoid driving the transistor into saturation.

It is important to understand that the conductance measured in the transmission-line configuration is *not* the conductance from source to drain. In particular, the transmission-line conductance is *zero* at $\omega=0$, while at finite frequency the transmission-line conductance results from the propagation of the ac signal into the lossy transmission line consisting of the pentacene film over the gate electrode.

2.5 Results of transmission-line measurements

I measured the dc characteristics of a large number of devices, with channel lengths ranging up to 2000 μm. For ac measurements, I concentrated on devices with longer channel lengths, since I wanted to observe the crossover between the low-frequency and high-frequency regimes, and was restricted to frequency range $50\ \text{Hz} < f < 20\ \text{kHz}$ by my measurement equipment (see Section 2.4). As described in Section 2.2.4, this crossover point occurs at $f = 4/\pi r c L^2$. Since the onset of the high-frequency regime is proportional to $1/L^2$, by studying devices with channel lengths exceeding 1000 μm I expected to observe high-frequency effects that would not appear below the 10^7-10^9 Hz range in TFTs with channel lengths of 1-10 μm.

Figure 2.7 shows the dc characteristics of a representative device, of channel length 1262 μm and width 1600 μm, on both logarithmic and linear scales. This device shows typical *p*-type field-effect behavior with a threshold voltage of approximately $V_T = -28\ V$, a field-effect mobility of 0.15 $\text{cm}^2/\text{V}\cdot\text{s}$, and an I_{on}/I_{off} ratio approaching 10^4. The off-conductance of approximately ~10 pS is probably *not* a true measure of the channel conductance but rather the noise floor of the Keithley 2400 source-meter (10 pS corresponds to a current of 50 pA at the maximum drain-source bias of 5 V). Shorter devices made on the same substrate showed I_{on}/I_{off} ratios exceeding 10^6, so the on/off ratio shown here is likely an underestimate of the true device characteristic.

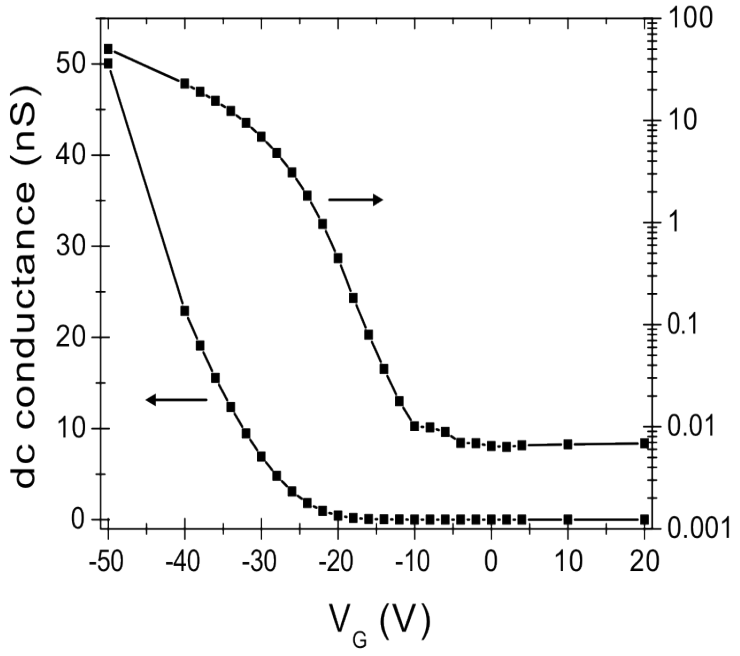

Figure 2.7: Transport characteristics of a pentacene TFT with channel length of 1262 μm, measured at DC at low bias ($|V_{DS}|<5$ V)

Figure 2.8 shows the gate-dependent ac admittance of the same device in the transmission-line configuration, split into its real component, the conductance $G(\omega)$, and its imaginary component, the susceptance $B(\omega)$. Measurement of these data were interleaved with measurement of the dc conductivity, using the techniques described in Section 2.4.

The susceptance of the gold source and drain electrodes, $B_C(\omega)=i\omega C_C$, has been subtracted from the total measured susceptance $B(\omega)$, so that Figure 2.8 shows only the susceptance due to the transmission line itself. The electrodes' capacitance is measured to be 89.59 pF, in excellent agreement with the value calculated from their combined area of 0.8 mm^2 and the nominal oxide thickness of 300 nm. I also made test

electrodes, on the same substrates, and found no variation of their capacitance from dc to 20 kHz, no variation with dc bias up to ±75 V, and a loss tangent of no more than 0.002. In this way, I accounted for the capacitance of the contacts, which is large, predictable, and easily measured, but not for any possible contact resistance; its effect will be discussed below.

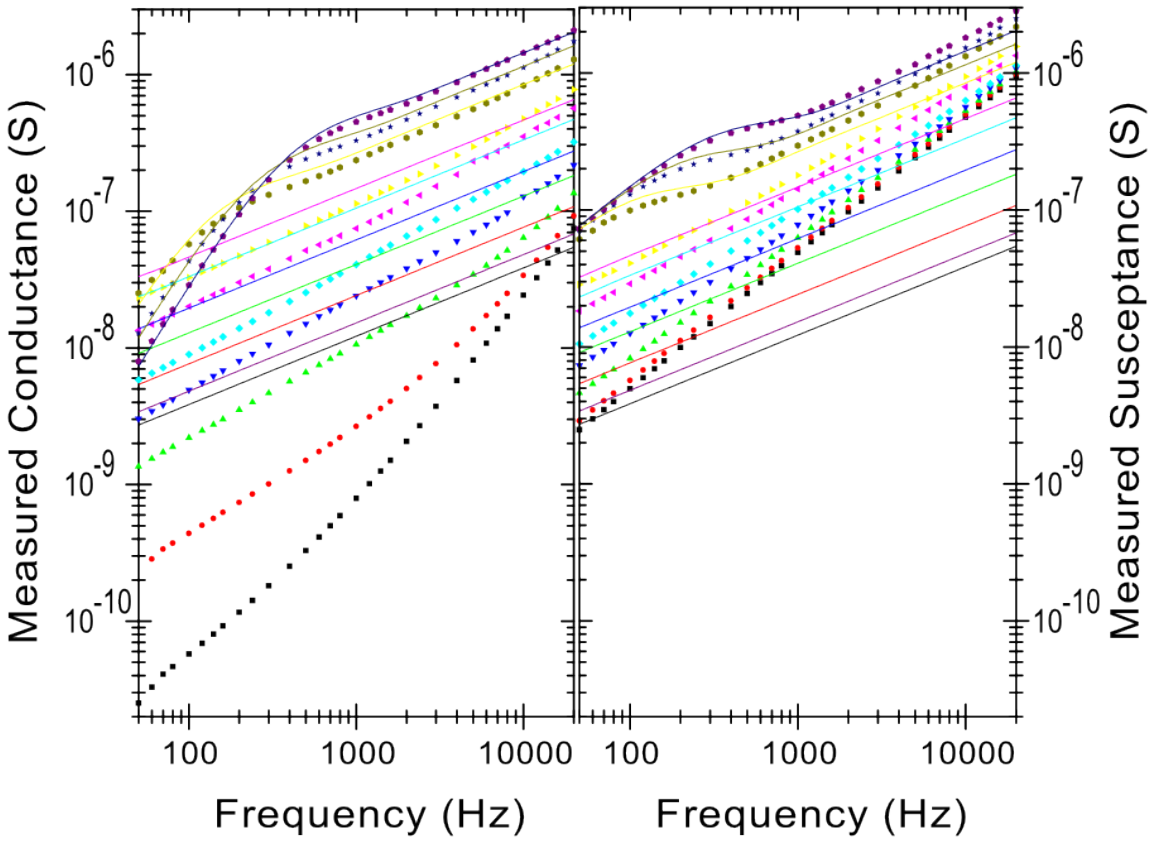

Figure 2.8: Conductance G(ω) and susceptance B(ω) of a pentacene TFT with channel length of 1262 μm. Solid symbols show measured data, while solid lines show the predicted admittance based on Equations 2.7 and the corresponding dc conductivity of the device (shown in Figure 2.7). Different colors correspond to different gate-source voltages; from top to bottom, they are: −50, −40, −30, −20, −16, −12, −10, −8, −6, and −4 V.

Figure 2.8 also shows lines representing the prediction of Equations 2.7. These have been calculated using the measured dc conductivity σ (calculated from the conductance shown in Figure 2.7) and the channel capacitance per unit area c, calculated from the oxide thickness and its dielectric constant (ε_r=3.9):

$$\sigma = \sigma_{DC} = G_{DC}(L/W)$$
$$c = \frac{\epsilon_0 \kappa_{oxide}}{d_{ox}} \tag{2.19}$$

There are no adjustable parameters in my model, which seeks to relate the measured conductivity of the film at dc to its ac transmission line admittance. Figure 2.8 shows good agreement between the experimental data and the model at low frequencies, for the most negative V_{GS} values, V_G = -30, -40, -50 V. In this regime, $V_{GS} < V_T$, so the *p*-type semiconductor channel is highly conducting. However, at higher frequencies and higher gate voltages the measured admittance data deviate from the model.

2.6 Possible explanations for the discrepancies

I considered several simplifying assumptions of the model described in Section 2.2.4, which might explain the discrepancies between the model and the data. Particularly notable is the observed departure from the predicted asymptotic high-frequency behavior, $G(\omega) = B(\omega) \sim \omega^{1/2}$. Figure 2.9, which plots the ratio $G(\omega)/B(\omega)$ for the experimental and theoretical data shown in Figure 2.8, demonstrates that the ratio $G(\omega)/B(\omega)$ falls below unity as the device is gated off by increasing gate voltage (that is, as V_G approaches and exceeds V_T, since it is a *p*-type device.)

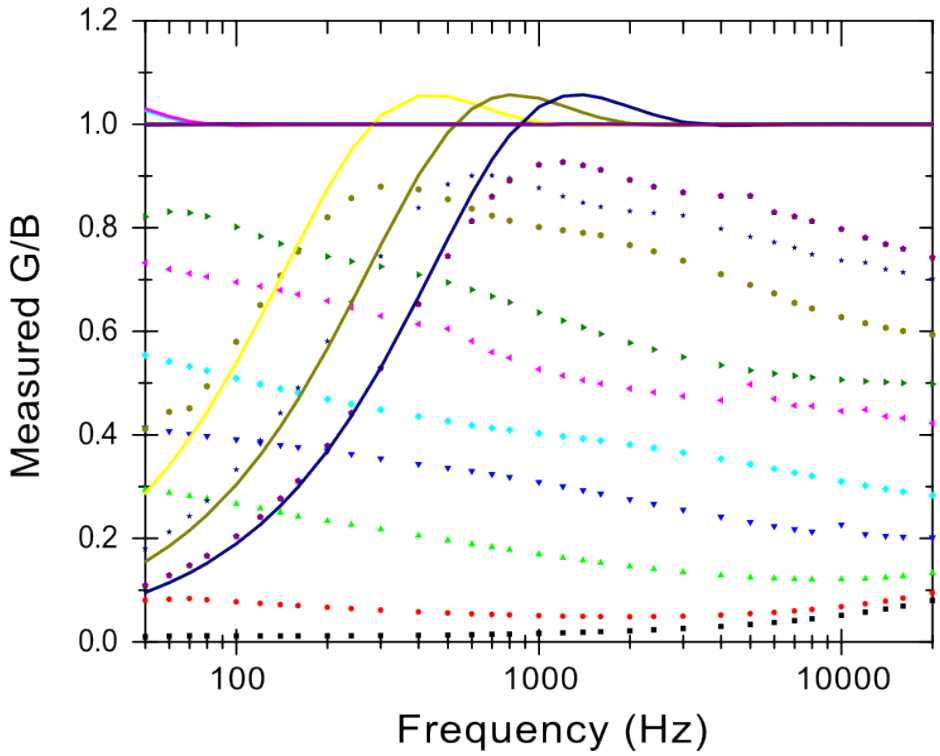

Figure 2.9: Ratio of conductance G(ω) to susceptance B(ω) for a pentacene TFT with channel length of 1262 μm (same data as in Figure 2.8). Solid symbols show measured data, while solid lines show the predicted ratio based on Equations 2.7 and the corresponding dc conductivity of the device (shown in Figure 2.7). Different colors correspond to different gate-source voltages; from top to bottom, they are: −50, −40, −30, −20, −16, −12, −10, −8, −6, and −4 V.

The experimental data of Figure 2.8 also shows both real and imaginary parts of admittance increasing faster than $\omega^{1/2}$ at the highest measured frequencies. This result also differs from the model of Section 2.2.4.

2.6.1 Contact resistance

A finite contact resistance, R_C, is present at the boundary between the gold electrodes and the thin film of pentacene evaporated on top of them. Previous experiments by Necliudov et al. on pentacene TFTs with channel lengths of 20-110 μm showed a complex dependence of contact resistance on contact geometry, contact metal, and gate and drain bias [60]. Blanchet et al. also observed a strong dependence of contact resistance on dielectric material for bottom-contacted pentacene TFTs [61].

However, contact resistance seems not to play a significant role in the transport properties of my long-channel pentacene TFTs. My colleague Adrian Southard developed a process for producing low contact-resistance, bottom-contacted pentacene transistors [7], which was used for the device whose transport properties are shown in Figure 2.7-Figure 2.8. By measuring devices with channel lengths in the range of 2 μm to 50 μm, I determined that the *contact* resistance of my pentacene TFTs was approximately equal to the *channel* resistance of a 1 μm-long sample in the highly-conducting on state. Therefore, for devices with L=1262 μm produced using the same process, the contact resistance is likely far less than 1% of the channel resistance.

Even if contact resistance *were* a significant fraction of the total device resistance, it would not affect the admittance of my transmission-line devices in the manner observed. The effect of contact resistant R_C in series with the transmission line is to set $1/R_C$ as an upper bound which conductance $G(\omega)$ cannot exceed. This is distinct from the behavior I observed, in which $G(\omega)$ actually increases *faster* than expected ($\sim\omega^{1/2}$ according to Equations 2.7), rather than being limited at high frequency.

Furthermore, gate-independent contact resistance would most noticeably affect the measured admittance in the regime of most negative V_{GS}, when the channel resistance is lowest. As shown in Figure 2.8, however, this is actually the regime in which my model (assuming zero contact resistance) most accurately predicts the experimentally measured admittance.

2.6.2 Frequency-dependent contact impedance

A model of gate- and frequency-independent contact resistance may be too simple to account for contact effects in my organic thin-film transistors. The contact impedance itself could depend on the frequency of the applied signal.

In experiments on poly(3-hexylthiophene) (P3HT) thin-film transistors, Hamadani et al. considered a contact capacitance C_C in parallel with frequency-independent R_C. Their schematic circuit model [52] is reproduced in Figure 2.10:

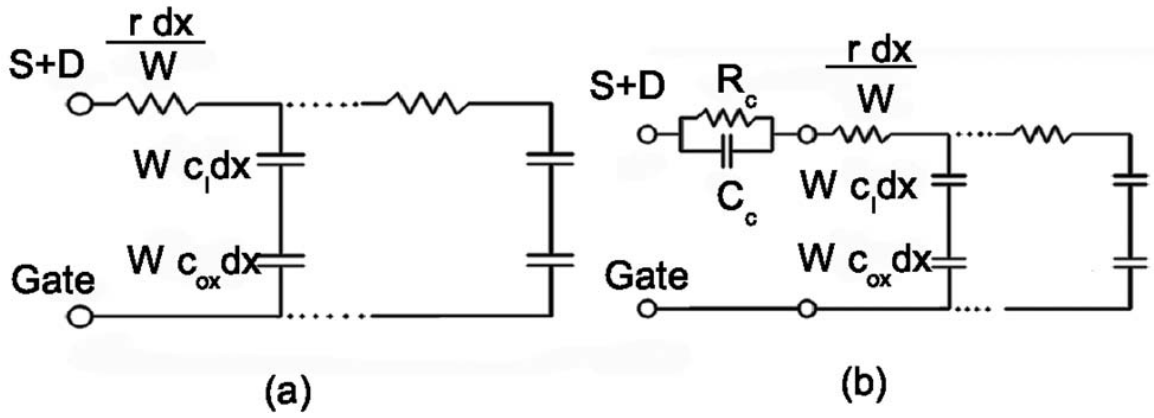

Figure 2.10: (a) Transmission-line circuit model used by Hamadani et al., similar to mine but additionally including interface capacitance (c_i). (b) Hamadani's model including contact impedance modeled as a parallel combination of resistance and capacitance. (From [52])

However, this too is unlikely to be responsible for the discrepancies between my model and the measured ac admittance. The impedance of the contact can be written as

$$\begin{aligned} Z_C &= \left(\frac{1}{R_C} + j\omega C_C \right)^{-1} \\ &= \left(1 - j\frac{\omega}{\omega_C} \right) \frac{R_C}{1 + (\omega/\omega_C)^2} \end{aligned} \quad \text{where } \omega_C = 1/R_C C_C \tag{2.20}$$

Determining the effect of this frequency-dependent contact in general is quite complex, as it requires a model of the contact in series with the frequency-dependent transmission line itself. Instead I will consider its effect in the limiting case of $z \gg 1$, which is evidently the regime in which my measurements differ most from the model's predictions.

In this limit, the channel impedance approximates that of two parallel, semi-infinite transmission lines, as discussed in Section 2.2.3:

$$\begin{aligned} Z &= (1-j)\frac{1}{2W\sqrt{2c\sigma\omega}} \\ &= (1-j)\frac{1}{\sigma\sqrt{\omega/\omega_{TL}}} \end{aligned} \quad \text{where } \omega_{TL} = \sigma/8cW^2 \tag{2.21}$$

The total impedance of the channel and contacts is thus

$$\begin{aligned} Z_{tot} &= Z_C + Z \\ &= \left(\frac{R_C}{1 + (\omega/\omega_C)^2} + \frac{1}{\sigma\sqrt{\omega/\omega_{TL}}} \right) - j\left(\frac{R_C}{\omega_C/\omega + \omega/\omega_C} + \frac{1}{\sigma\sqrt{\omega/\omega_{TL}}} \right) \end{aligned} \tag{2.22}$$

And the admittance, its reciprocal, is

$$Y_{tot} = 1/Z_{tot} = Z_{tot}^{*}/|Z_{tot}|^2 \tag{2.23}$$

Considering only the ratio of its real part, the conductance $G(\omega)$, and its imaginary part, the susceptance $B(\omega)$:

$$G(\omega)/B(\omega) = -\mathrm{Re}\{Z_{tot}\}/\mathrm{Im}\{Z_{tot}\} = \frac{\dfrac{R_C}{1+(\omega/\omega_C)^2} + \dfrac{1}{\sigma\sqrt{\omega/\omega_{TL}}}}{\dfrac{R_C}{\omega_C/\omega + \omega/\omega_C} + \dfrac{1}{\sigma\sqrt{\omega/\omega_{TL}}}} \tag{2.24}$$

The numerator and denominator differ only in the divisor of R_C. This demonstrates the dependence of the $G(\omega)/B(\omega)$ ratio on the contact frequency ω_C, in the $z \gg 1$ limit:

$$G(\omega)/B(\omega) = \begin{cases} <1 & \omega > \omega_C \\ =1 & \omega = \omega_C \\ >1 & \omega < \omega_C \end{cases} \tag{2.25}$$

This result is contrary to the experimental data, shown in Figure 2.8 and in Figure 2.9. Furthermore, it can be shown that the combined effect of R_C and C_C depresses both $G(\omega)$ and $B(\omega)$ below the model of Equations 2.3 in a broad band of frequencies centered around $\omega = \omega_C$; this contrasts with the previously mentioned experimental finding of enhanced $G(\omega)$ and $B(\omega)$ at high frequencies. Thus, a significant complex impedance of the contacts does not explain the deviation of my experiments from the model.

2.6.3 Interface-trap capacitance

I also considered the possibility that the channel-to-gate capacitance c might be gate-dependent.

Interface-trap capacitance at the boundary between the semiconductor film and the gate dielectric would reduce c, by inserting a small additional capacitance in series with the oxide capacitance. This effect may result from the movement of the Fermi level through the disordered distribution of electronic states in the organic semiconductor [52].

Hamadani's transmission-line model, as shown in Figure 2.10, includes such a capacitance (labeled c_i in contrast to the oxide capacitance c_{ox}), which was found to improve the agreement of the transmission-line model with the measured high-frequency admittance of P3HT [52].

Notwithstanding the merits of including interface-trap capacitance, Equations 2.3 predict that for *any* real conductivity r and capacitance per unit area c, $G(\omega)=B(\omega)$ in the high-frequency, high-z limit. As shown in Figure 2.9, this does not hold for my devices, where the ratio $G(\omega)/B(\omega)$ falls below the theoretically predicted values, especially as the device is gated off by increasing V_G. The systematic deviation of $G(\omega)/B(\omega)$ to values less than unity at high frequency is a central and persistent feature of my data, which is unexplained by the model thus far.

2.7 Generalization of transmission-line model

In Section 2.6, I have shown that the discrepancies between the measured admittance of my transmission-line device and the admittance calculated from its gate-dependent dc conductivity are not plausibly due to contact effects or interface-trap capacitance. In particular, the deviation of $G(\omega)/B(\omega)$ from unity at high frequencies (shown in Figure 2.9) is very difficult to explain.

These unexpected results especially appear when the device is gated off, that is not in a highly-conducting state. My model of a finite transmission line, developed in Section 2.2.2, is a very general one. There are, however, a couple of assumptions in this model which I have not yet questioned:

(1) The model assumes spatial uniformity of the transmission line; that is, the conductivity σ and capacitance per unit area c are assumed to be constant along its length.

(2) The model assumes that σ and c are real and frequency-independent.

While my pentacene thin films are polycrystalline, the dimensions of the individual grains are probably on the order of 200-2000 nm [20],[32]. In the long-device limit (low z), the length scale probed is comparable to the total device length, which is much longer than the individual grain size, so the assumption of spatial uniformity is a reasonable one. In the short-device limit (high z), the length scale probed is indeed shorter than the total device length. Due to doping of the semiconductor near the contacts, and due to grain size effects, the devices may indeed be spatially non-uniform. However, as I will soon demonstrate, the characteristic decay length in my pentacene devices is at least an order of magnitude greater than the individual grain size over the entire range of frequencies and gate voltages studied (see Section 2.7.2). Thus I can neglect inhomogeneity of the pentacene thin-film on the scale of individual grains.

2.7.1 Extraction of complex conductivity

The remaining assumption is that σ and c are real and frequency-independent. While maintaining the assumption of spatial uniformity, I can generalize Equations 2.3 to allow a complex, frequency-dependent σ and c. However, since the capacitance is dominated by the oxide capacitance (the interface trap capacitance is at most a small frequency-independent correction), it is reasonable to keep the assumption of a purely

real and frequency-independent *c*. I do allow a complex, frequency-dependent sheet conductivity,

$$\sigma(\omega)=\sigma'(\omega)+j\sigma''(\omega) \tag{2.26}$$

An analytical derivation of $\sigma'(\omega)$ and $\sigma''(\omega)$ in terms of the measured device admittance $Y(\omega)$ would be length and not very useful for the present purposes, but Equations 2.3 can easily be numerically inverted in order to calculate $\sigma'(\omega)$ and $\sigma''(\omega)$ directly from measurements of $G(\omega)$ and $B(\omega)$.

It is important to understand the meaning of, and the relationship between, the complex *conductivity* and the complex *admittance*. The admittance $Y(\omega)$ is a property of the complete transmission-line device, such as the semi-infinite device shown schematically in Figure 2.3 or the more realistic finite-length model of my thin-film transistors as transmission lines, shown in Figure 2.6. The admittance of the complete device is a complex quantity simply because it is neither purely resistive, nor purely capacitive. A simple test circuit consisting of a number of identical resistors and capacitors arranged as in Figure 2.3 will show this behavior; in fact, I constructed such a circuit, and it performed as expected. This device shows clearly-differentiated high-frequency and low-frequency behavior, with the crossover point determined by its resistance and capacitance per unit length, as illustrated in Section 2.2.4,

The *conductivity* is a very different quantity: this is not a feature of the complete device geometry (though I am assuming it to be homogenous over the length of my devices), but rather a measurement of the semiconductor film itself. If I were to replace my pentacene films with a good metal, then I would expect the conductivity to be real and independent of frequency or gate bias voltage.

I performed the calculations to extract $\sigma'(\omega)$ and $\sigma''(\omega)$ from measurements of $G(\omega)$ and $B(\omega)$ for the pentacene TFT with channel length 1262 μm whose transport data were summarized in Figure 2.7 and Figure 2.8. The real and imaginary parts of the extracted conductivity are shown in Figure 2.11:

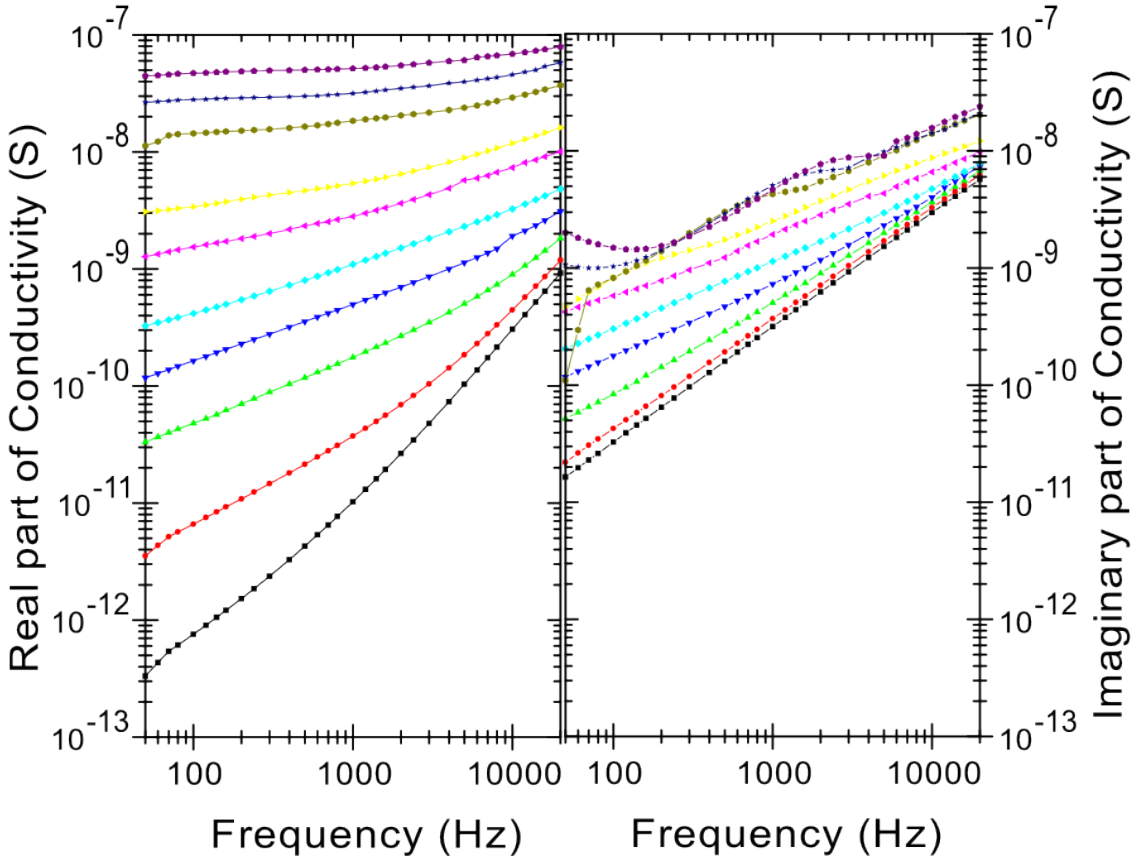

Figure 2.11: Real and imaginary components of the complex conductivity of a pentacene TFT with channel length of 1262 µm. This data was extracted from the conductance data in Figure 2.8 using Equations 2.16. Different colors correspond to different gate-source voltages; from top to bottom, they are: −50, −40, −30, −20, −16, −12, −10, −8, −6, and −4 V.

2.7.2 Description of results

The conductivity data in Figure 2.11 show a number of interesting features. At low frequency and large negative gate voltage, the real part of the conductivity dominates and it is nearly frequency-independent, as well as close to its dc value. That is,

$$\sigma'(\omega) \gg \sigma''(\omega)$$
$$\sigma'(\omega) \approx \sigma'(0) \tag{2.27}$$

However, at higher frequency and especially at V_{GS} above the threshold voltage V_T, $\sigma'(\omega)$ depends on frequency roughly as a power law, with an exponent that is apparently dependent on gate voltage. The imaginary part of the conductivity, $\sigma''(\omega)$, also shows power-law dependence on frequency, again with a gate-dependent exponent. In the highly-conducting on-state, $\sigma'(\omega) \gg \sigma''(\omega)$ as previously mentioned, but in the off-state $\sigma''(\omega)$ is comparable to $\sigma'(\omega)$ or even exceeds it. In the high-frequency, off-state limit (least negative V_{GS}), $\sigma''(\omega)$ is consistent with a capacitive rather than inductive reactance, further justifying the assumption of negligible inductance mentioned in Section 2.2.1.

Having calculated $\sigma'(\omega)$, the characteristic decay length l can be calculated from k, the complex wave-number of the RC transmission line, derived in Equation 2.1:

$$\begin{aligned} l &= \mathrm{Re}\{1/k\} \\ &= \mathrm{Re}\{\sqrt{\sigma / jc\omega}\} \\ &= \mathrm{Re}\{\sqrt{(\sigma''(\omega) - j\sigma'(\omega))}\}/\sqrt{c\omega} \end{aligned} \tag{2.28}$$

I find $l > 20$ μm at all frequencies and gate voltages for this device, as shown in Figure 2.12. This finding provides further justification for having neglected contact resistance, because the contact resistance is less than the resistance of a 1 μm-length strip of pentacene, as discussed in Section 2.6.1. The long decay length also justifies the assumption of spatial homogeneity discussed above. In polycrystalline pentacene produced using my deposition techniques, non-uniformities such as grain boundaries have a length scale <1 μm [20].

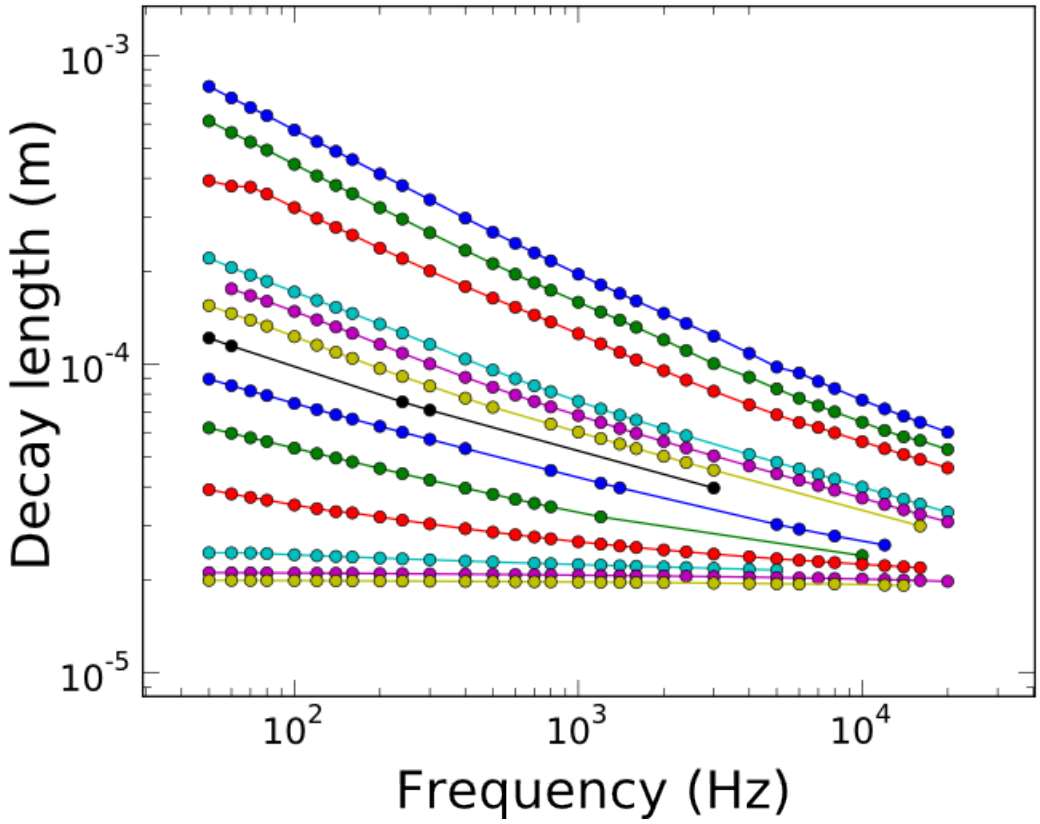

Figure 2.12: Characteristic RC decay length of a pentacene TFT with channel length of 1262 µm. Different colors correspond to different gate-source voltages; from top to bottom, they are: −50, −40, −30, −20, −18, −16, −12, −10, −8, −6, −4, and −2 V.

2.8 Theoretical explanations

Having measured the complex, gate-dependent conductivity $\sigma(\omega)=\sigma'(\omega)+j\sigma''(\omega)$ of my pentacene thin films, I tried to find a theoretical explanation for the observed frequency-dependence of the conductivity.

Electronic charge transport in organic semiconductors like pentacene has been explained by models of thermal trapping and release (for less disordered materials) and

by variable-range hopping (for more disordered materials) [38],[5], as discussed in Section 1.7. In general, hopping conduction in a disordered medium results in a frequency-dependent conductivity: as the frequency is increased, hopping events occur between localized sites which do not contribute to the dc conductivity but enhance the ac conductivity, which becomes complex [49]. Essentially, this is because there may exist many short paths with high hopping probabilities, while relatively fewer long paths have high hopping probabilities. At dc, at least one continuous conducting path (the percolation limit) must exist across the semiconductor in order for it to have a non-zero conductivity, but as frequency is increased carriers travel shorter and shorter distances before the direction is reversed; shorter conducting paths thus contribute increasingly to the ac conductivity.

2.8.1 Universal dielectric response

There must be a very wide range of hopping frequencies (that is, of continuous hopping paths) in order for conductivity to increase over many decades of frequency [49]. The conductivity will stop increasing only when the frequency exceeds the maximum hopping probability per unit time.

Dyre and Jonscher have observed that a wide range of disordered materials exhibit a "universal dielectric response" (UDR) [50],[51] in which the real and imaginary components of the conductivity follow a roughly power-law function of frequency,

$$\begin{aligned} \sigma'(\omega) &= \sigma'(0) + A\omega^s \\ \sigma''(\omega) &= B\omega^s \end{aligned} \tag{2.29}$$

where A and B are material-dependent constants, and the exponent s depends on temperature, with a typical value around 0.8. More recently, Xu et al. found UDR-like behavior in thin films (random percolative networks) of single-walled carbon nanotubes of varying densities [62].

Dyre constructs a random free-energy barrier model to try to reproduce this behavior. This model envisions a cubic lattice of localized sites with hopping between nearest neighbors. Although the hopping distances do not vary significantly, the attempt frequencies of jumps between neighboring follow a thermally activated distribution,

$$\Gamma = \Gamma_0 \exp\left(-\frac{\Delta F}{k_B T}\right) \tag{2.30}$$

where ΔF is known as the free-energy barrier. Using the continuous-time random walk method (CTRW) [63] and this distribution of attempt frequencies, Dyre derives formulas for the dc and ac conductivity of the system:

$$\begin{aligned} &\sigma(0) = (\ln\lambda)/6\tau \\ &\sigma(\omega) = \sigma(0)\frac{i\omega\tau}{\ln(1+i\omega\tau)} \quad \text{where} \quad \begin{matrix} \tau = 1/\gamma_{min} \\ \lambda = \gamma_{max}/\gamma_{min} \end{matrix} \end{aligned} \tag{2.31}$$

Here, γ_{min} and γ_{max} represent the lowest and highest probabilities per unit time, respectively, of hopping away from any of the localized sites participating in the conduction. Because $\sigma(\omega)$ has been found to be increasing up to frequencies around 10^{12} Hz for many realistic disordered materials, its high-frequency cutoff is neglected in Equations 2.31.

Equations 2.31 yield a frequency-dependent complex conductivity which corresponds with observations of many disordered solids, and which has a number of properties that seem to agree with my measurements on pentacene. In particular,

$\sigma'(\omega) \sim A\omega^s$ above a minimum frequency, with weak increase of the exponent *s* with respect to frequency, which agrees with the results shown in Figure 2.11 [49]. Dyre also predicts a specific temperature dependence of the ac conductivity, differing from that of the dc conductivity.

As formulated by Dyre, this model predicts nearly-constant σ' at low frequency, followed by an approximately power-law increase for many decades of frequency, finally reaching a high-frequency plateau (which is frequently ignored). This has been observed in a wide range of disordered and amorphous conducting materials, both those with ionic conduction as well as electronic conduction, as shown in Figure 2.13. Because of its broad applicability, it has been named Universal Dielectric Response (UDR) [50].

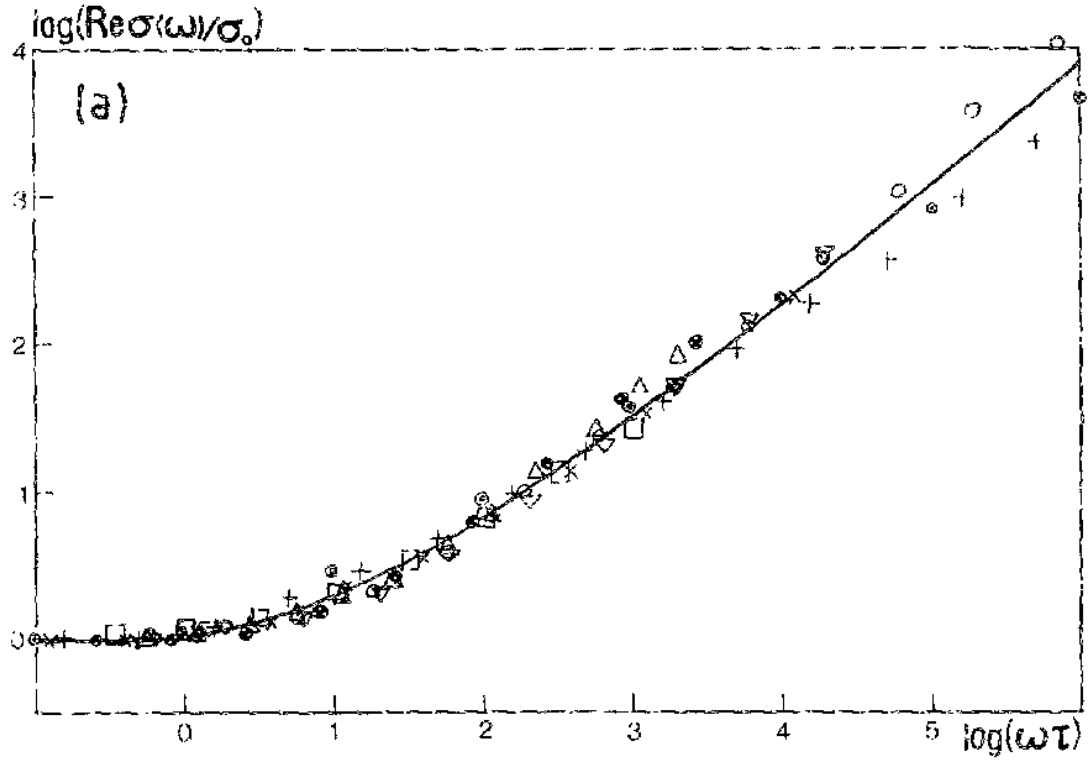

Figure 2.13: Universal dielectric response curve on a log-log plot. The solid line is the prediction of Dyre's random free-energy barrier model, while the symbols represent measurements of various materials, with τ a material-dependent fitting parameter: n-doped crystalline silicon (×), sputtered films of arsenic (●), sodium silicate glasses (⊙), glow-discharge silicon (△), silicon monoxide (+), amorphous germanium (□), $Mn_{1.8}Ni_{0.6}Co_{0.6}$ (▽), and monolayer of stearic acid (○). (From [49])

Note that the fitting parameter τ allows the curves shown in Figure 2.13 to scale to match each other's corner frequencies in the horizontal direction. However, the high-frequency behavior above the corner at $\omega = 1/\tau$ is independent of any fitting parameters and its surprisingly wide recurrence provides evidence for conformance to the "universal" behavior. Dyre demonstrates that above the corner frequency (e.g. $\omega \gg 1/\tau$

), Equations 2.31 will approximate the empirical power-law behavior of Equation 2.29, with an exponent *s* that shows only a weak, logarithmic dependence on frequency [49]:

$$s(\omega)=1-2/\ln(\omega\tau) \text{ where } \omega \gg 1/\tau \quad (2.32)$$

This exponent *s* is the slope of $\log\sigma'(\omega)$ with respect to $\log(\omega\tau)$, as seen in Figure 2.13. It asymptotically approaches unity at high frequency.

2.8.2 Applying UDR to my data on pentacene

My experimental conductivity data for pentacene (shown in Figure 2.11) show UDR-like frequency dependence over a large portion of the gate voltage and frequency ranges probed, with real and imaginary parts of the conductivity varying roughly as power laws with respect to frequency, $\sigma'(\omega)\sim A\omega^s$ and $\sigma''(\omega)\sim A\omega^s$. The exponents are the range of $0.5<s<1$, and furthermore they appear to slowly increase with frequency as predicted by Dyre in Equation 2.32.

To quantitatively evaluate my data within the UDR model, I performed least-squares fits of Equations 2.31 to the real part of my conductivity data. The UDR model of Schrøder and Dyre posits an inverse relationship between $\sigma'(0)$ and τ, $\tau=\epsilon_0\Delta\epsilon/\sigma'(0)$ where $\Delta\epsilon$ is related to the relative permittivity of the material [50]. (This consistent relationship between $\sigma'(0)$ and τ was also observed by Xu et al. for their thin films of SWNTs [62].) Initially, I left τ as the free parameter in my fits, with $\sigma'(0)$ determined from the dc transport data of Figure 2.7. This proved suboptimal, however, because of the significantly lower precision and greater noise of my dc measuring equipment. Therefore, I allowed $\sigma'(0)$ to vary as a free parameter instead, fitting the conductivity data for each gate voltage V_{GS}, with τ constrained by $\sigma'(0)\cdot\tau=k$

(k is a global fitting parameter over all values of V_{GS}). Figure 2.14 shows real conductivity ($\sigma'(\omega)$) data from Figure 2.11 alongside these fits. I excluded data for the highest gate voltages (most turned-off states of the device), because in these cases there was insufficient curvature in the graphs of $\log\sigma'(\omega)$ vs. $\log(\omega\tau)$ to extract the corner frequency $1/\tau$.

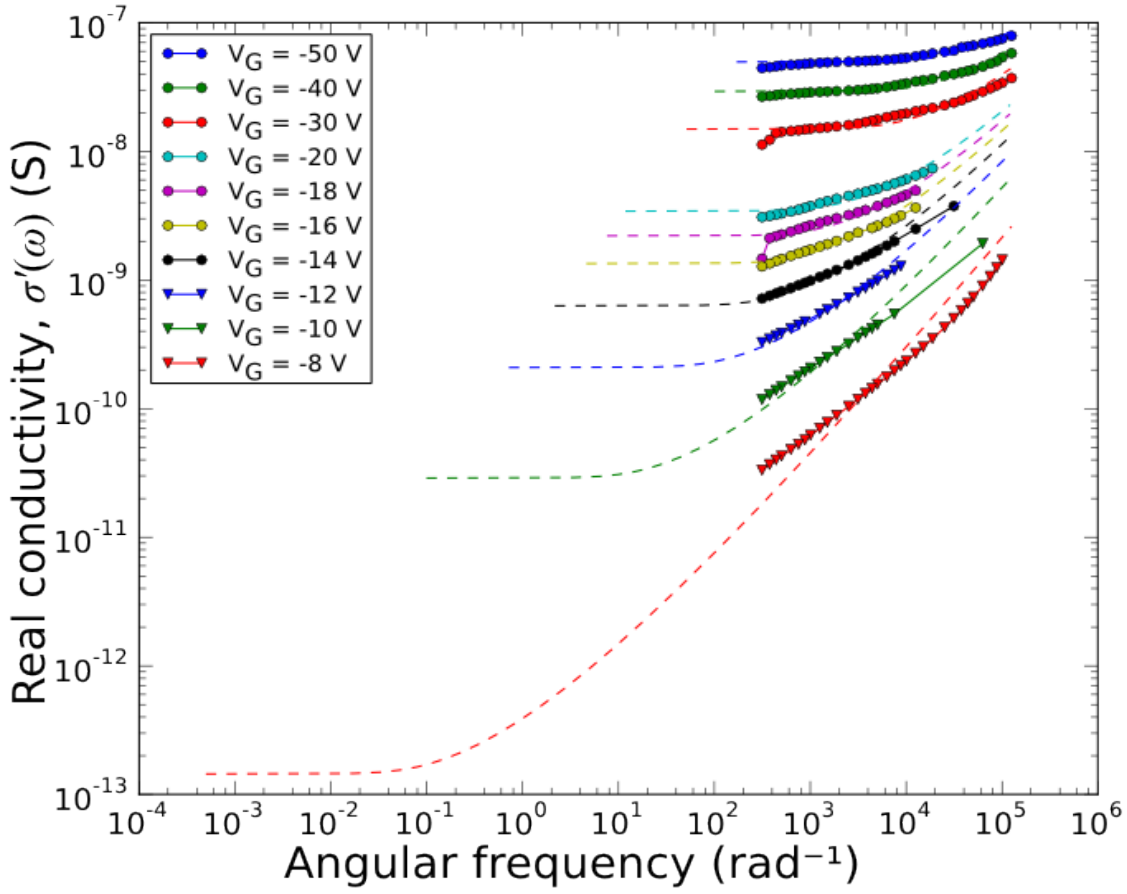

Figure 2.14: Real conductivity data from Figure 2.11 (solid symbols) with fits to the universal dielectric response model of Equations 2.31, allowing $\sigma'(0)$ as the free parameter for each fit, and $\sigma'(0)\cdot\tau = k$ with k a global fit parameter for all curves.

Figure 2.14 shows qualitatively good fits to Equations 2.31. From the fits to the individual curves, values of τ and $\sigma'(0)$ can be extracted, and I obtained the best fit with k=2.9×10^{-12} pF. With these parameters, the pentacene data can be plotted in a form identical to that of Figure 2.13 from Dyre, that is in the form of $\log[\sigma'(\omega)/\sigma(0)]$ vs. $\log(\omega\tau)$. In Figure 2.15 I show the data in this form:

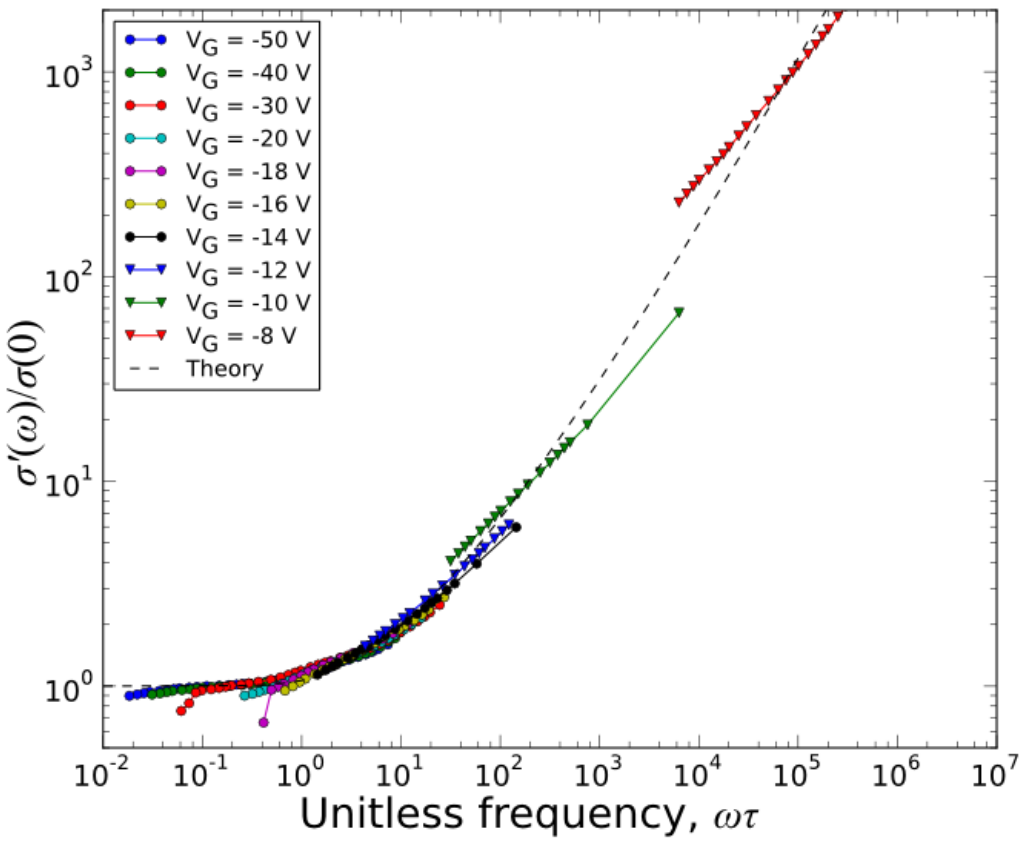

Figure 2.15: Real conductivity data from Figure 2.11 (solid symbols), having been fitted to the universal dielectric response model of Equations 2.31, recast to the form of the Universal Dielectric Response curve using the parameters τ and $\sigma'(0)$ obtained from the fits.

Unfortunately, my ac transport data (limited by the Andeen-Hagerling capacitance bridge I used) extends only over 2.6 decades in frequency, which makes it difficult to see the curvature of the universal dielectric response in any individual curve of Figure 2.15. However, the complete set of data, over a range of gate-source voltages from $V_{GS} = -50$ to -8 V, shows good agreement with the model. A persistent deviation from the UDR model occurs at low frequencies, below roughly f=150 Hz, and is seen in both Figure 2.14 and Figure 2.15.

It is also instructive to plot the fitting parameters used to fit the real conductivity data of my pentacene devices to the universal dielectric response curve. In Figure 2.16, I plot $1/\tau$ as well as $\sigma'(0)$, comparing the low-frequency conductivity from the fits with the values obtained from the dc transport data of Figure 2.7:

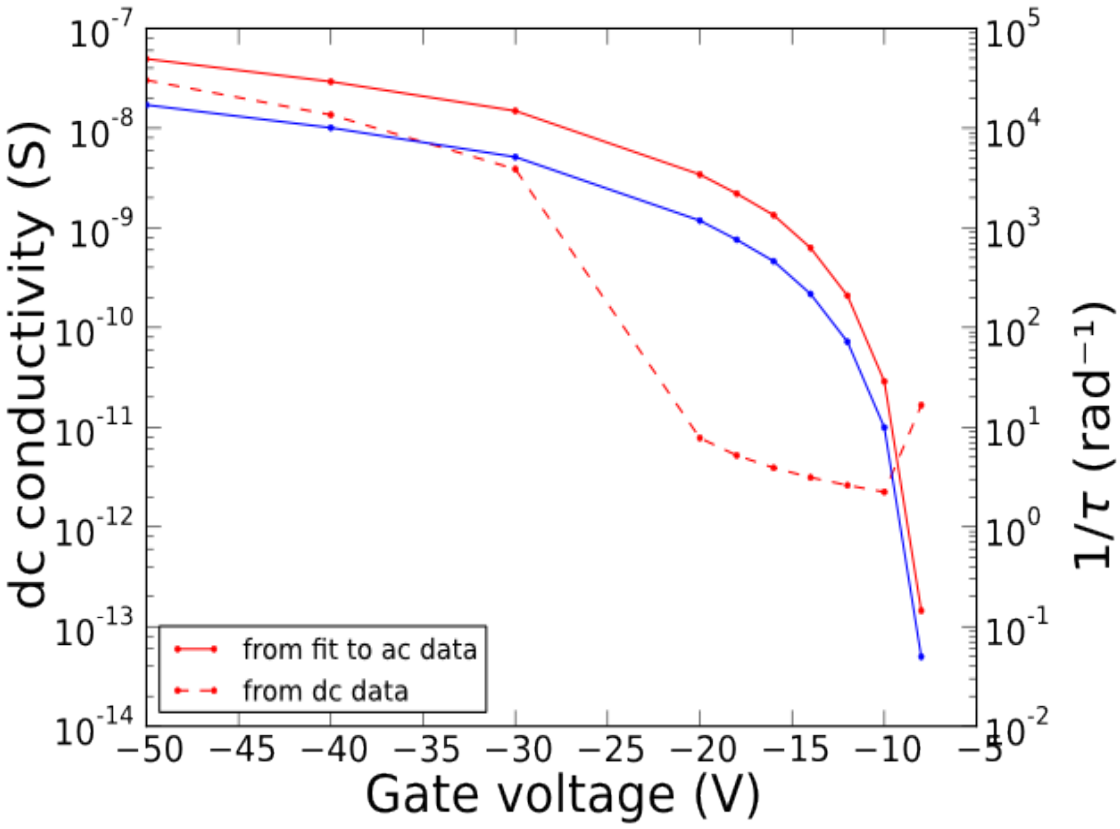

Figure 2.16: Fitting parameter $\sigma'(0)$ *(dc conductivity), and* $1/\tau = k/\sigma'(0)$ *(*τ *is the minimum hopping probability) from fits of the real ac conductivity data from Figure 2.11 to the universal dielectric response curves shown in Figure 2.14 and Figure 2.15, as a function of gate-source voltage. The values of* $\sigma'(0)$ *obtained from the ac fits are compared with those from the dc transport data for the same device, extracted from Figure 2.7. The global fitting parameter is* $k = \tau \cdot \sigma'(0) = 2.9 \times 10^{-12}$ pF .

Figure 2.15 shows a good fit using the assumption of an inverse relationship between τ and $\sigma'(0)$ (in particular the values obtained from fits to the ac data), lending support to the explanation of pentacene's ac conductivity in terms of the UDR model.. Recall from Section 2.8.1 above that $1/\tau = \gamma_{min}$, where γ_{min} is the minimum jump

probability between any two sites participating in ac transport through the disordered material. The correlation between γ_{min} and τ lends credence to Dyre's argument that the same fundamental processes limit dc and ac conduction in disordered materials [49]. Localized sites which are relatively inaccessible (low γ) limit both ac transport at low frequencies, as well as dc transport which requires a continuous hopping path through hopping sites across the organic semiconductor channel.

Schrøder and Dyre showed that UDR-type behavior can be observed under a very wide range of hopping conduction mechanisms [50]. These results thus cannot necessarily identify the exact mechanism of conduction in polycrystalline pentacene. However, analysis of pentacene's ac conductivity within the UDR framework can provide useful quantitative information about features such as hopping probabilities and their relation to dc conductivity.

2.9 Implications for practical applications

The frequency dependence of pentacene's conductivity will have profound consequences for practical applications of TFTs made from this material. For the devices discussed in this chapter, I define the on/off ratio at a given frequency in terms of the real component of the conductivity at the lowest and highest gate voltages measured, namely

$$r = \frac{\sigma'(\omega, V_{GS} = -50\ \mathrm{V})}{\sigma'(\omega, V_{GS} = -2\ \mathrm{V})} \tag{2.33}$$

A glance at Figure 2.11 shows that the on/off ratio of this device is rapidly reduced at high frequencies. In fact, it falls from $r \approx 10^5$ at 50 Hz to $r \approx 10^3$ at 20 kHz. This property would impede any applications of pentacene TFTs in CMOS-like

complementary logic circuits, which achieve low power consumption in part because of the extremely high on/off ratio of individual NMOS and PMOS field-effect transistors [64]. At more realistic operating frequencies of $>10^6$ Hz, pentacene TFTs will be extremely lossy in the off state. Furthermore, high off-currents will significantly reduce the noise margins of digital circuits built with pentacene TFTs.

The significant susceptivity $\sigma''(\omega)$ of pentacene also results in an effective parasitic capacitance between the source and drain electrodes. Looking at Figure 2.11, I find that the off-state susceptivity of my pentacene thin films is nearly proportional to applied frequency, ω:

$$\begin{aligned}\sigma''(\omega) &\approx (3\times 10^{-13}\ \text{S/Hz})\,\omega \\ &= (0.3\ \text{pF})\,\omega\end{aligned} \tag{2.34}$$

This parasitic capacitance, which is distinct from the *gate* capacitance of a thin-film transistor, may also be important in ac circuit models of pentacene transistors.

2.10 Conclusions and Future Work

2.10.1 Measurement technique

I have developed an ac circuit model of a thin-film transistor, describing this device as a lossy RC transmission line. This model predicts distinct regimes of frequency-dependent device conductance: at low frequencies, the device resembles a parallel-plate capacitor, while at high frequencies it resembles a semi-infinite transmission line. The crossover point appears at $\omega = 8\sigma / c\,L^2$, where L is the gate length, so by making devices that are considerably longer than the typical 1-10 μm gate

lengths of organic thin-film transistors, I can observe the transition between these different behaviors at relatively low frequencies (10^2-10^4 Hz for the devices described above).

The frequency-dependent admittance also depends on the 2D conductivity of the semiconductor film, σ, which can be modulated by varying the gate bias voltage. This enables a novel and accurate method of determining the mobility of a thin-film transistor: by varying the gate bias and performing ac measurements over a broad range of frequencies, one can observe the movement of the distinct frequency "corner" in the admittance (see Figure 2.4).

These techniques should be broadly applicable to measure the conductivity, $\sigma(\omega)$, of any semiconductor used in thin-film transistors. However, effects such as contact resistance and interface-trap capacitance (discussed in Section 2.6) may play a more significant role in other materials, thereby necessitating a more complex circuit model, such as the one used by Hamadani et al. to study the polymer semiconductor P3HT [52].

2.10.2 Frequency-dependent conductivity of pentacene

I used the RCTL measurement technique to study bottom-contacted thin-film transistors based on the organic semiconductor pentacene, comparing my ac measurements to dc transport measurements. I found significant discrepancies between the measured ac admittance and that predicted from the gate-dependent dc conductivity of the semiconductor.

Based on my ac admittance data, I extracted the conductivity of the pentacene, and found it to depend not only on the gate bias, but on the measurement frequency as well. These results show that pentacene is not purely a resistive material, but actually has a measurably complex conductivity at frequencies of 10^2-10^4 Hz. I argue that this behavior is due to disorder in polycrystalline pentacene thin films, which also results in hopping conduction at dc. This frequency-dependent conductivity is consistent with the Universal Dielectric Response model, which has previously been used to describe amorphous semiconductors, highly defected crystals, and other disordered conducting materials. Analysis of my conductivity data using the UDR model yields interesting results, such as a strong correlation between the minimum hopping probability within the material and its dc conductivity under varying gate bias (see Figure 2.16).

My results have significant implications for ac applications of pentacene TFTs. In my devices, pentacene's I_{on}/I_{off} ratio is greatly reduced at frequencies of only 10^4 Hz. The UDR model, which posits universal behavior of ac conduction in disordered materials, suggests that one of the ways to overcome this limitation would be to produce single-crystalline pentacene devices, or at least polycrystalline films with larger grain sizes, in which the transport is closer to band-like [18].

I expect that further studies on the frequency-dependent conductivity of single-crystal pentacene, as well as intentionally disordered devices, can provide additional insight into the nature of the disorder (structural or electronic) that gives rise to the frequency-dependent behavior. In particular, it is known that the grain size of pentacene thin films can be controlled by adjusting the temperature of the substrate during

deposition [32],[31], and that its grain size and dc transport are also strongly affected by the presence of pentacenequinone impurities [20] (see Section 1.6.3). It would be instructive to vary these parameters and to observe their effects on the parameters of ac conductivity measured by UDR, such as the hopping probability and the dc conductivity.

3. Introduction to graphene

3.1 Motivation

In this chapter, I will introduce graphene, a material with many promising nanoelectronics applications. After describing some of its basic properties and transport characteristics, I will focus in more detail on several techniques for fabricating graphene, and their advantages and disadvantages.

3.2 The structure of graphene

Graphene is a two-dimensional material, consisting of sp^2-bonded carbon atoms arranged in a hexagonal "chickenwire" lattice, with a bond length of about 0.14 nm, as shown in Figure 3.1. The thickness of a single layer, measured by the out-of-plane extension of the π orbitals, is around 0.34 nm [65]. Because of graphene's hexagonal lattice structure, it contains two equivalent simple hexagonal Bravais sub-lattices, generally known as the A and B lattices. Each unit cell thus contains two carbon atoms. Figure 3.1 shows a high-resolution transmission electron microscopy image of graphene [66]:

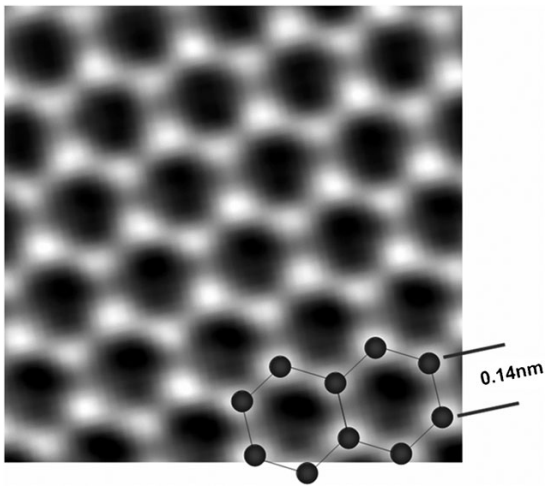

Figure 3.1: Image of single-layer graphene obtained by transmission electron microscopy (TEM), overlaid with ball-and-stick representation of the graphene lattice. (From [66])

Graphene has long been of theoretical interest, due to its simple structure and its relationship to other graphitic materials (e.g., carbon nanotubes are equivalent to graphene rolled up into a tube) [67]. Experimental interest has been very high since 2004, when researchers at the University of Manchester, UK, demonstrated production of graphene via mechanical exfoliation on insulating substrates, opening the possibility of electronic transport studies on this material (see Section 3.7.1) [68].

3.3 Electronic properties of graphene

Graphene's electronic properties can be calculated using the tight-binding approximation, which uses superposition of electronic wave-functions for individual atoms to calculate the band structure for an extended crystal. In graphene, the $2s$, $2p_x$ and $2p_y$ orbitals of the carbon atoms hybridize to form strong sp^2 or σ bonds with their

neighbors. The remaining π orbital is more weakly involved in bonding and is most important in determining the low-energy structure of graphene. The relationship between electronic energy E and the electron crystal momentum $\boldsymbol{k}$ for the π-derived bands of graphene was first calculated by Wallace within the tight-binding approximation, taking into account nearest and next-nearest neighbor hopping energies [69]. Ignoring next-nearest neighbor hopping (valid for energies close to the Fermi energy of charge-neutral graphene), the band structure can be written as

$$E(\boldsymbol{k}) = \pm\gamma_0\sqrt{1+4\cos(\sqrt{3}k_x a/2)\cos(k_y a/2)+4\cos^2(k_y a/2)} \tag{3.1}$$

E is measured relative to the Fermi energy of charge-neutral graphene. $a = 2.46$ Å is the lattice constant of one simple hexagonal sub-lattice of graphene (the previously mentioned bond length of 1.42 Å is in fact $a/\sqrt{3}$), and $\gamma_0 = 2.8$ eV is the nearest-neighbor hopping energy.

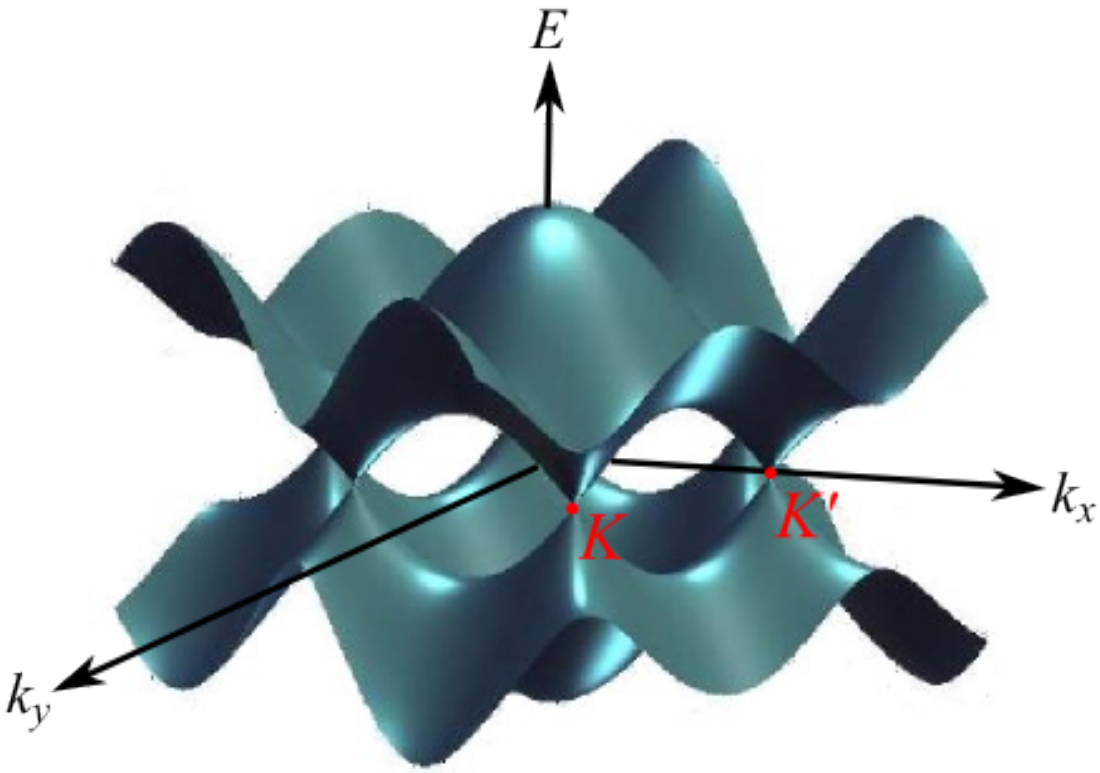

Figure 3.2: Electronic band structure of single-layer graphene, calculated from the tight-binding model using Equation 3.1. The K and K′ points, where the conduction and valence bands touch, are also shown (they correspond to the two equivalent sub-lattices).

Figure 3.2 shows the electronic band structure calculated using Equation 3.1. In the k_x-k_y plane, there are 6 points at which the valence and conduction bands of graphene touch. There are two distinguishable points called K and K'; the others differ from K or K' by a reciprocal lattice vector, and are thus equivalent to them by the symmetry of the lattice. In the vicinity of K and K', the energy dispersion is nearly linear, with the Fermi velocity as the proportionality constant, that is

$$E(\boldsymbol{k}) = \hbar v_F |\boldsymbol{k} - \boldsymbol{k}_K| \tag{3.2}$$

As a result of this linear or conical dispersion, graphene electrons at low energies are a model system for relativistic massless Dirac fermions, because they have energies that are proportional to their momenta.

3.3.1 High mobility, zero-gap semiconductor

According to Equation 3.1, the valence and conduction bands of graphene are perfectly symmetrical. Next-nearest neighbor hopping breaks this symmetry, but the effect is small for energies near zero. Thus one would expect a high degree of electron-hole symmetry in graphene, with similar conductivities for electrons and holes. Indeed, experiments have found the electron and hole mobilities (μ_e and μ_h) of pristine graphene to be similar and very large. Low-temperature experiments have shown that the mobility of graphene on SiO_2 substrates is nearly independent of temperature between 10 K and 100 K (in contrast to bulk graphite, where the mobility goes roughly as $1/T$ over this range), which shows that mobility is limited in this range by scattering from static disorder, rather than by temperature-dependent phonons [70]. Charged impurities in the substrate are thought to be the source of this disorder [71], and graphene to which such impurities have been intentionally added conforms to this model [72]. At room temperature, however, acoustic phonons limit the mobility of perfectly defect-free graphene to a theoretical value around 200,000 $cm^2/V \cdot s$ when suspended (that is, without a substrate). On oxidized silicon (SiO_2 on Si) substrates, scattering by polar optical phonons of the substrate actually have a much larger effect than scattering by phonons of graphene itself, so mobility is theoretically limited to about 40,000 $cm^2/V \cdot s$ on SiO_2 [70].

The highest-reported experimental mobilities of graphene on SiO_2 are over 15,000 $cm^2/V \cdot s$ at room temperature [67]. As this is around an order of magnitude higher than the electron mobility of state-of-the-art silicon devices [1], this has led to great interest in using graphene to augment or replace conventional CMOS electronics. However, as I mentioned above, graphene is a zero-gap semiconductor, since its valence and conduction bands touch at the *K* and *K'* points (as opposed to the 1.1 eV band gap of silicon). Because of this, field-effect transistor devices made from pristine graphene have poor I_{on}/I_{off} ratios, typically around 5-10 [73]. Figure 3.3 shows how the band gap of an intrinsic semiconductor like silicon exponentially suppresses its carrier density, whereas graphene at room temperature never reaches zero carrier density. The intrinsic carrier concentration in graphene is determined from the density of states of graphene near the Fermi level:

$$n_i = \int_0^\infty F(E)\, g(E)\, dE \tag{3.3}$$

where $F(E)$ is the Fermi-Dirac function and $g(E)$ is the density of states. From Equation 3.2, the 2D density of states for graphene (including the two-fold spin degeneracy) can be calculated as

$$g(E) = \frac{2E}{\pi \hbar^2 v_F^2} \tag{3.4}$$

Substituting Equation 3.4 into Equation 3.3, making a change of variables from *E* to $E/k_B T$, and substituting the well-known value of the first-order complete Fermi-Dirac integral [74] yields:

$$
\begin{aligned}
n_i &= \int_0^\infty \frac{2E}{\pi\hbar^2 v_F^2} \frac{1}{e^{E/k_B T}+1} dE \\
&= \frac{2}{\pi\hbar^2 v_F^2} \int_0^\infty \frac{E}{e^{E/k_B T}+1} dE \\
&= \frac{2(k_B T)^2}{\pi\hbar^2 v_F^2} \int_0^\infty \frac{E/k_B T}{e^{E/k_B T}+1} d(E/k_B T) \\
&= \frac{2(k_B T)^2}{\pi v_F^2} \cdot \frac{\pi^2}{12} = \frac{\pi}{6}\left(\frac{k_B T}{\hbar v_F}\right)^2
\end{aligned}
\tag{3.5}
$$

At room temperature (300 K) and assuming a Fermi velocity of 10^8 cm/s [75], Equation 3.5 gives an intrinsic carrier density of 8.1×10^{10} cm^{-2}. A similar calculation can be done for intrinsic silicon. As a three-dimensional semiconductor with a band gap, its electron density of states in the conduction band is [4]:

$$
g_c(E) = \frac{\sqrt{2}\, m_e^{*3/2}}{\pi^2\hbar^3} \sqrt{E - E_c} \tag{3.6}
$$

where m_e^* is the effective mass of electrons in the conduction band ($m_e^* \approx 1.08\, m_e$ for silicon [4]) and E_C is the energy level of the conduction band edge (equal to approximately half the band gap, $E_g/2$). Plugging Equation 3.6 into Equation 3.3 and numerically integrating yields 1.02×10^{10} cm^{-3} for the intrinsic electron density of silicon at 300 K, within a few percent of experimentally measured values [76].

In realistic samples of graphene, potential disorder due to charge impurities gives rise to inhomogeneous distributions ("puddles") of positive and negative charge at the Dirac point [71],[77]. As a result, the measured minimum conductivity is weakly dependent on disorder and is approximately $4e^2/h$ in dirty samples, and somewhat higher in clean samples [71].

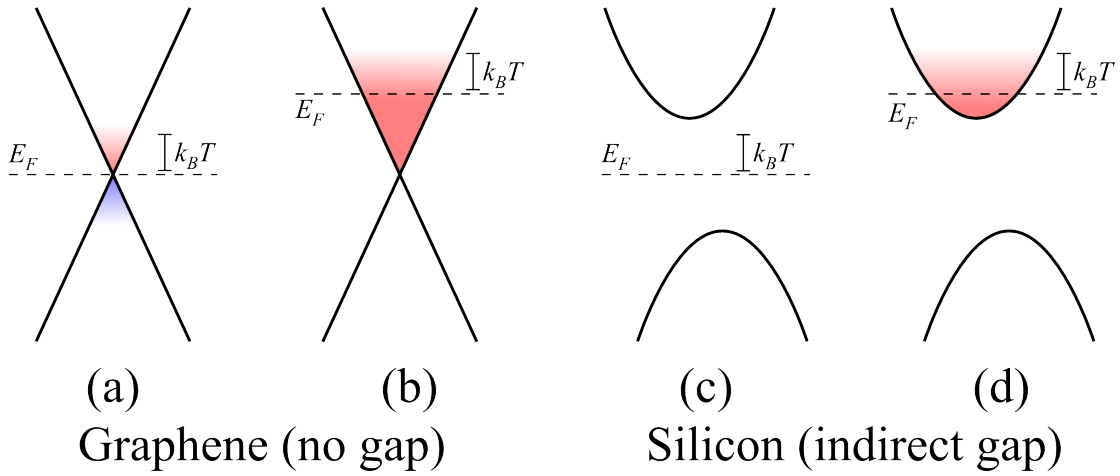

Figure 3.3: Schematic of the low-energy band structure of graphene (a,b) and silicon (c,d). (a) In unbiased graphene, with the Fermi energy at the Dirac point, there is a significant density of electron (red) and hole (blue) states within k_BT of the Fermi energy. (c) Because its band gap of 1.1 eV is much larger than k_BT (about 25 meV at 300 K, not drawn to scale), the carrier density of unbiased silicon is practically zero. (b,d) Intrinsic graphene and silicon both have much higher carrier densities when a non-zero gate bias voltage is applied.

3.4 Band gap engineering

I have previously discussed the importance of a high I_{on}/I_{off} ratio for low-power digital electronics applications in Chapter 2, in regards to organic semiconductors. In graphene, several techniques have been attempted to open a band gap and thereby increase the I_{on}/I_{off} ratio. Although I have not directly pursued strategies to engineer a band gap in graphene in my own thesis research, I include some discussion of efforts by other researchers toward this end, because much research is driven by this goal and

because its success will likely affect the range of future applications of graphene. For a recent review of this topic, see Fuhrer et al. [78].

3.4.1 Graphene nanoribbons

Graphene nanoribbons are strips of graphene with widths on the order of 1-100 nm. Calculations show that certain graphene nanoribbons will have a non-zero band gap [79]. However, this band gap depends crucially on the structure of the edges of the graphene ribbon. Two basic patterns of graphene edges are the armchair and zigzag shapes, shown in Figure 3.4.

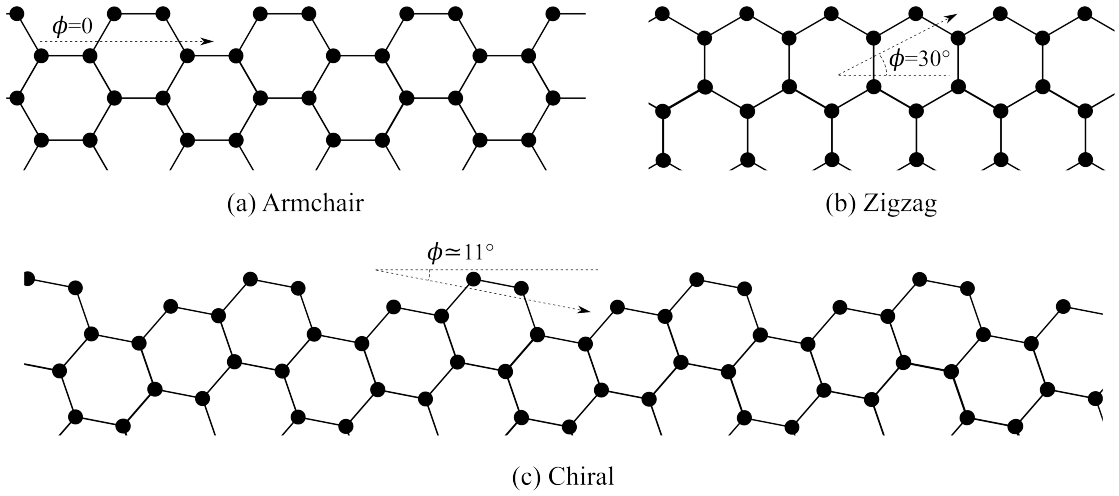

Figure 3.4: (a) Armchair and (b) zigzag shapes are among the possible edge structures for graphene nanoribbons. There are also an infinite number of possible repeating chiral edge structures, such as (c), which can be differentiated by their chiral angles. The chiral angle, ϕ, is defined as the minimal angle between the long axis of the nanoribbon and an armchair edge of the nanoribbon.

A number of researchers have calculated the electronic structure of graphene nanoribbons. Narrow graphene nanoribbons with armchair edges have a band gap that varies inversely with their width, and is around 0.5 eV for 3 nm width [79-81]. It has also been shown that this band gap decreases rapidly as the chiral angle (illustrated in Figure 3.4) is increased from 0° to 30°, so creating gapped graphene ribbons requires consistent edge structure [79].

Fabricating narrow graphene nanoribbons with armchair edges is difficult. Using electron-beam lithography, researchers at Columbia University made graphene nanoribbons as narrow as 15 nm, with energy gaps as high as 300 meV for the narrowest devices, but they were not able to precisely control the edge structure [82]. Another group demonstrated 2-3 nm-wide lithographically-patterned graphene nanoribbon FETs, and showed that their band gap was sufficient to achieve I_{on}/I_{off} ratios up to 10^6, with field-effect mobility around 150-200 $cm^2/V{\cdot}s$ [83]. In Sections 3.7.2 and 3.7.3, I discuss two novel methods to synthesize narrow graphene nanoribbons with consistent edge structure.

3.4.2 Bilayer graphene in a non-uniform electric field

Fundamentally, the lack of a band gap in graphene is a result of its great structural and consequently electronic symmetry: the density of states at energies $\pm E$ above and below the Dirac point are equivalent. Breaking this symmetry has inspired another approach to engineering a band gap in graphene. Bilayer graphene, stacked in the Bernal (or AB) arrangement consists of two sheets of graphene with half the atoms in each layer

directly above or below those in the other layer, while the other half lay directly above or below the centers of the other layer's hexagonal rings, as shown in Figure 3.5.

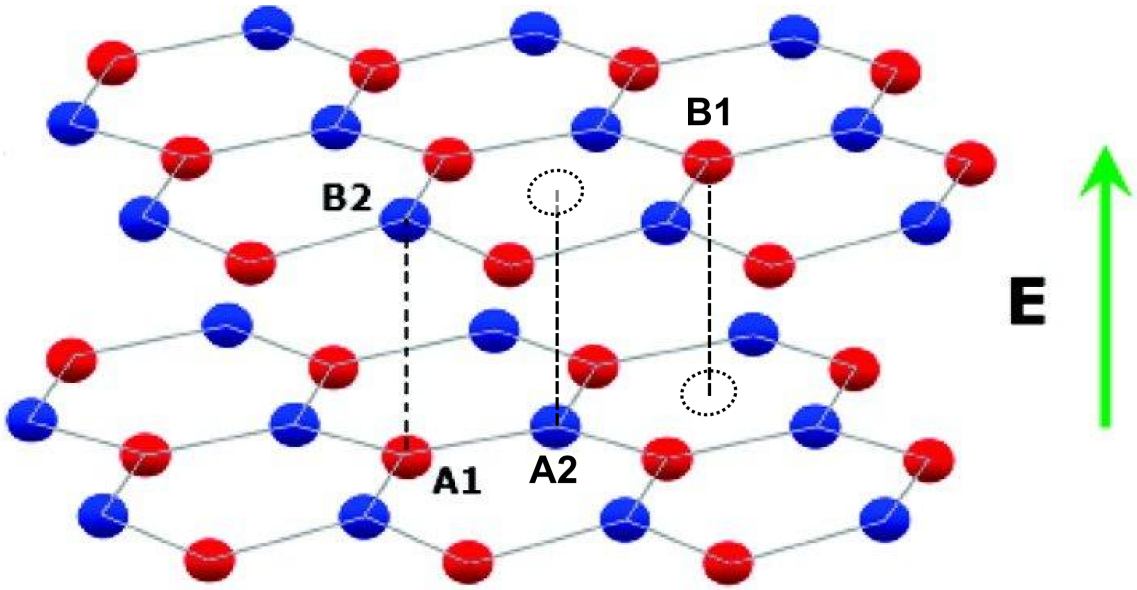

Figure 3.5: Bilayer graphene with the AB stacking arrangement. The atoms of the first layer's A sublattice lie directly below those of the second layer's B sublattice. Those of the first layer's B sublattice lie directly below the centers of the second layer's hexagonal rings, and vice versa. (Slightly modified from [73])

The band structure of bilayer graphene is more complex than that of single-layer graphene, but it possesses much the same structural symmetry, and it is also a zero-gap semiconductor [84-86]. However, applying a non-uniform vertical electric field to a graphene bilayer breaks this symmetry: not only does it move the Fermi energy, producing a net doping, but it also opens a gap between the valence and conduction bands [84],[87]. It is actually possible to control these two effects independently in order to make a gapped bilayer with the Fermi level in the middle of the conduction and valence bands [84].

Researchers at Delft University first demonstrated the opening of a band gap in bilayer graphene via the application of such electric fields [88]. They constructed a bilayer graphene field-effect transistor (FET) with both top and bottom gates, and showed that the device resistance greatly increased when the two gates were biased asymmetrically. They also observed temperature-dependent conductivity in this state, contrasting with the temperature-independent transport of symmetrically-biased devices, as evidence that a band gap was responsible for the increased resistance, rather than static charge disorder induced by the presence of the top gate [88]. Subsequently, groups at Berkeley and IBM have constructed similar devices and used the two gates to tune the combination of band gap and Fermi level [73],[84]. Figure 3.6, reproduced from [84], explains the device structure and transport measurements. The IBM group subsequently demonstrated a 130 meV band gap using an average electrical displacement of 2.2 V/nm [73]. Their devices achieved an I_{on}/I_{off} ratio of about 100 at room temperature, reaching 2,000 at 20 K.

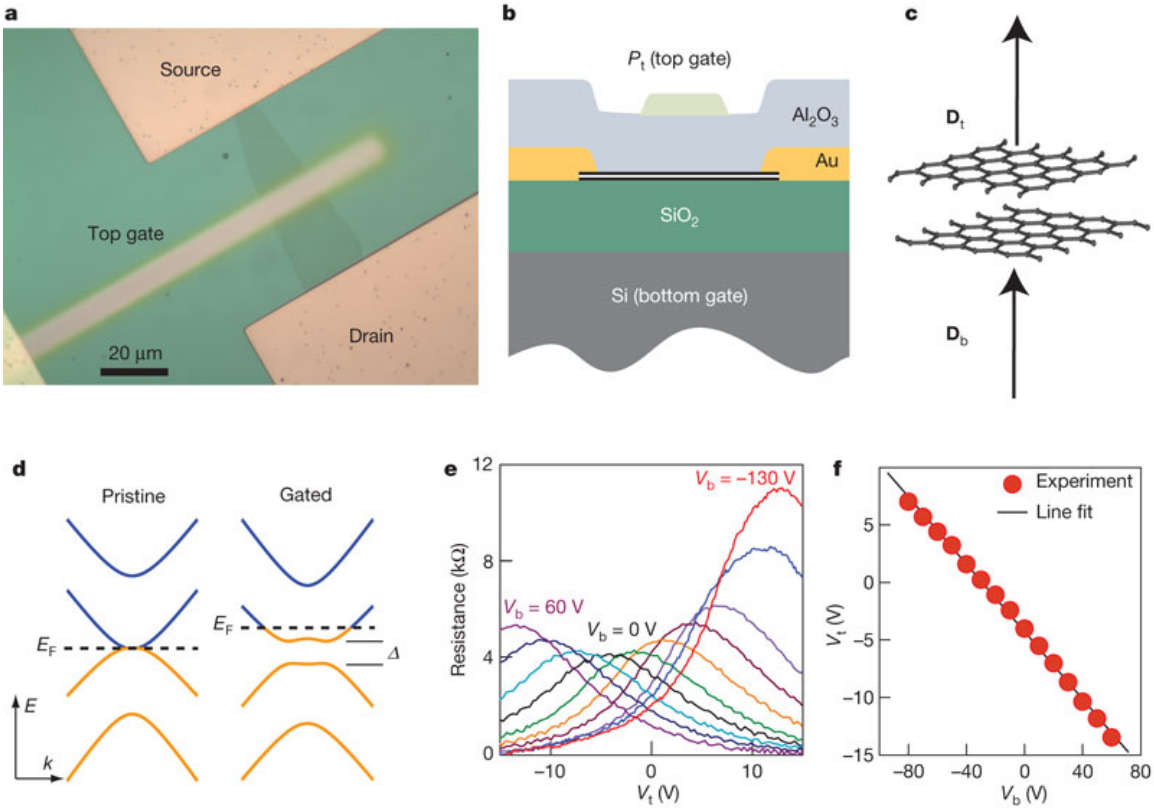

Figure 3.6: (a) Optical microscopy image of the bilayer device. (b) Cross-sectional side view of the gated device. (c) Sketch showing how gating of the bilayer induces top (D_t) and bottom (D_b) electrical displacement fields. (d) Left, the electronic structure of a pristine bilayer has zero bandgap. Right, upon gating, the displacement fields induce a non-zero bandgap Δ and a shift of the Fermi energy E_F. (e) Graphene electrical resistance as a function of top gate voltage V_t at different fixed bottom gate voltages V_b. The traces are taken with 20 V steps in V_b from 60 V to -100 V and at V_b = -130 V. The resistance peak in each curve corresponds to the charge neutrality point (CNP) at $D_b - D_t = 0$ for a given V_b. (f) The linear relation between top and bottom gate voltages that results in bilayer CNPs. (Figure and abridged caption from [84])

Although this dual-gated, bilayer device structure is more complex than a single-gated FET made from a graphene nanoribbon, it is a more flexible device with more potential optoelectronic applications, and may be able to achieve higher carrier mobility than graphene nanoribbons as well [73].

3.5 Optical properties of graphene

In addition to its exceptional electronic properties, graphene also has unusual optical properties. A single layer of graphene absorbs approximately $\pi\alpha \approx 2.3\%$ of incident light (where α is the fine structure constant) over the visible range [89]. This is attributed to the nearly-linear dispersion of graphene's electronic band structure, which results in a universal high-frequency conductivity of graphene, $G = e^2/4h$ that determines its optical reflectance and transmittance [90].

This is a high absorption coefficient for an atomically-thin monolayer, but it also means that graphene is a nearly-transparent, highly-conducting material. Here its high conductance even in the ungated state is a virtue rather than an obstacle (see Section 3.3.1). As such, graphene has the potential to replace indium tin oxide (ITO) in many applications. ITO, with a sheet resistance of 10-100 Ω/□ and a transparency of 80-85% at its optimal thickness [91],[92], is the best-known transparent conducting material and is now in very high demand due to the proliferation of liquid crystal displays (LCD). If large areas of graphene could be produced with consistent characteristics, it might prove a cost-effective substitute for ITO. Several published reports demonstrate large sheets of few-layer graphene with sheet resistance of 300-500 Ω/□ and transparency around 80%

[93],[94], and one pre-print claims sheet resistance of 40 Ω/□ and transparency around 90% [95].

Beyond its commercial applications, graphene's large absorption coefficient provides a means to identify very thin samples on certain surfaces via optical contrast with the substrate. I will discuss the benefits and pitfalls of this technique extensively in Chapter 4.

3.6 Raman spectroscopy of graphene

Raman spectroscopy is a very useful technique for the characterization of graphene and other graphitic materials. Among other strengths, it can be performed in ambient conditions, and can rapidly characterize small areas (under 1 μm^2).

3.6.1 Basics of Raman spectroscopy

As the name implies, Raman spectroscopy is based on the Raman effect of inelastic scattering of photons. For most materials, nearly all light is scattered elastically, however a small fraction of the incident light scatters inelastically. The scattered photon can have either a lower energy than the incident photon (Stokes Raman) or a higher energy (anti-Stokes Raman); of the two the Stokes Raman effect is stronger (significantly so for phonon energies well above $k_B T$).

In Stokes Raman scattering, not all of the energy of the incident photon goes into the scattered photon, but some of it instead excites other vibrational or rotational modes of the solid. As a result, the distribution of Raman shifts (changes in photon energy, typically expressed in terms of the change in wavenumber or spatial frequency, with units

of cm^{-1}) for a given material reveals information about the possible excitations of the system. A spectrometer is used to measure the intensity of scattered light for different Raman shifts, with some kind of notch filter required to suppress the much stronger signal from elastically scattered light (zero Raman shift).

3.6.2 Raman modes of graphene

To my knowledge, the first studies of the Raman properties of graphitic materials were reported by Tuinstra and Koenig in 1969 [96]. The authors measured the Raman spectra of pyrolitic graphite, commercial graphite, and activated carbon samples. In all these types of samples, they observed a prominent Raman peak at around 1575 cm^{-1}. The authors attribute this to the in-plane E_{2g} zero-momentum optical phonon mode [96], and nearly the same peak is observed in single-layer graphene due to the very weak effect of interlayer coupling [97].

Tuinstra and Koenig also observed a second Raman peak at around 1355 cm^{-1}, present weakly in commercial graphite and more strongly in activated carbon, but not at all in the high-purity pyrolitic graphite. In infinite crystals of graphene, only $k = 0$ (zero crystal momentum) phonon modes should be Raman active, because of the symmetry of the lattice. They thus attributed this peak, dubbed *D* (for disorder), to the presence of lattice defects, or finite-sized crystals which make certain high-symmetry zone-boundary phonon modes Raman active. Evidence from X-ray scattering backs this up, demonstrating a linear relationship between crystal size and the relative intensity of the *D* and *G* modes (I_D / I_G) [96].

A third prominent Raman mode has received a great deal of attention in recent graphene research: the *2D* mode (also called *G'*). Appearing at roughly twice the frequency of the *D* mode, the *2D* mode can in many cases be used to differentiate monolayer graphene from multilayers [97],[98]. The *2D* peak is due to a double-resonance process [99],[100], in which *two* phonons are scattered with opposite momenta, both close to k_K or $k_{K'}$ [97]. The exact energies available for this process are sensitive to the electronic band structure of graphene, which differs between one-, two-, and few-layer graphene. The *2D* mode of graphene is described in more detail in Section 5.2.

Ferrari et al. measured the Raman spectra of AB-stacked graphene of different layer thicknesses (identified via transmission electron microscopy) and found systematic differences in the *2D* band [97]. In particular, single-layer graphene has only a single, symmetric *2D* peak because there is only one pair of conduction and valence bands, while the *2D* mode of bilayer graphene has two pairs of valence and conduction bands (shown in Figure 3.6(d)), resulting in four possible combinations of initial and scattered electronic states. I have reproduced their spectra, highlighting the thickness-dependence and dispersion of the *2D* band, in Figure 3.7:

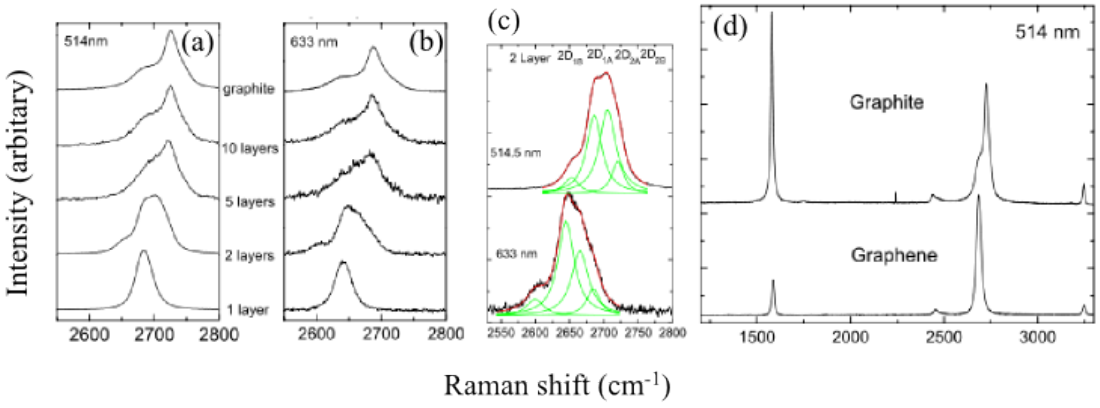

Figure 3.7: Raman spectra of different layer thicknesses of AB-stacked graphene. (a, b) 2D peaks of 1-, 2-, 5-, 10-layer graphene and bulk graphite under 514 nm and 633 nm lasers. (c) 2D peaks of bilayer graphene at 514 and 633 nm layers, showing the four sub-peaks. (d) Complete Raman spectra of monolayer graphene and many-layer AB-stacked graphite, showing the relative intensity of the G and 2D peaks. (From [97])

Although this work suggests that it should be possible to distinguish the thickness of any few-layer graphene sample using only the shape of its *2D* band, this has been found not to be the case. Because the changes in the *2D* modes of multilayer graphene are due to changes in the electronic band structure, other properties of the material can affect these as well. It has been found that few-layer graphene with misoriented or rotationally disordered layers exhibits a single-peaked Raman *2D* band that is very similar to that of monolayer graphene. This effect, which I discuss more extensively in Chapter 5, has been observed in mechanically exfoliated graphene [98],[101] (see Section 3.7.1), graphene grown epitaxially on SiC [102] (see Section 3.7.4), and by me on graphene grown via chemical vapor deposition on copper.

Furthermore, the results of Ferrari et al. in Figure 3.7 and other reports suggest that the relative intensity of the *G* and *2D* Raman peaks could be used to distinguish the thickness of graphene multilayers. However, this method is also unreliable because doping and interactions with the substrate can cause considerable sample-to-sample variation in this ratio [103],[104].

In Figure 3.8, I visually summarize the prominent *D*, *G*, and *2D* (or *G'*) Raman modes of graphene:

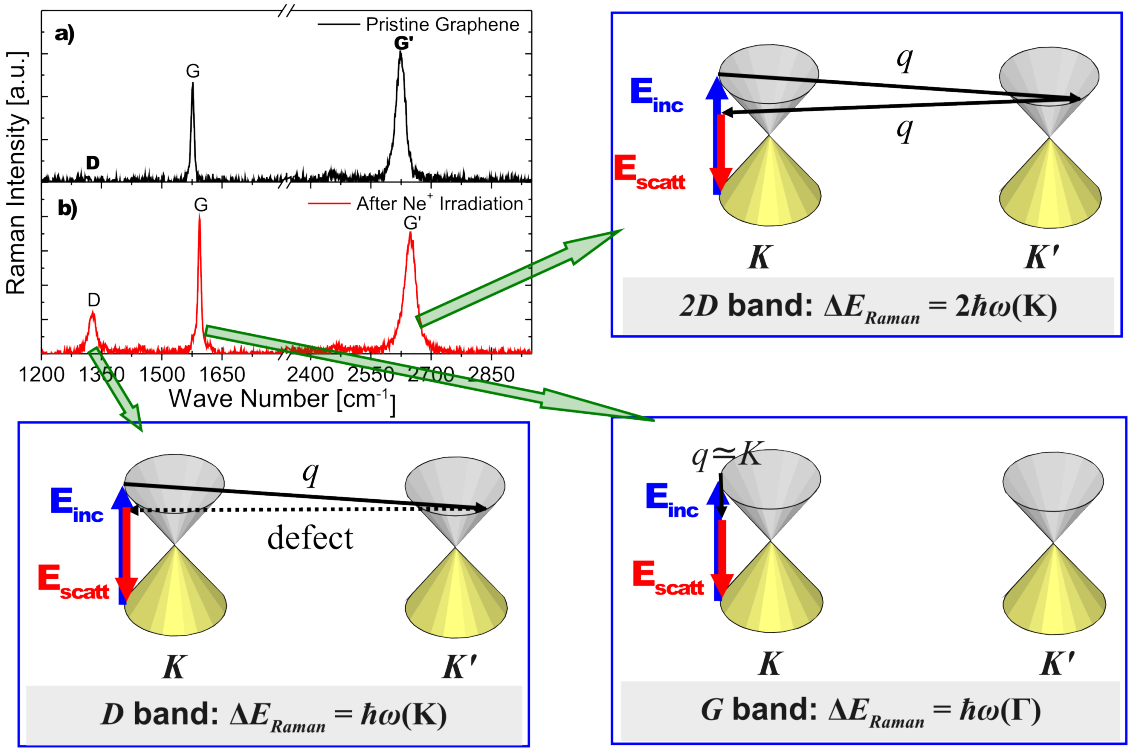

Figure 3.8: Raman D, G, and 2D (or G') modes of graphene. The Raman spectra in the upper-left show pristine and ion-irradiated (defected) monolayer graphene (from [72]). The D band is weak or nonexistent in pristine graphene but appears in defected or finite-size samples as discussed in the text. The other three diagrams show the low-energy electronic structure and phonon scattering involved in the 2D, G, and D Raman processes (clockwise from upper right).

3.7 Graphene synthesis methods

As I described above, graphene is an electron-hole symmetric semiconductor with a remarkably high experimentally achievable mobility (see Section 3.3.1), and it would in many ways be an ideal replacement for conventional silicon-based CMOS transistors if it

had a sufficient I_{on}/I_{off} ratio, which requires some way to introduce a band gap substantially greater than k_BT (such as the techniques described in Section 3.4).

Mass production of high-purity, low-defect sheets of graphene would also be required for its widespread commercial application. The earliest technique for fabricating graphene, mechanical exfoliation, has produced the highest-performing samples and is widely used in academic research, but does not scale to larger production. In this section, I will describe that technique, as well as several alternative synthesis methods which may be more promising for large-scale production. In particular, I will focus on chemical vapor deposition (CVD). In Chapters 4 and 5, I will discuss the optical and Raman characterization of graphene sheets which I have produced using CVD.

3.7.1 Mechanical exfoliation

The earliest graphene samples were produced by Andre Geim and colleagues at the University of Manchester, using the method of mechanical exfoliation of graphite, "a euphemism for slicing this strongly-layered material by gently rubbing it against another surface" [65]. This is also known as the drawing method, because it is the same process by which a graphite pencil draws a line on a sheet of paper. Graphite consists of many stacked layers of graphene. While the sp^2 bonds within each layer are extremely strong (cf. the enormous specific tensile strength of single-walled carbon nanotubes [105]), the interlayer coupling is by much weaker van der Waals interactions. Therefore, relatively intact sheets of graphene slide off, one or a few at a time, as the source material is dragged against another surface. Modern pencils are made from low-quality powdered graphite with clay added as a binder to hold it together, but the starting material for

obtaining graphene by exfoliation is typically highly-oriented pyrolitic graphite (HOPG) [68]; Kish graphite, which is a byproduct of an obsolete steel-making process; or geologic specimens of crystalline graphite.

While mechanical exfoliation can produce high-purity single-layer flakes of graphene, it has numerous drawbacks. It is a labor-intensive process and produces highly variable results, with products varying in thickness from single-layer graphene to flakes hundreds of layers thick. Yield is sensitive to the purity of the graphite source, and to the humidity of the environment in which it is performed. Usually, multilayer flakes retain the stacking order of the source material, but sometimes the layers are misoriented [101], a phenomenon which I have also observed in samples produced in my lab. Perhaps most importantly, the diameter of the flakes varies from around 100 nm to 1 mm [78], but usually does not exceed that in manual exfoliation. It is therefore impossible to envision a complex integrated circuit (IC) such as a microprocessor, let alone a large-area device such as a liquid crystal display backplane, made from mechanically-exfoliated graphene.

3.7.2 Unzipping carbon nanotubes

Hongjie Dai and colleagues have succeeded in "unzipping" carbon nanotubes (cutting them along their long axes) and unrolling them onto a flat substrate to make graphene nanoribbons [106]. They coat multi-walled nanotubes (MWNT) in a protective polymer such that half of their circular cross section is exposed while half is encased. Reactive ion etching is then used to etch the exposed portion, and the polymer is dissolved to leave graphene nanoribbons with consistent chirality along their edges. If the source nanotubes have uniform chirality, the nanoribbons should as well; there is a

one-to-one correspondence between the circumference of the nanotube and the width of the nanoribbon, and between their complementary chiral angles.

This technique is very exciting because nanoribbons can have a significant, non-zero band gap (as discussed in Section 3.4.1). However, it requires a source of carbon nanotubes with consistent chirality and does not solve the problem of how to pattern, etch, and selectively dope graphene over a large area, as is required for the manufacture of complex ICs.

3.7.3 Graphene nanoribbons from chemical precursors

Efforts to synthesis large-scale two-dimensional polymers have historically proven very difficult [107]. Recently, however, extremely narrow graphene nanoribbons have been produced from polycyclic aromatic hydrocarbon precursors, consisting of multiple six-atom carbon rings [108]. These molecules are patterned on substrates and then heated to remove the hydrogen-terminated edges, causing them to lie flat and bond together.

This technique is another route to creating narrow nanoribbons, and may offer greater ease of patterning the ribbons and choosing their chirality than the nanotube-unzipping method (Section 3.7.2).

3.7.4 Epitaxial growth on silicon carbide

Graphene has also been produced by epitaxial growth on crystalline wafers of silicon carbide (SiC), an insulating material with hexagonal lattice structures. At temperatures above 1100°C, the surface layers are reduced to graphene [109]. The results

depend on whether growth occurs on the carbon face $(000\bar{1})$ or on the silicon face (0001). The Si face typically produces few-layer (1-3) graphene with a consistent stacking order [110], while graphene on the C face is often 10-20 layers thick and rotationally disordered [111],[102]. Vacuum growth of epitaxial graphene on the Si-terminated (0001) face yields single-crystal domains with typical diameters of 30-100 nm, while on the C-terminated $(000\bar{1})$ face domain sizes are about 200 nm [109]. The thermal decomposition of SiC is not self-limiting, so a variety of different thicknesses of graphene can be formed by this process [112].

Emtsev et al. have found that growth in an argon atmosphere produces much higher-quality graphene samples [109]. In vacuum, Si atoms begin to evaporate from the surface at around 1150°C. In around 900 mbar of Ar, however, the Si atoms do not evaporate until about 1500°C (basically for the same reason that water boils at higher temperatures in higher-pressure atmospheres). With higher thermal energy, the SiC surface rearranges itself into smooth, parallel terraced steps of 300-700 nm in width, unlike the roughened substrate observed in lower-temperature vacuum growth [109]. The authors conclude that nucleation of graphene layers begins at these step edges and is limited only by the sizes of the steps, which at over 1 μm in width are much larger than the steps on the as-manufactured substrates. They provide evidence from Raman spectroscopy (see Section 3.6.2) to demonstrate low defect density of their epitaxial graphene, as shown in Figure 3.9(e).

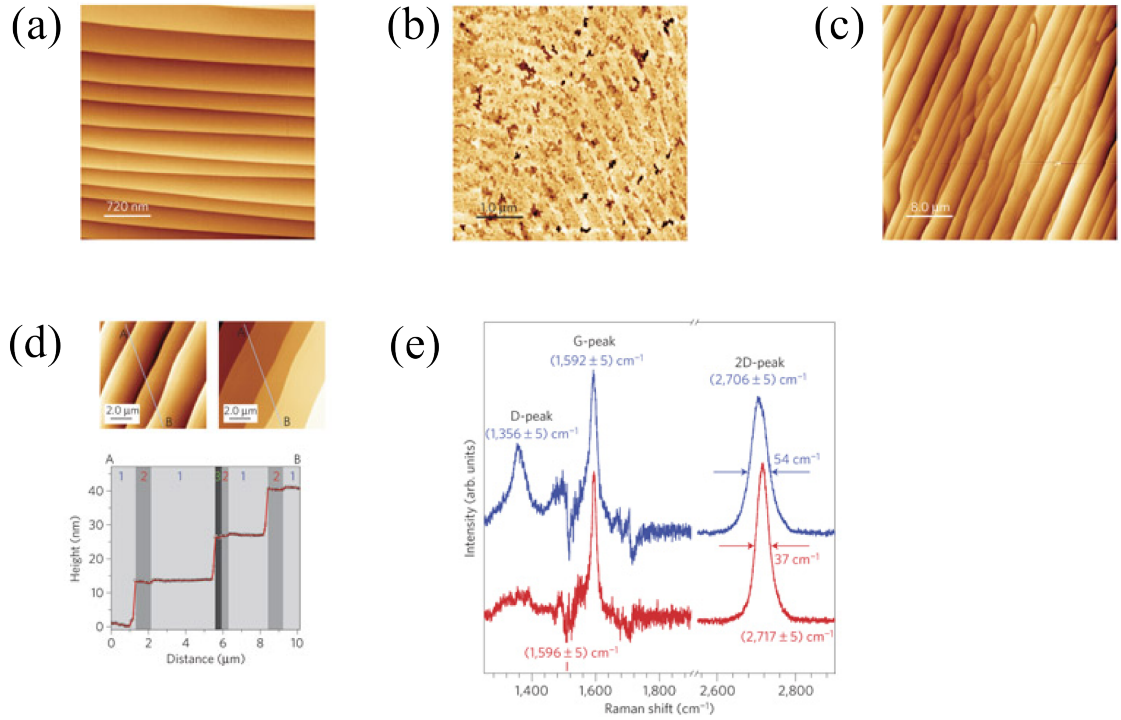

Figure 3.9: (a) Atomic force microscopy (AFM) image of hydrogen-terminated SiC (0001) surfaces, with a step height of 1.5 nm. (b) AFM image of graphene grown on this surface in UHV, showing small domain sizes. (c) AFM image of graphene grown on this surface in argon atmosphere, showing terraced domains similar to those of the underlying substrates, but of much greater width. (d) AFM profiles across steps show small thickness variations near the edges due to bilayer/trilayer formation. (e) Micro-Raman spectra of epitaxial graphene grown in UHV (blue upper curve) and in argon (red lower curve), the latter showing reduced D peak and therefore lower defect density. (From [109])

Epitaxial growth of graphene on SiC has the advantage of an insulating substrate, which means that graphene does not need to be transferred off in order to make useful

devices (a conducting substrate will obviously short-circuit graphene grown thereupon). Mobility of graphene grown on the Si face of SiC has been measured in some cases to be comparable to that of mechanically-exfoliated graphene on SiO_2 substrates, and the quantum Hall effect has also been observed in epitaxial graphene [113-115].

Because epitaxial graphene on SiC is produced on large, flat wafers, it is amenable to some of the conventional techniques of etching, UV photolithography, and metallization which the semiconductor industry has honed for use on silicon wafers. Recent reports have demonstrated graphene transistors on SiC, patterned to resemble Silicon *n*-channel MOSFETs, operating at GHz frequencies and with comparable performance [116]. In early 2010, researchers at IBM reported graphene transistors operating at frequencies of 100 GHz, produced by epitaxial growth on SiC wafers and patterned using relatively standard CMOS processing techniques [117].

3.8 Chemical vapor deposition of graphene

Although epitaxial growth of graphene on SiC has many advantages, it does require single-crystalline wafers costing at least $\$100/cm^2$ as of 2010, and the size of individual graphene domains is still limited by terraces on the substrates. Chemical vapor deposition (CVD) on transition metal substrates has emerged as an alternative technique for synthesis of large areas of graphene, and has been the focus of my own research. In CVD growth of graphene, a volatile carbon-containing gas flows over a metal substrate at high temperature (typically over 1000°C), and deposits carbon on it in the form of graphene.

Vapor synthesis of thin films of graphite on metals, and their oxides and carbides, has been studied for several decades (for a review, see Oshima and Nagashima [118]). Many of these early studies explored changes in the crystalline and lattice structure of metal-grown graphene, compared to the structure of bulk graphite. Chemical vapor deposition may also provide epitaxial growth, if there is a good match between the surface lattice of the substrate and that of the material being grown, in this case the 2D honeycomb structure of graphene. I will focus on recent techniques which seem promising for the growth of large sheets of graphene with transport and optical properties comparable to those of mechanically-exfoliated graphene.

Single-crystal transition metals with hexagonal structure seem a good candidate for CVD growth of epitaxial graphene. Ruthenium crystallizes in a hexagonal lattice with a lattice constant of 2.7 Å. Indeed, the controlled CVD growth of graphene and multilayers on the (0001) surface of crystalline ruthenium has been demonstrated [119], but unfortunately this technique also suffers from the high cost of single-crystal metals.

Surprisingly, non-hexagonal metals turn out to be more forgiving substrates for CVD growth of graphene. Nickel and copper have been widely adopted for this purpose, in part because their lattices are well-matched to that of graphene. Both form face-centered cubic (fcc) crystals; sliced along any of the eight equivalent {111} planes, an fcc lattice has a hexagonal surface structure. The lowest-energy surfaces of fcc metals are typically the {111} planes, and rolling these metals into foils often exposes their {111} surfaces [120],[121]. Nickel and copper have surfaces with lattice constants of 2.49 Å and 2.55 Å respectively; the lattice constant of each of graphene's two simple hexagonal

sub-lattices is approximately 4.92 Å (see Section 3.2). This gives a lattice mismatch of about 1% to nickel, and about 3% to copper.

3.8.1 Formation of graphene on nickel and copper

Chemical vapor deposition of graphene on polycrystalline sheets, foils, or thin films of nickel or copper can produce large areas of graphene (wafer-scale) at low cost [122]. Although both metals' surfaces are well-matched to the hexagonal lattice of graphene, the processes by which graphene forms on them seem to be very different.

A typical CVD growth recipe for graphene involves flowing methane, CH_4, (or sometimes ethylene C_2H_4) in an inert or reducing carrier gas over a nickel or copper substrate at a temperature above 1000°C. These metals catalyze the decomposition of CH_4, although copper is comparatively much less reactive [123],[124]. There are basically two different mechanisms by which this gas can deposit graphene on the metal surface. First, if carbon is soluble in the metal at the growth temperature, then it can dissolve into the bulk of the metal and precipitate or segregate out onto its surface, extruding a film of graphene as it is cooled and the solubility decreases. Second, carbon can adsorb on the metal surface, nucleating islands of graphene which expand to form islands as further carbon is added [125].

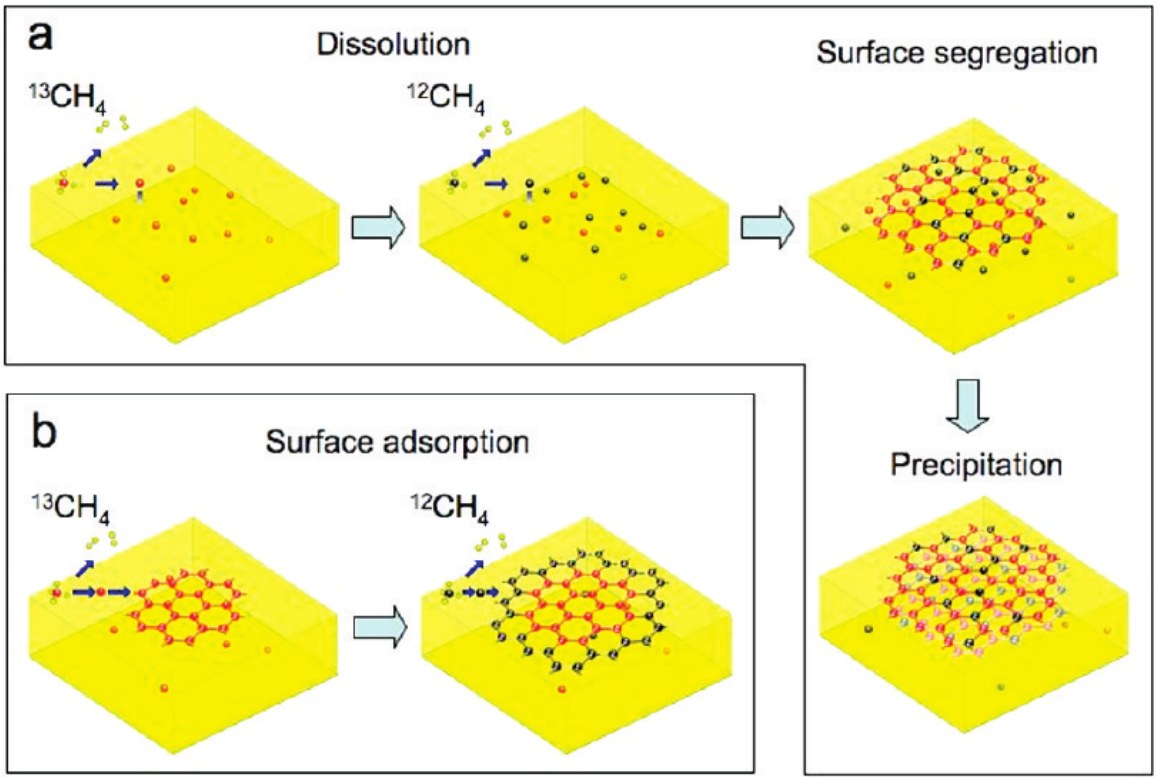

Figure 3.10: Schematic of the different mechanisms by which graphene can form on a metal surface, and the different distributions of carbon isotopes that would result from exposure to successive bursts of $^{13}CH_4$ and $^{12}CH_4$. (From [125])

Ruoff and colleagues at the University of Texas performed an isotope-labeling experiment to try to distinguish these forms of growth. They grew graphene on sputtered Ni films and Cu foils using low-pressure CVD (total pressure around 500 mTorr [126]), but used short, alternating bursts of high-purity ^{12}C- and ^{13}C-methane. They reasoned that the distribution of ^{12}C and ^{13}C on the surface would differ depending on the growth mechanism [125]:

(1) If growth is by dissolution followed by precipitation or segregation, the different isotopes of carbon should diffuse within the bulk of the metal and then precipitate out in a largely randomized mixture of ^{12}C and ^{13}C.

(2) If growth is by surface adsorption, with deposition of carbon being at highly-reactive nucleation sites and preceding outwards along the edges and surfaces of graphene islands, then the graphene films should be separated into regions of pure ^{12}C or ^{13}C.

(3) Some combination of these two mechanisms is also possible.

^{12}C-graphene and ^{13}C-graphene can be distinguished by their Raman spectra; the relative mass and concentration of each isotope affect the frequencies of the Raman modes (see Section 3.6) [127][45]. The Ruoff group found that after growth on Cu, the resultant graphene contained roughly circular regions with pure ^{13}C Raman peaks, corresponding to the initial 60 second burst of $^{13}CH_4$, which nucleated the initial graphene islands. Around these they found rings of graphene containing pure ^{12}C Raman peaks, corresponding to the following 60 second burst of $^{12}CH_4$, in which ^{12}C atoms attached to the existing islands but did not form new ones because the preferential nucleation sites had already been filled. I have reproduced their schematic of this distribution in Figure 3.10. They found only very small amount of mixed-isotope graphene at the boundaries between the pure regions [125]. They thus concluded that, because of the very low solubility of carbon in Cu, graphene growth on Cu proceeds almost exclusively by surface adsorption. Furthermore, they believe that it is a self-limiting process which can

produce only a single layer of graphene, since once a monolayer is deposited, there is no more Cu surface to catalyze the decomposition of methane.

In contrast, Ruoff's group found evidence from Raman spectroscopy that graphene forms on nickel through a combination of segregation and precipitation and surface adsorption [125]. This helps to explain some other experimental results from CVD growth of graphene on Ni. In particular, many researchers have found that CVD growth on Ni produces a mixture of single- and few-layer graphene [128-131],[94]. I observed the same phenomenon in my own attempts at atmospheric-pressure CVD growth of graphene on sputtered and evaporated films of Ni. Because segregation and precipitation of carbon are not self-limiting processes like surface segregation, it is likely that the multilayer regions result from the combination of the two processes.

Furthermore, it has been observed that CVD growth on Ni is highly sensitive to the rate at which the samples are cooled after growth [131], whereas growth on Cu is not sensitive to this [126]. This can also be explained in terms of surface segregation of carbon dissolved in the Ni substrate. One report compared CVD growth on Ni with cooling rates of 0.1°C/s, 10°C/s, and 20°C/s [131]. The authors found, again providing evidence from Raman spectroscopy, that the slowest cooling rate produced almost no graphene, the fastest produced thick and disordered graphene, while largely single-layer and defect-free graphene resulted from an intermediate cooling rate. They concluded that, under slow cooling, dissolved C diffuses into the bulk metal and remains in a solid solution. At faster cooling rates, C segregates on the Ni surface, but if this rate is too high the resultant film does not have time to relax into the equilibrium state of a

continuous graphene monolayer. Figure 3.11 illustrates their conclusions about the effect of cooling rate on CVD growth of graphene on Ni.

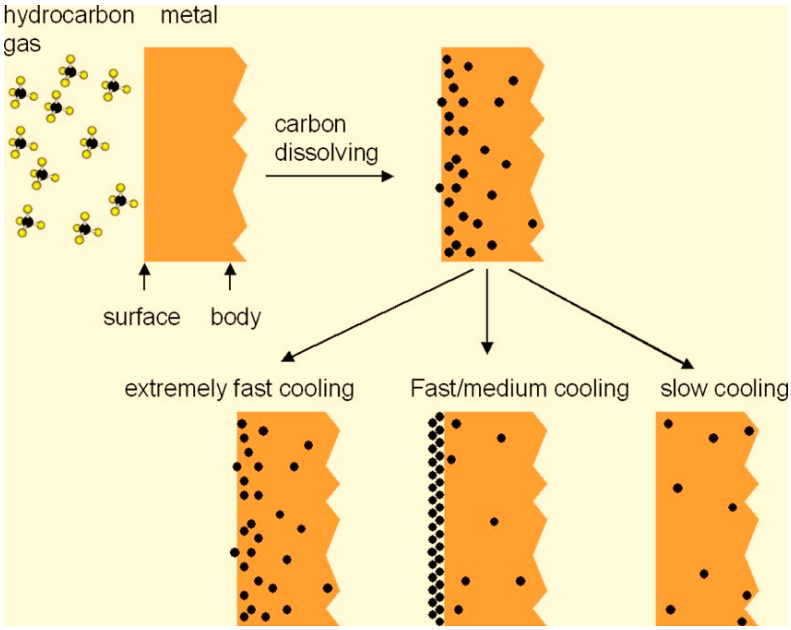

Figure 3.11: Schematic of carbon dissolving in Ni and segregating on the surface at different cooling rates. Extremely fast cooling is about 20°C/s, while fast/medium cooling is 5-10°C/s, and slow cooling is 0.1°C/s. (From [131])

3.9 My graphene CVD growth techniques

3.9.1 On thin films of nickel

Initially, I attempted atmospheric-pressure CVD growth of graphene on nickel. There are now several published reports of this technique [94],[122],[126],[128],[132].

I deposited thin films of nickel (200-300 nm) on SiO_2 wafers using dc sputtering and electron-beam evaporation. Using growth recipes derived from Kim et al. [94], and later Yu et al. [131], I was able to grow films of graphene on these surfaces, with sizes of

many mm^2 (limited only by the sizes of the substrates and the 1 inch diameter of the CVD furnace tube that I used). Figure 3.12 shows optical images of graphene that I grew on nickel thin films.

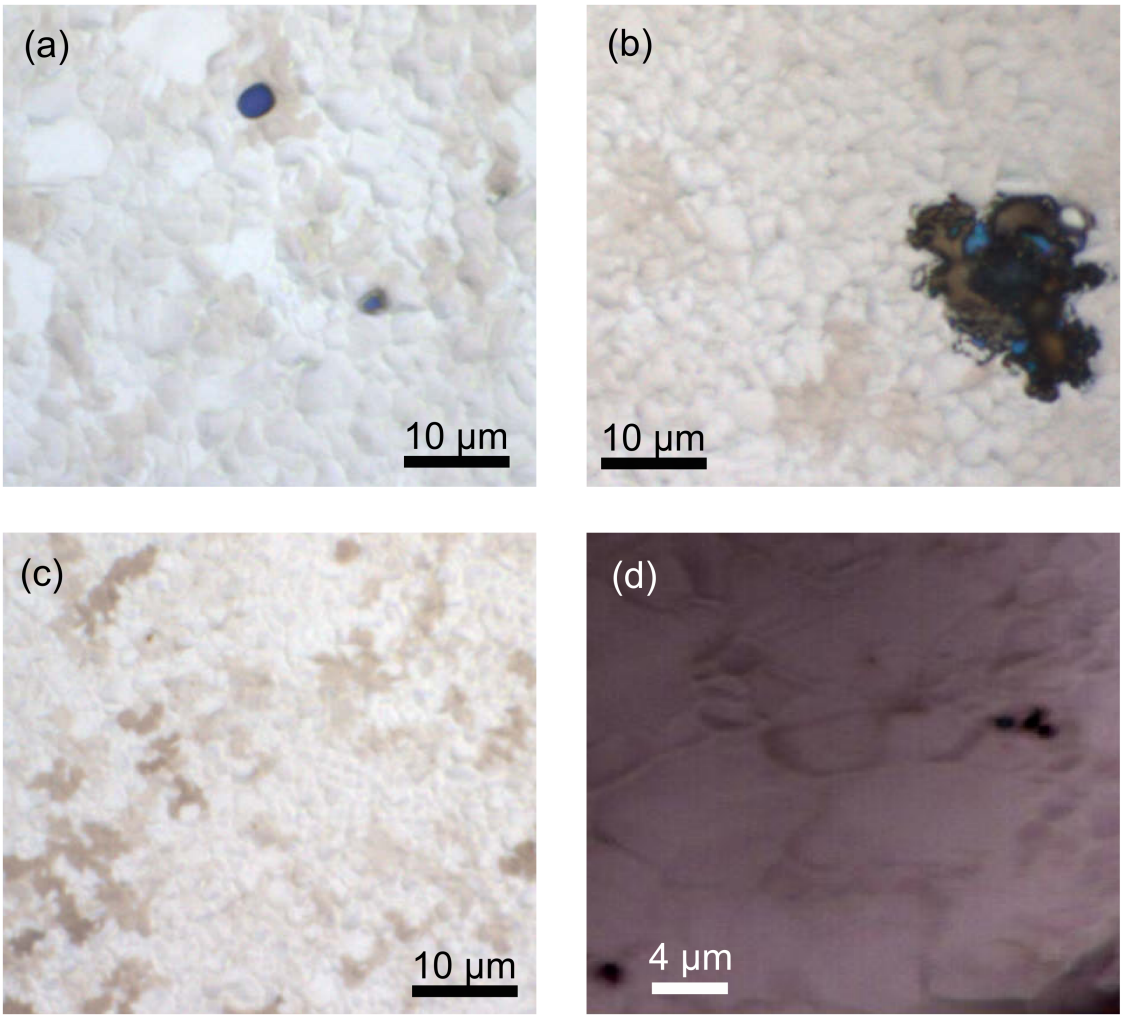

Figure 3.12: Optical images of graphene grown on sputtered nickel thin films (a,b,c) and electron-beam evaporated nickel thin films (d). All samples show variation in the optical contrast, and thus the thickness, of the graphene. (b) shows a large graphene-free void where the nickel seems to have dewetted from the SiO_2 substrate during the high-temperature CVD process, and (d) shows a concentration of graphene (darker material) around the edges of the nickel grains.

I also took Raman spectra of these graphene samples on nickel, and observed the characteristic *G* and *2D* peaks of mechanically-exfoliated graphene, along with *D* peaks

indicating varying levels of disorder (see Section 3.6.2 for the significance of these peaks). The relative intensity of these peaks often varied significantly, without any clearly-visible changes in the optical contrast of the graphene films, as shown in Figure 3.13:

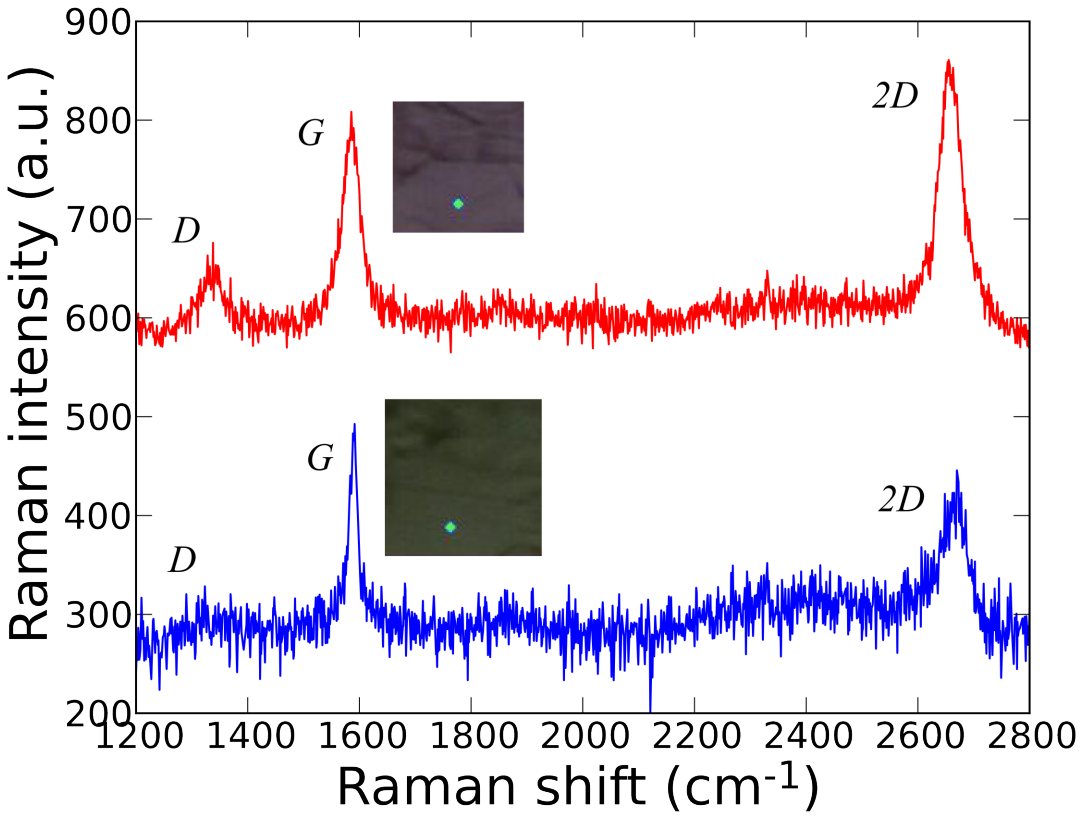

Figure 3.13: Raman spectra of graphene on e-beam evaporated nickel, at two nearby points on the same sample. The upper spectrum shows a $I_{2D}/I_G > 1$ *and a significant D peak (* $I_D/I_G \approx 0.25$ *), while the lower spectrum shows* $I_{2D}/I_G < 1$ *and a much smaller D peak. The asymmetrical shape of the 2D peak in the lower spectrum is suggestive of multilayer AB-stacked graphene (see Section 3.6.2), but it is difficult to be certain given the noise and Raman background. Insets show ~5×5 μm optical images around the points where the Raman spectra were measured.*

All of my attempts at growing graphene on nickel yielded samples with widely-varying optical contrast, attributed to variations in multilayer graphene thickness. Several subsequently-published reports have confirmed that CVD growth of graphene on nickel usually produces a mixture of different graphene thicknesses [133],[131],[132]. These results have now been explained by Yu et al. [131] and Li et al. [125] in terms of the processes of segregation and precipitation, which are not self-limiting, by which carbon-containing gas forms graphene on nickel. As I found it difficult to control the growth of graphene on nickel, and encountered other difficulties in transferring graphene from the nickel substrates, I switched to growing graphene on copper, which seemed to be a more promising technique in terms of producing consistent results.

3.9.2 On copper foils

There are now several published reports of low-pressure CVD growth of graphene on very large areas of copper [95],[122],[126]. Measurements by Raman spectroscopy, atomic force microscopy (AFM), electronic transport, and other techniques have led many researchers to conclude that graphene forms only a single monolayer on copper. As I mentioned above, the Ruoff group has shown convincingly that this is because growth on Cu at low pressure is exclusively by surface adsorption of carbon [125].

In my own experiments on graphene, I have instead adopted the technique of atmospheric-pressure CVD, initially due to the ready availability of an atmospheric-pressure furnace. This provides a much higher flux of carbon-containing gas, but is in other respects very similar to low-pressure CVD. I have adopted a growth procedure

similar to those of Lee et al. [122] and Cao et al. [134] to grow graphene on Cu; theirs are, to my knowledge, the only published reports of atmospheric-pressure growth on Cu.

For substrates, I use copper foils of 99.8% purity and 25 μm thickness (commercially sold by Alfa Aesar with part number 13382). Prior to growth, I sonicate 2-5 cm^2 pieces of foil in acetone, then rinse them in methanol followed by isopropanol, to clean them. I load the foils into a 1 inch quartz tube furnace and heat them in a linear ramp to approximately 1050°C under atmospheric pressure in flowing Ar at 1000 simple cubic centimeters per minute (SCCM) and H_2 at 50 SCCM. I hold the substrates at the growth temperature for 30 minutes to anneal them before applying the reaction gas mixture, which consists of CH_4 at 50 SCCM, H_2 at 15 SCCM, and Ar at 1000 SCCM. After growth, I cool the foils to room temperature, again in Ar at 1000 SCCM and H_2 at 50 SCCM.

I have found no systematic variation in the resulting graphene films over a range of growth times from 30-300 s, probably because the growth proceeds extremely quickly under such a high flux of methane (Ruoff's group found that a complete monolayer grows in under 3 min at 500 mTorr total pressure [125],[135]). I have also varied the cooling rate from <1 °C/s to >10 °C/s, and again find no variation, contrasting with reports of graphene grown on Ni via atmospheric-pressure CVD [131],[132], as I discussed in Section 3.8.1. I have, however, found substantial variation with growth temperature: samples grown at lower temperatures show much higher defects (evidenced by a broad *D* band similar to that of amorphous carbon [136]), with no graphene

produced at all below approximately 950°C. This pattern is corroborated by discussions that I have had with other researchers at recent conferences.

Following growth, I can analyze my graphene films immediately via Raman spectroscopy, or transfer them to insulating substrates for more detailed study. I have used a wet-transfer procedure substantially similar to that of Reina et al. [129]. I spin-coat a protective layer of poly[methyl methacrylate] (PMMA) to a thickness of approximately 200 nm on the copper foils, then dry them briefly on a hot plate at 150°C. I then immerse the foils in Transene APS-100 (a $FeCl_3$-based etchant) and heat it gently to accelerate the etching process. The copper is entirely etched within 30 min and the nearly transparent films of graphene and PMMA float to the surface. I rinse these films in DI water, then transfer by hand onto clean pieces of 300 nm thermally-grown SiO_2 on Si. Great care and dexterity is required to place the films onto the transfer substrates in a reasonably flat and unwrinkled configuration. I heat the substrates to around 60°C to slowly evaporate the water, dissolve the PMMA in acetone, and finally rinse gently in isopropanol. Using this technique, I successfully transferred films of graphene with areas exceeding 1 cm^2, again limited by the size of the substrates that I found convenient to work with.

It is difficult to obtain optical images of as-grown graphene on copper films, since the graphene does not contrast strongly with the surface, and the foils are not flat, making it very difficult to inspect them in a high-resolution microscope with a low depth of field. However, once transferred to SiO_2 substrates via the procedure I have just described, the

films of graphene are easily visible by optical contrast against the substrate (see Section 3.5 and Chapter 4).

Figure 3.14 shows optical images of two samples of CVD-grown graphene against nominal 300 nm SiO_2 substrates. While portions of each sample show relatively uniform optical contrast against the substrate, both samples also show noticeable bands of higher contrast, typically separated by 2-5 μm, which run parallel to each. These are reminiscent of the distribution of parallel grooves which are found on the copper substrates, apparently as a result of the polishing process used to produce the foils, and which persist after high-temperature annealing during the growth process. I will discuss the significance of these regions of higher contrast in much more detail in Chapter 4.

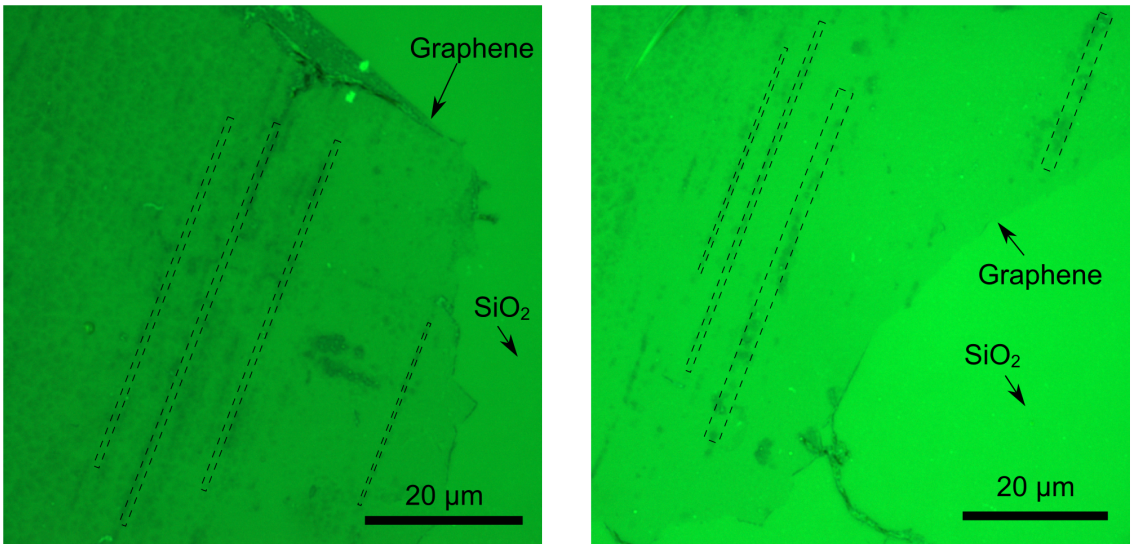

Figure 3.14: Optical images of two samples of graphene grown via atmospheric-pressure CVD on copper, under a 550 nm green filter. I intentionally introduced voids (areas of bare SiO_2) into these samples to show the contrast against the substrate. Notice the parallel bands of higher contrast (highlighted with dashed lines) which are visible in both of these samples.

After the transfer process, I am left with thin films of graphene on flat SiO_2 substrates, which are amenable to many measurement techniques, including atomic force microscopy, Raman spectroscopy, and optical contrast microscopy. In the following chapters I will describe the results of these measurements on my CVD-grown graphene films, and some unexpected conclusions about the distribution and thickness of this graphene.

4. Optical properties of graphene

4.1 History

The optical properties of graphene have attracted great interest since it was first isolated by the group of Andre Geim at the University of Manchester. All the earliest samples of graphene (and indeed, many of the highest-performing samples since) were fabricated via mechanical exfoliation of various pure forms of graphite [137].

The process of mechanical exfoliation of graphite (described in Section 3.7.1), is very capricious and produces a wide range of graphitic flakes, from monolayers to folded or tangled multilayers to thicker crystallites. Finding single-layer graphene among the various products of mechanical exfoliation required imaging techniques that could rapidly scan a large area of the transfer substrate and distinguish flakes by thickness.

While micro-Raman spectroscopy turned out to be very useful for this purpose [97], it is not a very fast technique, nor is it always straightforward to automate. Moreover, as I mentioned in Section 3.6.2 and will discuss further in Chapter 5, Raman spectroscopy can be "fooled" by its intimate dependence on the electronic and phonon structure of graphene.

Graphene researchers found that thin flakes of graphene contrasted strongly on silicon dioxide (SiO_2) substrates, for certain specific combinations of incident light color and oxide thickness. Figure 4.1 illustrates this effect, showing that wavelengths of light under which graphene contrasts strongly on 300 nm oxide render it nearly invisible on 200 nm oxide, and vice versa:

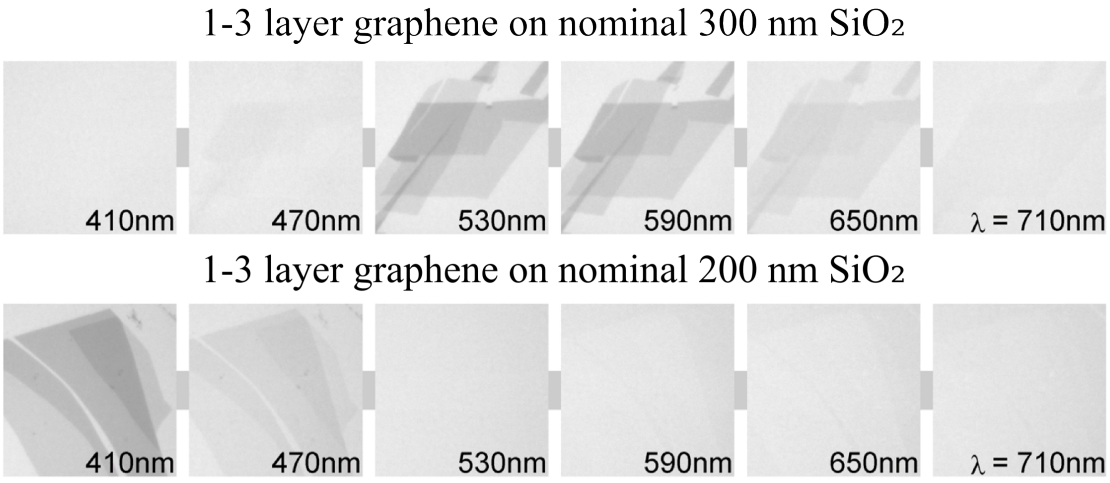

Figure 4.1: Optical contrast of thin graphene on 300 nm (top) and 200 nm (bottom) thick SiO_2 substrates, illuminated by light of various wavelengths indicated in the figure. (From [65])

This effect occurs because thin graphene is relatively transparent, and thus alters the optical path of reflected light via interference. Finding a distinctive contrast for single-layer graphene allows researchers to quickly locate small flakes of single-layer graphene among numerous samples of varying thickness simply using an optical microscope and visual identification [65].

4.2 Quantitative model

Although identification of monolayer and few-layer graphene via optical contrast seems an embarrassingly simple technique, understanding this phenomenon quantitatively can be fairly complex. In order to reliably determine the thickness of graphene using optical contrast, it is important to be able to accurately predict the contrast of one or several layers on a given substrate.

The basic model for graphene's optical contrast was summarized by Geim's group in Blake et al. [65]. One way to calculate the coefficient of reflection of their multilayer structure is to evaluate the infinite sums in the incoming, transmitted, and reflected wave amplitudes, which arise from the internal reflections in the intermediate layers, as shown in Figure 4.2. However, this quickly becomes unwieldy for a structure of more than 3 layers.

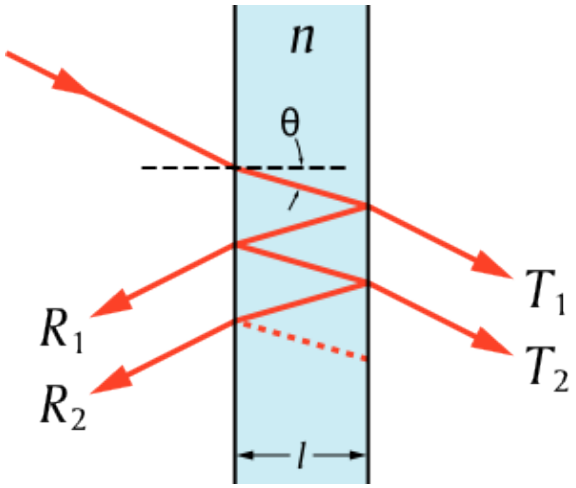

Figure 4.2: Repeated reflections and transmissions of light incident on a layered structure. (From Wikimedia Commons.)

4.2.1 Transfer-matrix method

Instead, one can use the transfer-matrix method to calculate the coefficients of reflection and transmission from a multilayer structure. Below I briefly derive this method, expanding on the lecture notes of Dr. Bo Sernelius of Linköping University in Sweden [138]. I have adopted the sign convention used by Blake et al. and by most subsequent graphene researchers, who use *negative* extinction coefficients for lossy

dielectric materials [65]; that is, the imaginary component of the index of refraction is negative.

Consider a beam of light shining from left to right through a structure consisting of *N* layers of variable thickness, as in Figure 4.3. It is assumed that the right-most layer has a semi-infinite thickness so that it contains no left-traveling wave.

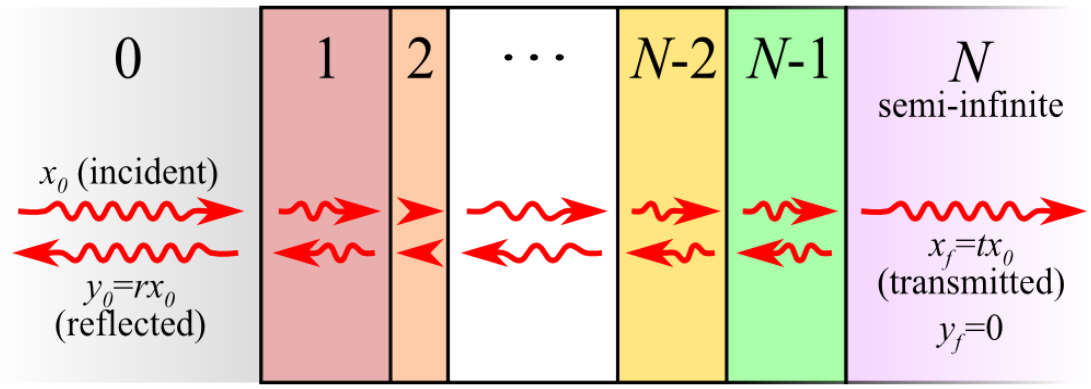

Figure 4.3: Structure of multiple transparent layers, with light shining through from left to right. Layer thickness and index of refraction are variable. Left- and right-most layers are semi-infinite.

In and adjacent to the *n*-th layer, there will be left-traveling and right-traveling waves. Let x'_L, y'_L be the complex amplitudes of the left- and right-going waves, respectively, just *outside* the left boundary of layer *n* and let x_L, y_L be the amplitudes of the left- and right-going waves just *inside* the left boundary of layer *n*, as shown in Figure 4.4:

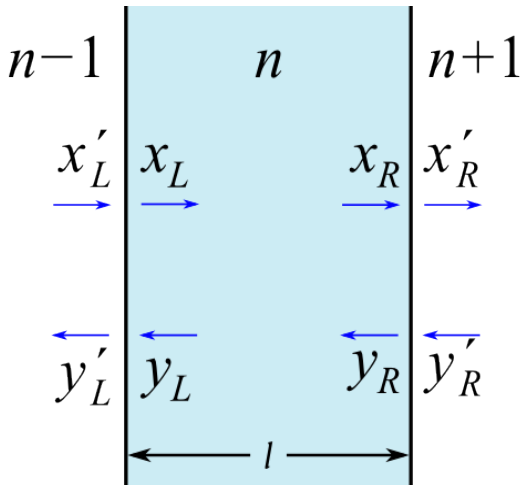

Figure 4.4: One layer in a many-layer structure. x'_L, y'_L *and* x_L, y_L *are the wave amplitudes just outside and inside its left boundary, respectively, while* x'_R, y'_R *and* x_R, y_R *are the amplitudes just outside and inside its right boundary, respectively.*

First, as light waves cross the interface from layer $n-1$ to layer *n*, they are transmitted and reflected at the interface. Let $r_{n-1,n}$ and $t_{n-1,n}$ be the amplitude Fresnel coefficients of reflection and transmission, respectively, from layer *n-1* to layer *n*. In the equilibrium case, the relationship between x'_L, y'_L and x_L, y_L can be read off of Figure 4.4,

$$\begin{aligned} x_L &= t_{n-1,n}\, x'_L + r_{n,n-1}\, y_L \\ y'_L &= t_{n,n-1}\, y_L + r_{n-1,n}\, x'_L \end{aligned} \tag{4.1}$$

This can be algebraically rearranged to,

$$\begin{aligned} x'_L &= \frac{1}{t_{n-1,n}}\, x_L - \frac{r_{n,n-1}}{t_{n-1,n}}\, y_L \\ y'_L &= t_{n,n-1}\, y_L + r_{n-1,n}\, x'_L \\ &= \frac{r_{n-1,n}}{t_{n-1,n}}\, x_L + \left(t_{n,n-1} - \frac{r_{n-1,n} r_{n,n-1}}{t_{n-1,n}} \right) y_L \end{aligned} \tag{4.2}$$

The following identities, which relate the opposite-direction Fresnel coefficients of reflection and transmission [139], are used to simplify Equations 4.2:

$$\begin{aligned} r_{n-1,n} &= -r_{n,n-1} \\ t_{n-1,n}t_{n,n-1} &= 1 + r_{n-1,n}r_{n,n-1} \end{aligned} \tag{4.3}$$

Substituting these into Equations 4.2, and rearranging it into the form of a matrix transformation:

$$\begin{pmatrix} x'_L \\ y'_L \end{pmatrix} = \frac{1}{t_{n-1,n}} \begin{pmatrix} 1 & r_{n-1,n} \\ r_{n-1,n} & 1 \end{pmatrix} \begin{pmatrix} x_L \\ y_L \end{pmatrix} \tag{4.4}$$

Secondly, as light waves of wavelength λ propagate a distance d in layer n, their phase and amplitude evolve by the phase factor $e^{-2\pi j\tilde{n}d/\lambda}$, where $\tilde{n}$ is the (possibly complex) index of refraction of the layer. Let $\Phi_n = 2\pi j l_n \tilde{n}$, where l_n is the thickness of layer n. In the case of normal incidence of light, the phase change across layer n is $e^{-\Phi_n}$. Now, again referring to Figure 4.4, the relationship between x_L, y_L and x_R, y_R is,

$$\begin{aligned} x_R &= e^{-\Phi_n}x_L \\ y_L &= e^{-\Phi_n}y_R \end{aligned} \quad \text{or} \quad \begin{pmatrix} x_L \\ y_L \end{pmatrix} = \begin{pmatrix} e^{\Phi_n} & 0 \\ 0 & e^{-\Phi_n} \end{pmatrix} \begin{pmatrix} x_R \\ y_R \end{pmatrix} \tag{4.5}$$

Combining Equations 4.4 and 4.5, gives the relationship between x'_L, y'_L and x_R, y_R:

$$\begin{aligned} \begin{pmatrix} x'_L \\ y'_L \end{pmatrix} &= \frac{1}{t_{n-1,n}} \begin{pmatrix} 1 & r_{n-1,n} \\ r_{n-1,n} & 1 \end{pmatrix} \begin{pmatrix} e^{\Phi_n} & 0 \\ 0 & e^{-\Phi_n} \end{pmatrix} \begin{pmatrix} x_R \\ y_R \end{pmatrix} \\ &= \frac{1}{t_{n-1,n}} \begin{pmatrix} e^{\Phi_n} & r_{n-1,n}e^{-\Phi_n} \\ r_{n-1,n}e^{\Phi_n} & e^{-\Phi_n} \end{pmatrix} \begin{pmatrix} x_R \\ y_R \end{pmatrix} \end{aligned} \tag{4.6}$$

The matrix appearing in Equation 4.6 is called the single-layer transfer matrix:

$$\boldsymbol{M_n} = \frac{e^{-j\Phi_n}}{t_{n-1,n}} \begin{pmatrix} e^{2j\Phi_n} & r_{n-1,n} \\ r_{n-1,n}e^{2j\Phi_n} & 1 \end{pmatrix} \tag{4.7}$$

$\boldsymbol{M}_n$ is used to calculate the wave amplitudes just *outside* the left interface of layer *n* from those just *inside* the right interface of layer *n*. Referring back to Figure 4.3, it is clear that the transfer matrix of the complete system is a product of transfer matrices, one for each individual layer. The relationship between the incident and reflected wave amplitudes just outside of layer 1, and those just outside the left interface of layer *N*, is given by:

$$\begin{pmatrix} x'_1 \\ y'_1 \end{pmatrix} = \left(\boldsymbol{M}_2 \times \boldsymbol{M}_3 \times \cdots \times \boldsymbol{M}_{N-1} \right) \begin{pmatrix} x'_N \\ y'_N \end{pmatrix} \tag{4.8}$$

In order to get the amplitudes just *inside* of layer *N*, it is necessary to account for the transfer matrix of the interface between layers *N*-1 and *N*. This is equivalent to an additional layer of zero width, and has the form of the matrix in Equation 4.4. The complete transfer matrix is thus,

$$\boldsymbol{M} = \boldsymbol{M}_1 \times \boldsymbol{M}_3 \times \cdots \times \boldsymbol{M}_{N-1} \times \frac{1}{t_{N-1,N}} \begin{pmatrix} 1 & r_{N-1,N} \\ r_{N-1,N} & 1 \end{pmatrix} \tag{4.9}$$

This complete transfer matrix connects the field amplitudes at the right edge of the left-most layer, and at the left edge of the right-most layer:

$$\begin{pmatrix} x_0 \\ y_0 \end{pmatrix} = \boldsymbol{M} \begin{pmatrix} x_N \\ y_N \end{pmatrix} \text{ where } \boldsymbol{M} = \begin{pmatrix} M_{11} & M_{12} \\ M_{21} & M_{22} \end{pmatrix} \tag{4.10}$$

Because the rightmost layer (*N*) is assumed to be semi-infinite, there is no reflected (left-going) wave in that layer, that is $y_f = 0$. Thus, $x_L = M_{11} x_R$ and $y_L = M_{21} x_R$. The amplitude transmission and reflection coefficients of the complete system are given by:

$$t = x_R / x_L = M_{11} \tag{4.11}$$

$$r = y_L / x_L = M_{21} / M_{11} \tag{4.12}$$

In summary, one can calculate the transmission and reflection coefficients of an arbitrarily complex structure of parallel, transparent, layered materials given the thicknesses and indices of refraction of each layer, and given the coefficients of reflection and transmission at each interface. These coefficients are given by the Fresnel equations, and in general depend on the polarization and angle of incidence of the light beam.

Based on the equations derived in this section (specifically 4.7, 4.9, and 4.12), I have written software in Python which can symbolically calculate the transfer matrices of arbitrarily complex layered structures. Using the *symbolic* formulas for the coefficients of transmission and reflection, this program then creates routines to perform efficient and precise *numerical* computation of the coefficients, given arrays representing the various input parameters. This software is very useful for analyzing and modeling complex layered structures including graphene.

4.3 Application to graphene

Blake et al. studied the optical properties of a three-layer structure consisting of graphene, SiO_2, and silicon; that is, light incident from air onto graphene on an oxidized silicon wafer, as shown in Figure 4.5:

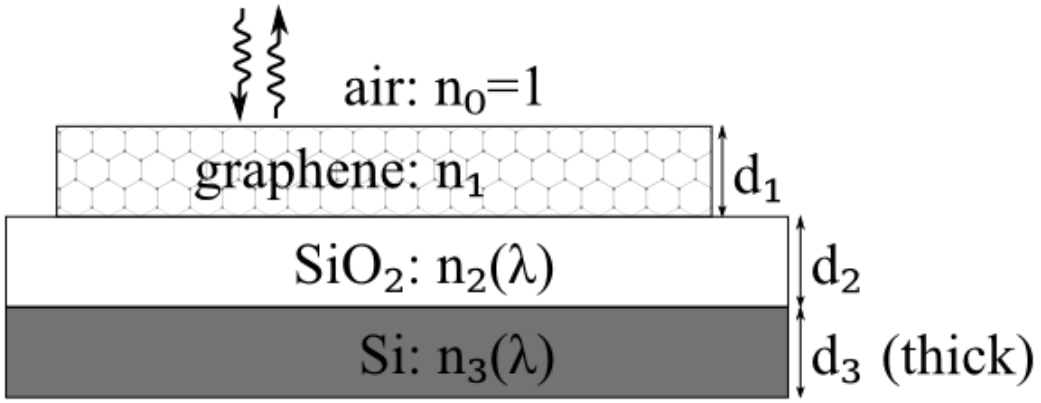

Figure 4.5: Three-layer structure used by Blake et al. [65] to model the optical contrast of graphene on oxidized silicon substrates.

The authors cite the intensity reflectance coefficient of this structure, which can be easily derived using the transfer-matrix method described in Section 4.2.1:

$$R=\left|\frac{r_{23}+r_{01}r_{12}r_{23}e^{2j\Phi_1}+r_{12}e^{2j\Phi_2}+r_{01}e^{2j(\Phi_1+\Phi_2)}}{r_{01}r_{23}+r_{12}r_{23}e^{2j\Phi_1}+r_{01}r_{12}e^{2j\Phi_2}+e^{2j(\Phi_1+\Phi_2)}}\right|^2 \tag{4.13}$$

For the case of normal incidence, the Fresnel reflection coefficients are simply $r_{ik}=(n_i-n_k)/(n_i+n_k)$, where n_i is the complex index of refraction of the *i*-th layer. The indices of refraction of single-crystal silicon and thermal oxide (fused silica) and their dispersions are well-known [140], and the authors assumed the index of refraction of graphene to be equal to that of bulk graphite, namely $n_G=2.6-1.3\,j$. The assumption of semi-infinite thickness for the silicon bottom layer is reasonable because silicon has a high extinction coefficient in the visible range, and because it is far thicker than the graphene or SiO_2 layers. The contrast of graphene on the substrate is defined as the relative difference in reflected light intensity between the bare substrate and the substrate with graphene on top [65]:

$$C=\frac{I_{\text{w/graphene}}-I_{\text{substrate}}}{I_{\text{substrate}}}=\frac{R(n_1=1)-R(n_1=n_G)}{R(n_1)=1} \tag{4.14}$$

Blake et al. found good qualitative agreement between the calculated contrast of single-layer graphene on 90-300 nm SiO_2 and the experimentally measured contrast, obtained using an optical microscope illuminated via narrow-band filters [65]. In particular, they accurately reproduced the wavelengths of peak contrast observed on 90 nm and 300 nm thickness of SiO_2, as shown in Figure 4.6 and Figure 4.7.

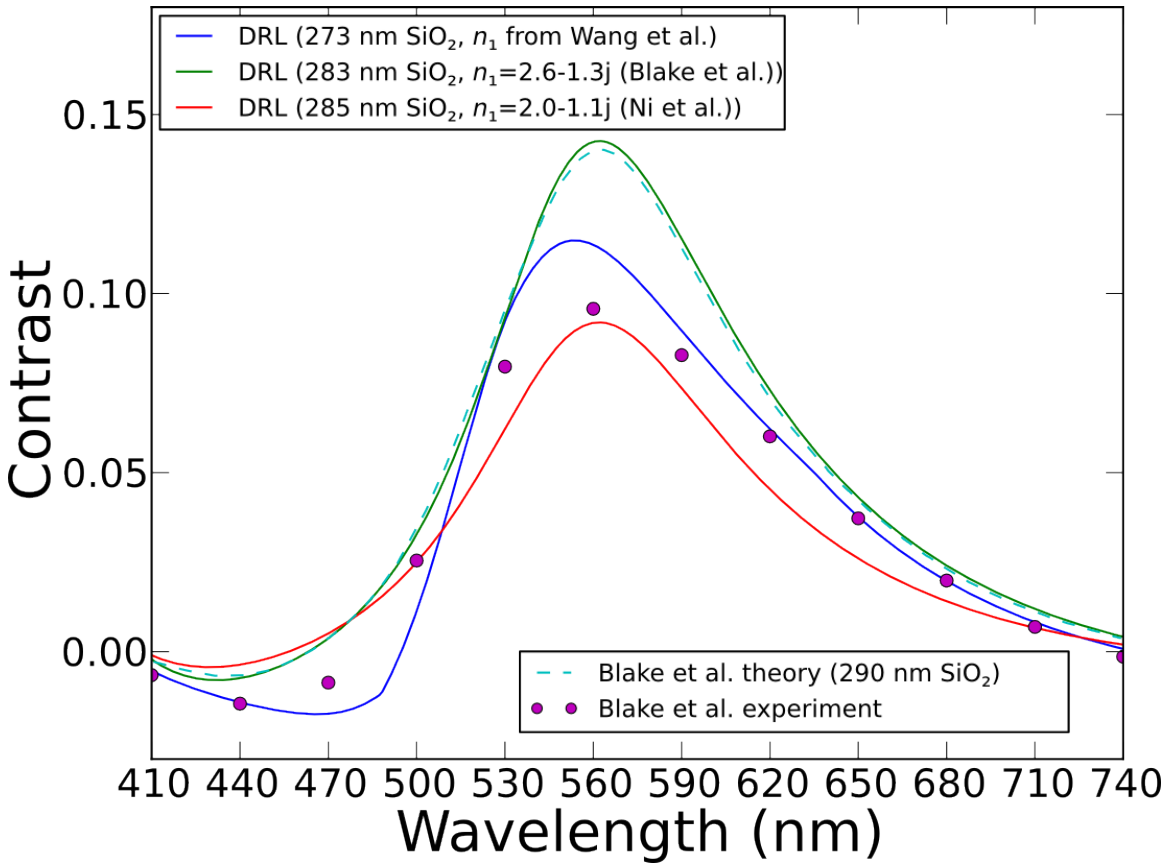

Figure 4.6: Contrast of single-layer graphene on nominal 300 nm SiO_2. Circles are measured contrast from Blake et al. [65],while the dashed line is the theoretical result by Blake et al. using 290 nm for the SiO_2 thickness. Solid lines are my theoretical results, using various indices of refraction for the graphene layers, and best-fit values for the SiO_2 thickness.

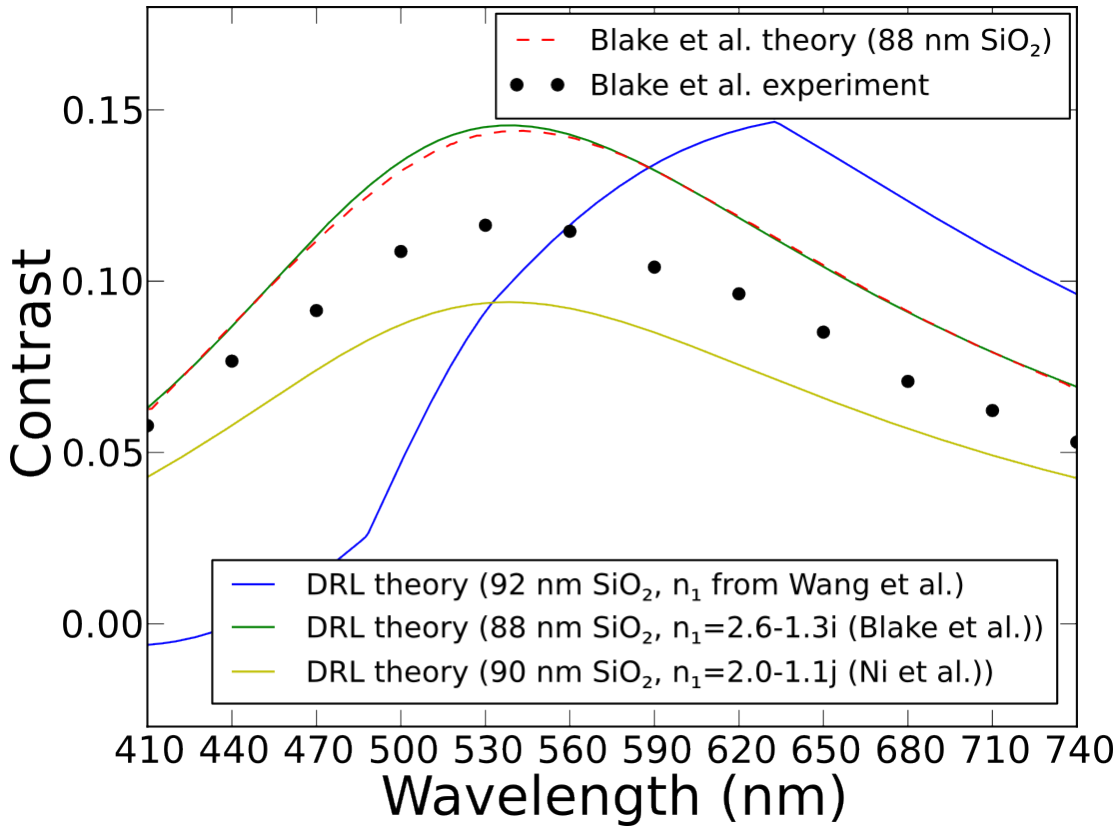

Figure 4.7: Contrast of single-layer graphene on nominal 90 nm SiO_2. Circles are measured contrast from Blake et al. [65],while the dashed line is the theoretical result by Blake et al. using 88 nm for the SiO_2 thickness. Solid lines are my theoretical results, using various indices of refraction for the graphene layers, and best-fit values for the SiO_2 thickness. Discontinuities in the curve using indices of refraction from Wang et al. [142] are due to limited data on their frequency dispersion.

4.4 Sources of error in optical contrast measurements

Although Blake et al. accurately predict the positions of graphene contrast peaks as functions of illumination wavelength, their model consistently overestimates the

magnitude of graphene's contrast [65]. They attribute this to a combination of the high numerical aperture of their microscope, NA=0.9, and imprecise knowledge of the exact index of refraction of graphene [65].

4.4.1 Non-normal incidence of light

A high numerical aperture lens collects light over a wide range of angles (roughly 128° for NA=0.9). Non-normal light incidence in turn alters the Fresnel reflection and transmission coefficients in a rather complicated polarization-dependent fashion, and increases the path length within each layer (Φ_n in Equation 4.5). Because optical contrast measurements typically use unpolarized light (equivalent to an equal mixture of *s*- and *p*-polarized light), because $R_p < R_s$ for lossless media (that is, *p*-polarized light reflects less than *s*-polarized), and because the SiO_2 layer is far thicker than the graphene, a crude approximation for the effect of non-normal incidence would be to increase the effective thickness of the SiO_2 in proportion to $1/\sin\theta$ and to discount the total reflectance by some empirical factor.

More recent work, however, has accounted for this source of error. Ni et al. measured the optical contrast of graphene on SiO_2, but took care to minimize non-normal incidence by collecting backscattered light via a pinhole aperture [141]. As I will discuss below, their work and other reports suggest that the largest source of error in the graphene contrast model of Blake et al. is an imprecise knowledge of the index of refraction of graphene.

4.4.2 Finite light source bandwidth

Rather than use bandpass filters to measure the contrast at each wavelength, as Blake et al. did, Ni et al. used white light and passed it through a spectrometer to find the contrast at each individual wavelength [141]. While it is not *a priori* obvious, this finite filter bandwidth is not a significant source of contrast in measured bandwidth. I theoretically investigated the effect of combining realistic filters with the wavelength-dependent reflectance of graphene. The contrast under a bandpass filter is defined by the following formula, where $C(\lambda)$ is the contrast under a monochromatic source of wavelength λ, and $T(\lambda)$ is the intensity transmittance of the filter at a specific wavelength:

$$C_{bp} = \frac{\int_0^\infty C(\lambda) T(\lambda) d\lambda}{\int_0^\infty T(\lambda) d\lambda} \tag{4.15}$$

I found that the effect of a filter with a 10 nm bandwidth is negligible, in terms of the fractional change in contrast of few-layer graphene on SiO_2 under a bandpass filter, compared to a monochromatic source. This relative change is defined as:

$$\Delta = \frac{C_{bp} - C(\lambda = \lambda_{center})}{C(\lambda = \lambda_{center})} \tag{4.16}$$

Figure 4.8 shows the very small fractional change in contrast given by Equation 4.16 for 1-9 layer graphene on SiO_2 substrates around 300 nm thickness, under a typical 600 nm filter:

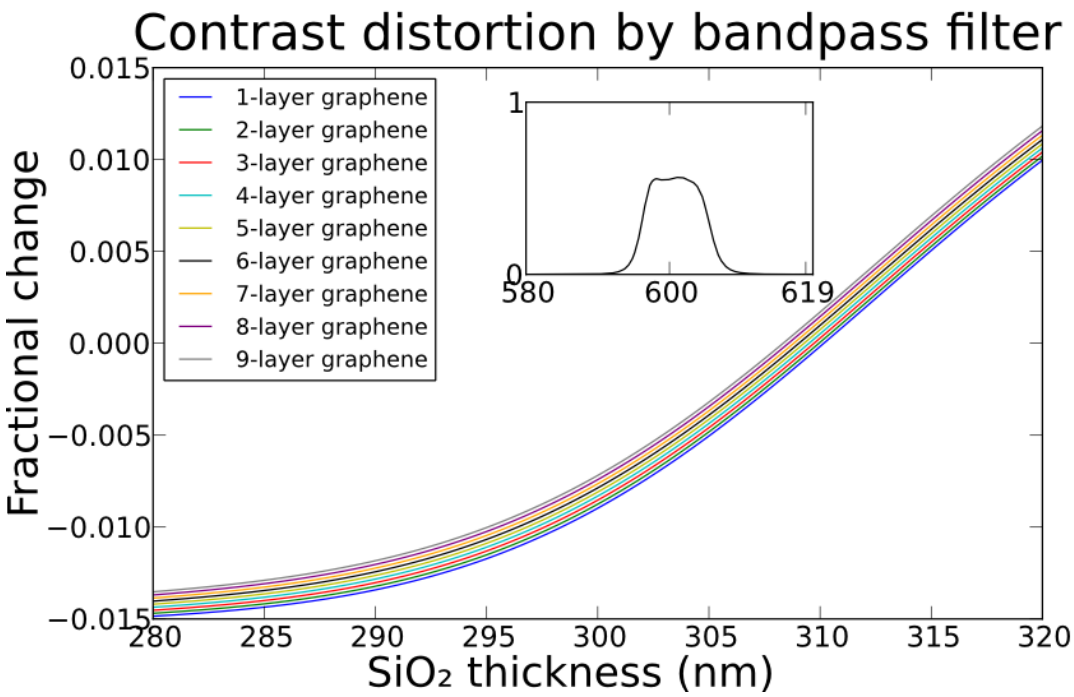

Figure 4.8: Theoretical contrast of graphene, and graphene multilayers, under white light passed through a Thorlabs FB600-10 bandpass filter (transmittance in inset), compared to contrast under a 600 nm monochromatic source. I used the refractive indices of Ni et al. [141] to produce this figure, but other reasonable values do not significantly affect the results.

4.4.3 Measuring the index of refraction of graphene

Ni et al. attempted to fit their measured contrast to the 3-layer reflectance formula of Equation 4.8 by varying the index of refraction of single-layer graphene, and thereby arrived at a best-fit value of $n = 2.0 - 1.1\,j$. Using this index gives somewhat better fits to the experimental data of Blake et al.; this can be seen in Figure 4.6 and Figure 4.7, where I have plotted the contrast predicted by Equation 4.8 using parameters from Blake

et al. *except* that I have substituted the estimate of graphene's index of refraction from Ni et al.

Subsequently, Wang et al. used spinning-disc picometrology to perform more direct measurements (i.e. without fitting to other data) of the index of refraction of mono- and bi-layer graphene [142]. Using this technique, they measured a strongly dispersive and thickness-dependent index of refraction for graphene, reproduced in Figure 4.9:

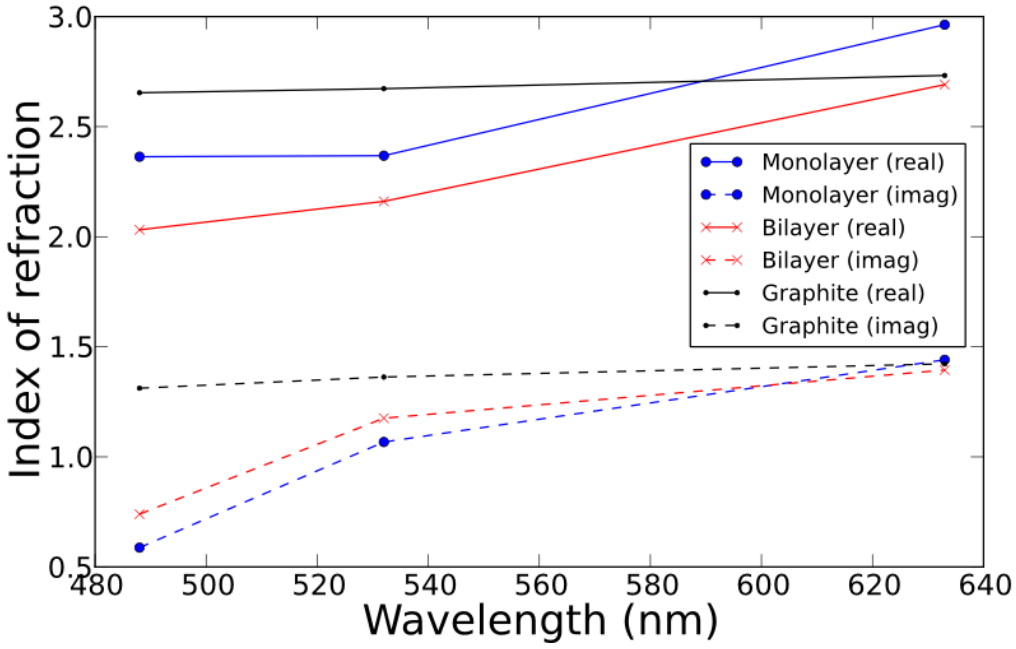

Figure 4.9: Refractive indices of monolayer graphene, bilayer graphene, and bulk graphite measured via spinning-disc picometrology by Wang et al. (Data from [142])

Wang et al. do not offer any explanation for the surprising dispersion or thickness-dependence of graphene's index of refraction, although Ni et al. had speculated that the optical differences between bulk graphite and graphene may be due to decreased interlayer interactions [141]. Unfortunately, it is difficult to reconcile the results of Wang et al—collected at only three laser wavelengths, 488 nm, 532 nm, and 633 nm—with

those collected by Blake et al. and Ni et al. over a broader and denser range. In Figure 4.6 and Figure 4.7, I also plot the contrast predicted by Equation 4.8 using parameters from Blake et al. but having substituted $n_1(\lambda)$ from the results of Wang et al., with real and imaginary components linearly interpolated between the wavelengths they measured. While Figure 4.6 shows that Wang's indices of refraction give a plausible fit to the contrast measured by Blake et al. on nominal 300 nm oxide, Figure 4.7 shows that Wang's values completely fail to account for the observed contrast on nominal 90 nm oxide.

The disagreements between the indices of refraction report by Ni et al., Wang et al., and others suggest substantial sample-to-sample variation in the optical properties of graphene. A recent review by Skulason et al. highlights the broad range of observed indices [143]. Skulason's theoretical work, based on the electronic band structure of graphene, indicates that the optical properties of few-layer graphene are dominated by absorption, and that they are thus more strongly dependent on its extinction coefficient rather than on $\mathrm{Re}\{n\}$ [143], consistent with the observations of Blake et al. [65].

These widely-observed and as-yet unexplained variations add great uncertainty to the use of optical contrast as a technique for identifying single-layer graphene, a result which many researchers seem not yet to have appreciated. However, optical contrast remains one of the fastest and easiest techniques available for characterizing graphene, and it is unclear whether any other single technique, such as Raman spectroscopy [101] or atomic-force microscopy [144], can offer greater precision.

4.5 Measuring the thickness of multilayer graphene

Graphene's optical contrast on a substrate such as SiO_2 depends on several factors, including the substrate thickness, the wavelength and angle of incidence of the light source, and, last but not least, on the imprecisely-known index of refraction of graphene and few-layer multilayers (discussed in Section 4.4).

4.5.1 Dependence on oxide thickness

Given the goal of using optical contrast to identify the thickness or layer count of graphene, it is desirable to minimize the uncertainties in these parameters. Blake et al. found good contrast (>10%) of single-layer graphene on *nominal* 300 nm SiO_2, under 550 nm green light, which has the advantage of reducing eye strain during manual, true-color searches for monolayer graphene flakes [65]. This combination of oxide thickness and illumination wavelength seems to have become very popular among other researchers. Ironically, it turns out to be a very poor choice, insofar as one hopes to reduce the likelihood of mis-identification of monolayer graphene based on uncertainties in the other parameters. Figure 4.10(a) illustrates this difficulty graphically:

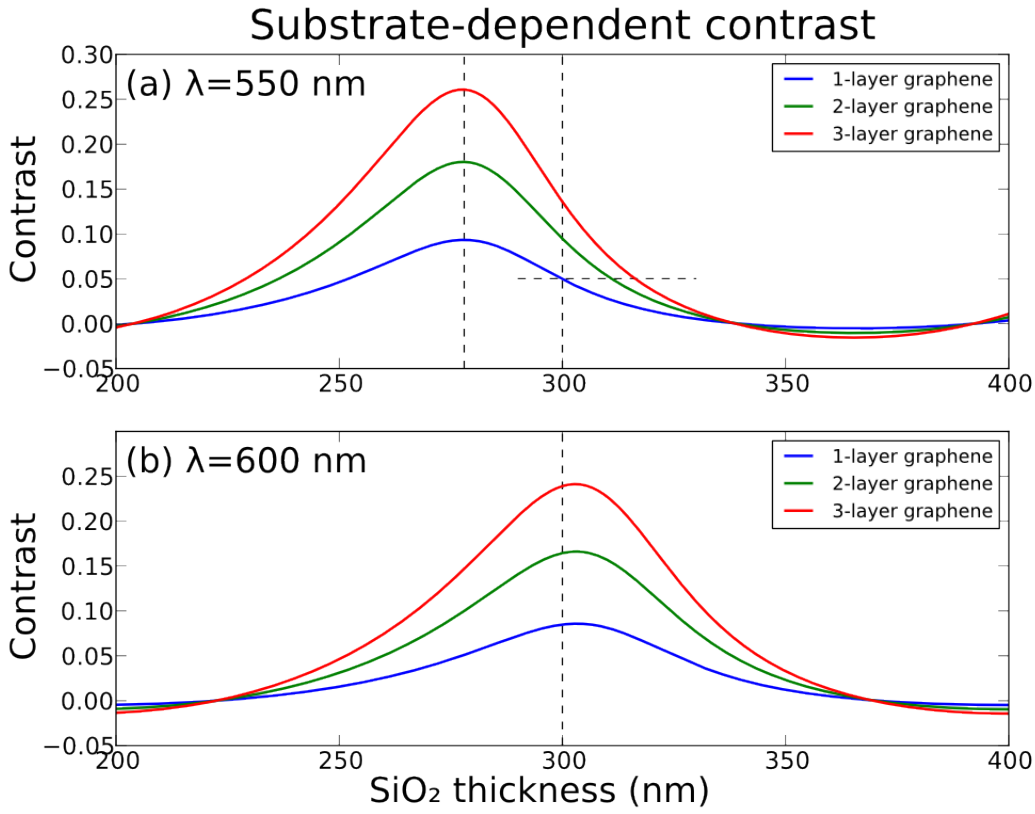

Figure 4.10: Theoretical contrast of 1-3 layer graphene on SiO_2 (using the 3-layer model and n_1=2.0-1.1j) under (a) 550 nm green light and (b) 600 nm orange light. Dashed lines at d_2=278 nm and d_2=300 nm highlight the substantial variation in the dependence of graphene's contrast on the oxide thickness.

On 300 nm SiO_2, under 550 nm light, the sensitivity of graphene's contrast to the oxide thickness (i.e. $|\partial C / \partial d_2|$ from Equations 4.8 and 4.1) is nearly maximized, so a comparatively small variation in the oxide thickness can produce a large variation in the contrast. Wafer vendors often specify tolerances of up to ±5% in oxide thickness. Figure 4.10(a) shows that, for example, the 5% contrast of monolayer graphene on 300 nm SiO_2

is identical to that of *bilayer* graphene on 311 nm SiO_2 (only 3.7% thicker). Without verification of wafer thickness, mono- and bi-layer graphene may not be reliably distinguished on nominal 300 nm SiO_2.

A better choice, if identification under 550 nm green light is desired, is to use 278 nm SiO_2. Since $|\partial C/\partial d_2|$ is minimized at this oxide thickness, unknown variations in the substrate are much less likely to result in mis-identification of single-layer graphene. For example, the 8.5% contrast of monolayer graphene on 278 nm SiO_2 shown in Figure 4.10(a) is equivalent to that of bilayer graphene on 301 nm SiO_2; an 8.3% uncertainty in the oxide thickness is necessary to confuse the two. Alternatively, 600 nm orange light can instead be used to more reliably identify graphene on 300 nm SiO_2, as shown in Figure 4.10(b); having prepared a large number of graphene samples on nominal 300 nm oxide before I began to investigate this effect systematically, I found the switch to a 600 nm filter to be the least painful option available to me.

4.5.2 Change in contrast due to additional graphene layers

As discussed in Section 4.4.3, the literature shows substantial sample-to-sample and lab-to-lab variation in the index of refraction of 1-few layer graphene. This makes it difficult to measure the precise number of layers of any particular sample using optical contrast alone, even if error due to other sources, such as uncertainty in the substrate's oxide thickness, are minimized.

However, in order to detect *changes* in graphene's thickness, such as islands of $N+1$ -layer graphene on *N*-layer graphene, it is only necessary to determine the possible range of contrast changes. Recall from Section 4.2.1 that the transfer matrix for an *N*-

layer structure is a product of $N-1$ matrices. Adding an additional layer on top, made of the same material as the previous top layer, means front-multiplying the transfer matrix by an additional single-layer matrix of the form in Equation 4.7:

$$\boldsymbol{M_1}=\frac{e^{-j\Phi_1}}{t_{01}}\begin{pmatrix} e^{2j\Phi_1} & r_{01} \\ r_{01}e^{2j\Phi_1} & 1 \end{pmatrix} \tag{4.17}$$

Also, the transfer matrix of the new second layer must be altered to account for the change in the reflection and transmission coefficients at its top surface (now zero and one respectively, since layers 1 and 2 are made of the same material). The new complete transfer matrix is,

$$\begin{aligned} \boldsymbol{M} &= \frac{e^{-j\Phi_1}}{t_{01}}\begin{pmatrix} e^{2j\Phi_1} & r_{01} \\ r_{01}e^{2j\Phi_1} & 1 \end{pmatrix}\cdot e^{-j\Phi_2}\begin{pmatrix} e^{2j\Phi_2} & 0 \\ 0 & 1 \end{pmatrix}\cdot \boldsymbol{M_3}\cdots\boldsymbol{M_N} \\ &= \frac{e^{-j(\Phi_1+\Phi_2)}}{t_{01}}\begin{pmatrix} e^{2j(\Phi_1+\Phi_2)} & r_{01} \\ r_{01}e^{2j(\Phi_1+\Phi_2)} & 1 \end{pmatrix}\cdot \boldsymbol{M_3}\cdots\boldsymbol{M_N} \end{aligned} \tag{4.18}$$

Now, $\boldsymbol{M_3}\cdots\boldsymbol{M_N}$ is the transfer matrix without the top two layers. In the case I am interested in, these two layers are both graphene, and everything below is the substrate. So $\boldsymbol{M_3}\cdots\boldsymbol{M_N}$ is the transfer matrix of the substrate; however, it is the transfer matrix of the substrate given light incident from *graphene*, rather than from *air* (my layer 0). It can, however, be rewritten in terms of light incident from air:

$$\begin{aligned} \boldsymbol{M_3}\cdots\boldsymbol{M_N} &= \frac{e^{-j\Phi_3}}{t_{23}}\begin{pmatrix} e^{2j\Phi_3} & 0 \\ 0 & 1 \end{pmatrix}\begin{pmatrix} 1 & r_{23} \\ r_{23} & 1 \end{pmatrix}\cdot \boldsymbol{M_4}\cdots\boldsymbol{M_N} \\ &= \begin{pmatrix} 1 & r_{23} \\ r_{23} & 1 \end{pmatrix}\begin{pmatrix} 1 & r_{03} \\ r_{03} & 1 \end{pmatrix}^{-1}\cdot\frac{e^{-j\Phi_3}}{t_{23}}\begin{pmatrix} e^{2j\Phi_3} & 0 \\ 0 & 1 \end{pmatrix}\begin{pmatrix} 1 & r_{23} \\ r_{23} & 1 \end{pmatrix}\cdot \boldsymbol{M_4}\cdots\boldsymbol{M_N} \\ &= \begin{pmatrix} 1 & r_{23} \\ r_{23} & 1 \end{pmatrix}\cdot\frac{1}{1-r_{03}^2}\begin{pmatrix} 1 & -r_{03} \\ -r_{03} & 1 \end{pmatrix}\cdot\tilde{\boldsymbol{M}} \\ &= \frac{1}{1-r_{03}^2}\begin{pmatrix} 1-r_{23}r_{03} & r_{23}-r_{03} \\ r_{23}-r_{03} & 1-r_{23}r_{03} \end{pmatrix}\cdot\tilde{\boldsymbol{M}} \end{aligned} \tag{4.19}$$

Now, $\tilde{\boldsymbol{M}}$ is the transfer matrix of light incident from air (layer 0) onto layers 3…*N*. Substituting Equation 4.15 into Equation 4.14,

$$\begin{aligned}\boldsymbol{M} &= \frac{e^{-j(\Phi_1+\Phi_2)}}{t_{01}}\begin{pmatrix} e^{2j(\Phi_1+\Phi_2)} & r_{01} \\ r_{01}e^{2j(\Phi_1+\Phi_2)} & 1 \end{pmatrix}\cdot\frac{1}{1-r_{03}^{\,2}}\begin{pmatrix} 1-r_{23}r_{03} & r_{23}-r_{03} \\ r_{23}-r_{03} & 1-r_{23}r_{03} \end{pmatrix}\cdot\tilde{\boldsymbol{M}} \\ &= \begin{pmatrix} e^{2j(\Phi_1+\Phi_2)}(1-r_{23}r_{03})-r_{01}(r_{23}-r_{03}) & e^{2j(\Phi_1+\Phi_2)}(r_{23}-r_{03})-r_{01}(1-r_{23}r_{03}) \\ r_{01}e^{2j(\Phi_1+\Phi_2)}(1-r_{23}r_{03})-(r_{23}-r_{03}) & r_{01}e^{2j(\Phi_1+\Phi_2)}(r_{23}-r_{03})-(1-r_{23}r_{03}) \end{pmatrix} \\ &\quad\cdot A\,\tilde{\boldsymbol{M}}\end{aligned} \tag{4.20}$$

Here *A* is a constant prefactor which is not needed to determine the reflectance, since it cancels out, but does figure in the transmittance (see Equations 4.11 and 4.12). Expanding $\boldsymbol{M}$ from Equation 4.13 into individual matrix elements,

$$\begin{aligned} M_{11} &= A[e^{2j(\Phi_1+\Phi_2)}(1-r_{23}r_{03})-r_{01}(r_{23}-r_{03})]\tilde{M}_{11} \\ &\quad + A[e^{2j(\Phi_1+\Phi_2)}(r_{23}-r_{03})-r_{01}(1-r_{23}r_{03})]\tilde{M}_{21} \\ M_{21} &= A[r_{01}e^{2j(\Phi_1+\Phi_2)}(1-r_{23}r_{03})-(r_{23}-r_{03})]\tilde{M}_{11} \\ &\quad + A[r_{01}e^{2j(\Phi_1+\Phi_2)}(r_{23}-r_{03})-(1-r_{23}r_{03})]\tilde{M}_{21} \end{aligned} \tag{4.21}$$

From Equation 4.11, the amplitude reflection coefficient for the complete structure is,

$$\begin{aligned} r &= M_{21}/M_{11} \\ &= \frac{r_{01}e^{2j(\Phi_1+\Phi_2)}(1-r_{23}r_{03})-(r_{23}-r_{03})+[r_{01}e^{2j(\Phi_1+\Phi_2)}(r_{23}-r_{03})-(1-r_{23}r_{03})]\tilde{r}}{e^{2j(\Phi_1+\Phi_2)}(1-r_{23}r_{03})-r_{01}(r_{23}-r_{03})+[e^{2j(\Phi_1+\Phi_2)}(r_{23}-r_{03})-r_{01}(1-r_{23}r_{03})]\tilde{r}} \end{aligned} \tag{4.22}$$

Here $\tilde{r}=\tilde{M}_{21}/\tilde{M}_{11}$ is the amplitude reflection coefficient of light incident from air (layer 0) onto layers 3…*N*. While the expression for *r* in Equation 4.10 is lengthy and awkward, it clearly demonstrates that the uncertainty in the reflectance of graphene on an SiO_2 substrate can be ascribed to just three independently varying quantities:

(1) The thickness of the oxide substrate ($\tilde{r}$ is a known function of this)

(2) The index of refraction n_g of the graphene (r_{01} is a known function of this)

(3) The thickness of the graphene ($\Phi_1+\Phi_2$ is a known function of this and n_g)

There is uncertainty in all three of these: the effect of oxide thickness was discussed in Section 4.5.1, while the index of refraction measured for graphene shows considerable variation (see Section 4.4.3), and the thickness of the graphene should be treated as an unknown quantity, since it is what I seek to measure.

Given experimental uncertainty in each of these three parameters, one might assume that optical contrast cannot give any reliable information at all about variations in graphene layer number. Fortunately, this is not the case. In order to demonstrate this, I have calculated the differential contrast of graphene (that is, the change in contrast due to adding one additional layer) under 600 nm light, allowing all three parameters to vary:

(1) SiO_2 thickness varies from 290 to 310 nm (equivalent to a nominal 300 nm wafer with ±3.3% uncertainty).

(2) Graphene's index of refraction, n_g, varies over the Cartesian product of $\mathrm{Re}\{n_g\} \in [2.0, 3.0]$ and $\mathrm{Im}\{n_g\} \in [-0.8, -1.6]$. This is essentially the entire range of reported experimental and theoretical values reported for 1…few-layer graphene in the review by Skulason et al. [143].

(3) Graphene thickness varies from 0 to 10 layers.

In Figure 4.11, I summarize the possible variations in graphene's differential contrast over this 3-dimensional phase space:

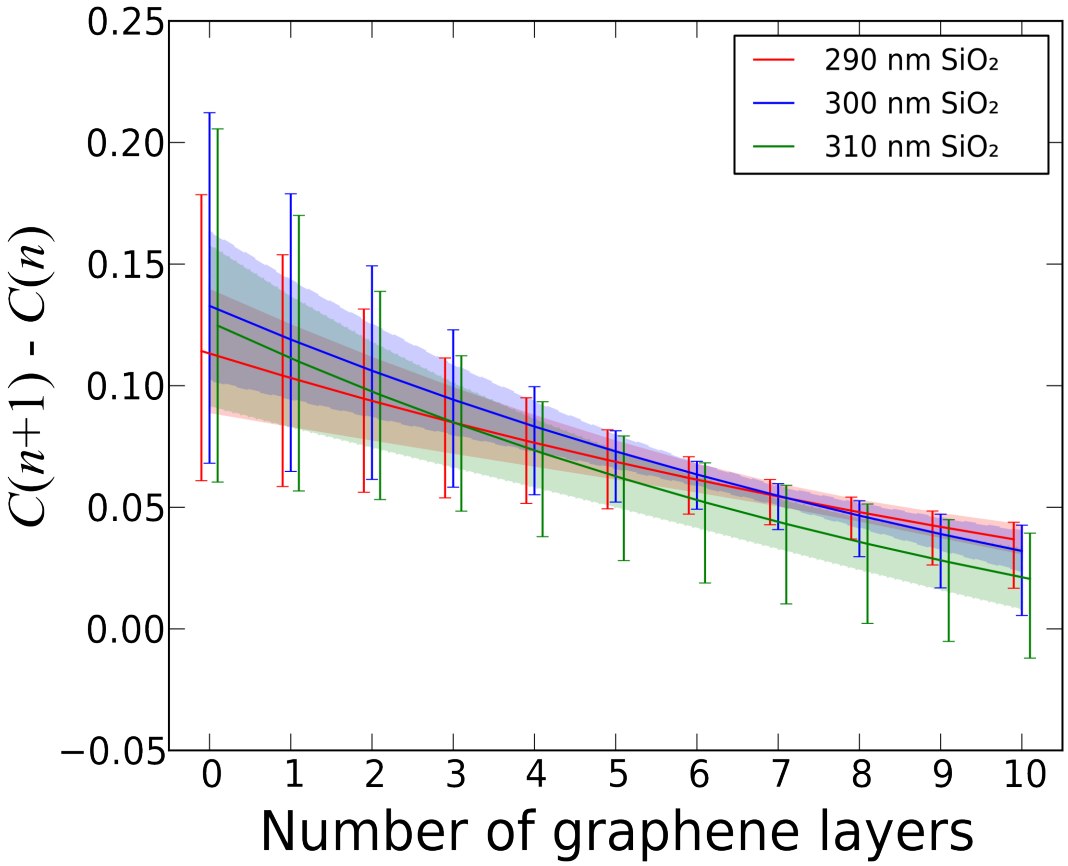

Figure 4.11: Absolute change in contrast from adding one additional monolayer of graphene, on 290, 300, and 310 nm SiO_2 under 600 nm illumination. The index of refraction of graphene, n_g, varies over the phase space discussed in the text. For a given number of layers, the error bar indicates the entire range of differential contrast, while the central bands show one standard deviation around the mean differential contrast for each combination of layer number and oxide thickness ($\overline{\Delta C} \pm \sigma_{\Delta C}$).

It is clear from Figure 4.11 that, under these conditions, the change in contrast from adding an additional layer of graphene is almost certainly positive, for 1 to 10 layers of graphene. For 1 to 7 layers, the change is almost certainly 0.05, which should be

easily detectable by eye. In producing Figure 4.11, I used a uniform distribution for graphene's index of refraction. If the indices of refraction of real graphene samples show some stronger central tendency, this account would narrow the $\pm\sigma$ band in the figure.

Thus, despite considerable uncertainty about the index of refraction of graphene and of SiO_2 substrate thickness, a judicious choice of filters enables the use of optical contrast to map variations in graphene thickness.

4.6 Measuring the optical contrast of CVD-grown graphene

Armed with a theoretical model of graphene's contrast on SiO_2 and an awareness of the many sources of uncertainty in this model, as described in Sections 4.2-4.5, I am now ready to present experimental data on its optical contrast.

In Section 3.9, I described the atmospheric-pressure chemical vapor deposition (CVD) method by which I have grown graphene films on copper foils, and then transferred them to SiO_2 substrates via a chemical etching process.

Researchers who have grown graphene via low-pressure CVD on copper substrates have found this process to produce single-layer graphene almost exclusively [93],[95],[126],[122],[125], providing evidence of uniform optical contrast, uniform Raman characteristics, and transport data consistent with monolayer graphene. My CVD-grown graphene samples show significant non-uniformity of their optical contrast. Some, but not all, of the regions of increased contrast lie in parallel bands which resemble the parallel polishing marks on the copper substrates, as I mentioned previously. Figure 4.12 again shows the patterns of optical contrast on two samples of CVD-grown graphene transferred to nominal 300 nm SiO_2.

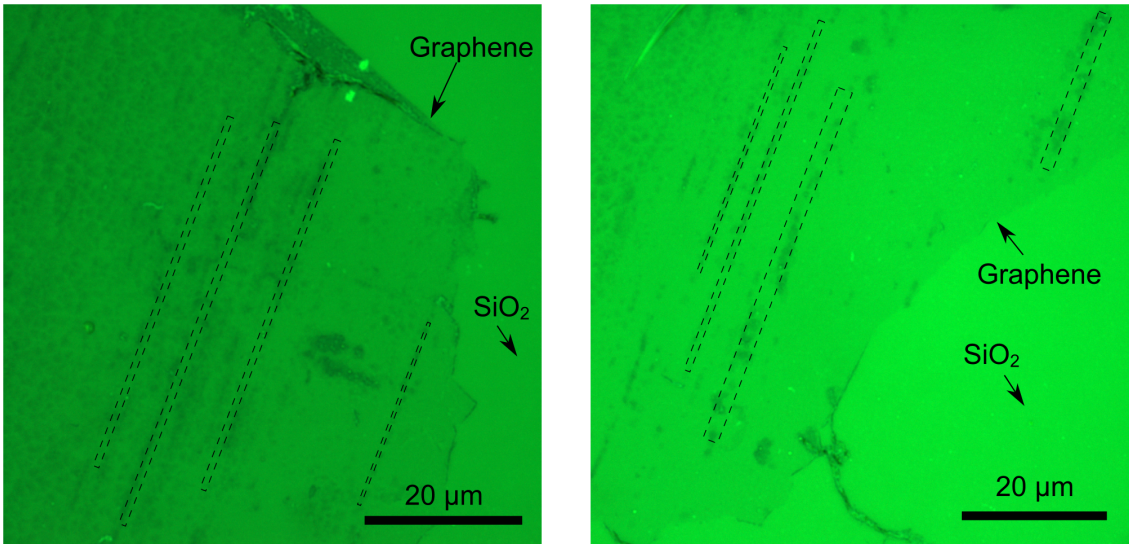

Figure 4.12: Optical images of two samples of graphene grown via atmospheric-pressure CVD on copper, under a 550 nm green filter. I intentionally introduced voids (areas of bare SiO_2) into these samples to show the contrast against the substrate. Notice the parallel bands of higher contrast (highlighted with dashed lines) which are visible in both of these samples.

4.6.1 Image acquisition

I took optical images of my CVD-grown graphene using an Olympus STM6 measuring microscope fitted with a 100× objective with a numerical aperture of 0.9. I captured high-resolution, color images in TIFF format using a digital camera. I took care care to ensure as little post-processing of the images as possible. In particular, I avoided the use of the nonlinear gamma correction which is often applied by image processing software to adjust for the non-linear response of typical computer displays, disabled automatic white balance and color correction, and tried as hard as possible to maintain constant illumination levels.

I did, however, calibrate the camera to correct for non-linear illumination of its field of view. This effect, known as vignetting, is visible in many photographs (particularly from cameras with inexpensive lenses at maximum apertures), where the edges appear less bright than the central portion of the image. Vignetting is well-known to optics engineers [145], and although there are many sources, in our microscope it is likely caused by the combined effects of variable aperture size in multi-element objective lenses, and the angle-dependent sensitivity of digital camera sensors. All the images which I present below have been corrected to account for vignetting.

Initially, I used a 550 nm green filter to capture high-contrast images of graphene on SiO_2, following the lead of Blake et al. [65] and many other graphene researchers. However, as I discussed in Section 4.5.1, theoretical models show that a 600 nm filter is much less sensitive to slight variations of oxide thickness around 300 nm. I therefore switched to a Thorlabs FB600-10 filter centered at 600 nm, with an approximate full-width half-maximum bandwidth of 10 nm. As I discussed in Section 4.4.2, the finite bandwidth of such filters does not significantly affect the results of optical contrast measurements.

4.6.2 Optical contrast data

In order to measure optical *contrast*, it was of course necessary to capture images in which both the graphene samples and the SiO_2 substrate were clearly visible. Because the natural edges (corresponding to the edges of the copper substrates) of my CVD-grown samples tended to be quite ragged, I intentionally punched holes in the graphene

films during the transfer process, thereby providing cleaner edges of the graphene flakes, which I could clearly visualize against the nominal 300 nm SiO_2 substrate.

In order to quantitatively assess contrast variations, I selected regions of CVD-grown graphene near the edges of the transferred flakes and captured digital images, calibrating them as described in Section 4.6.1. Converting these images to grayscale, I computed pixel-by-pixel histograms of the intensity of reflected light from various interesting sub-regions of each image. For comparison purposes, I have also imaged a number of mechanically-exfoliated graphene samples on SiO_2, produced at Maryland and graciously provided to me by my colleague Dr. Jianhao Chen.

Figure 4.13(b) shows a grayscale optical micrograph of a sample of CVD-grown graphene transferred from copper to nominal 300 nm SiO_2; according to the manufacturer, this particular batch of wafers has a mean thickness of 309.2 nm, with a standard deviation of 1.4 nm. Alongside it, Figure 4.13(a) is a micrograph of two flakes of mechanically-exfoliated graphene (on an SiO_2 wafer from a batch specified as 306.8 nm±0.8 nm).

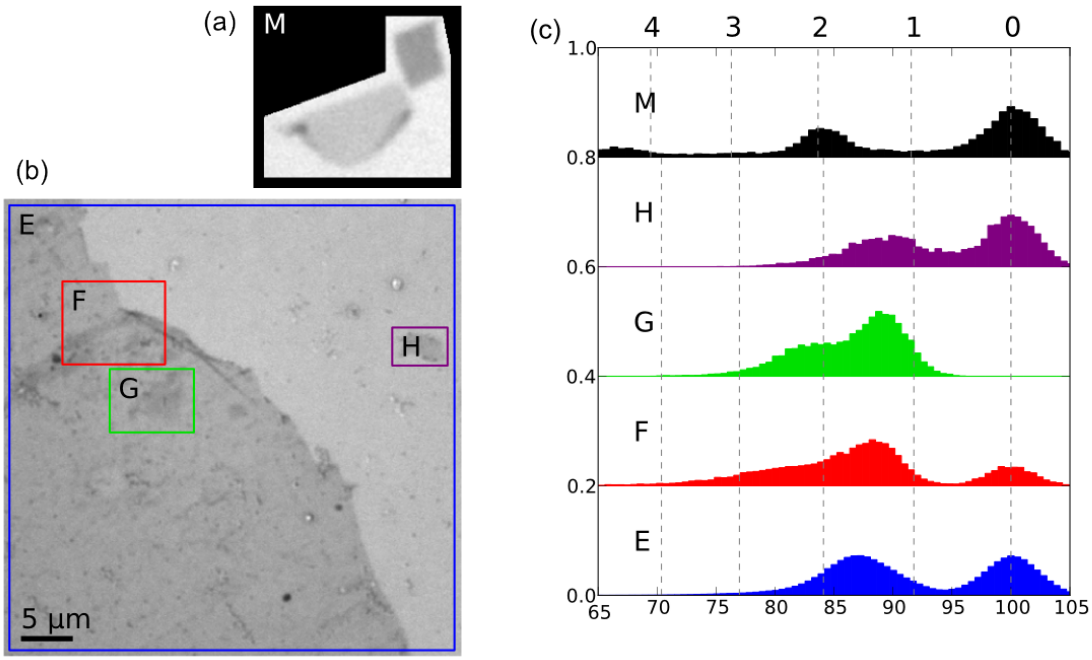

Figure 4.13: Constrast-stretched grayscale optical micrographs of (a) mechanically-exfoliated graphene (bilayer and four-layer islands) and (b) CVD-grown graphene, under a 600 nm filter. A large graphene-free void was intentionally introduced into the sample shown in (b) during the transfer process, in order to facilitate optical contrast measurements. (c) Normalized histograms of the optical contrast of the correspondingly-labeled regions of (a) and (b). Vertical dashed lines in (c) show my theoretical calculations of the contrast expected for graphene of 1-4 layer thickness on SiO_2 substrates of corresponding thickness, assuming an index of refraction of $n_g = 2.0 - 1.1\,j$ for the graphene.

Regions of lighter and darker contrast are clearly visible in Figure 4.13(b). I computed histograms of the optical contrast of all the outlined and marked regions in Figure 4.13(a-b), and plot them in Figure 4.13(c). All of the marked regions, except for

region G, contain an area of SiO_2, and this shows up in the histogram as a prominent intensity peak. I have normalized all the histograms to place the SiO_2 peak at the 100% mark, so that contrast (defined by Equation 4.1) may be read directly off of them. The vertical dashed lines in Figure 4.13(c) indicate the theoretical contrast of 1-4 layer graphene, computed using Equation 4.8 and assuming the index of refraction for graphene measured by Ni et al., $n_g = 2.0 - 1.1\,j$ [141]. Note that the contrast in the printed optical micrographs does not correspond to that actually measured from the digital images, because I have stretched the printed images' contrast to aid the reader in distinguishing darker and lighter regions.

Regions F and G of the CVD graphene micrograph show clear double peaks for graphene in their histograms, at about 80% and 87%. On the other hand, regions E and H show only single peaks, at around 87%.

The mechanically-exfoliated graphene shows two peaks as well, of which one lines up well with the theoretically-predicted contrast of bilayer graphene on 309 nm SiO_2, while the other has slightly greater contrast than the theoretical prediction for 4-layer graphene. In fact, I was able to confirm that the flake shown in the lower left of Figure 4.13(a) is correctly identified as bilayer graphene by measuring its Raman spectra under 514 nm and 633 nm lasers. Shown in Figure 4.14, these spectra show the four characteristic subpeaks of the *2D* band measured by Ferrari et al. on AB-stacked bilayers (see Section 3.6.2) [97].

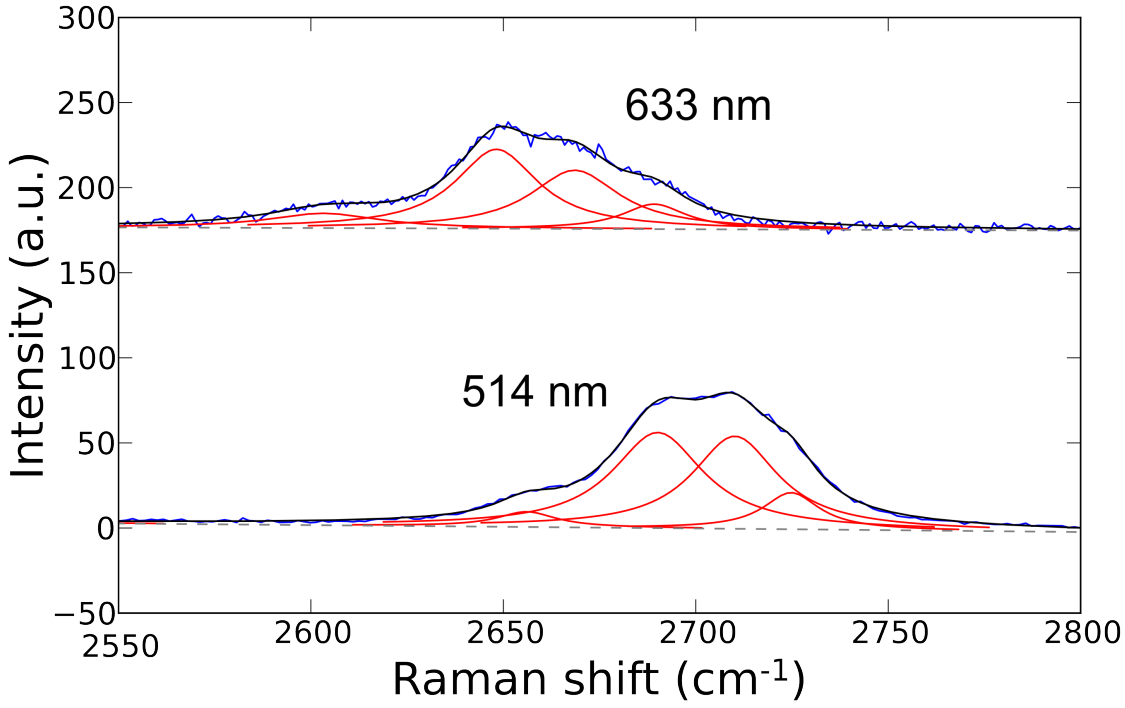

Figure 4.14: A portion of the Raman spectra of the lower-left flake of mechanically-exfoliated graphene shown in Figure 4.13(a). This sample has a sharp G peak at around 1580 cm^{-1} (not shown), no measurable D peak, and the 2D bands shown here. The peak frequencies, relative intensities, and dispersion with laser frequency (106 cm^{-1}/eV, see section 5.2) of the four 2D sub-peaks agree with those measured by Ferrari et al. [97] for bilayer graphene.

The contrast peaks of the CVD-grown graphene do not clearly line up with the theoretically-predicted contrast of 1-4 layer graphene. However, the 12-13% contrast of the first peak agrees with the predicted contrast contrast of monolayer graphene on 310 nm SiO_2, as discussed in Section 4.5.2 and plotted in Figure 4.11, accounting for wide variation in the index of refraction. The additional 7% contrast of the second peak

is at the very low end of the plausible range of contrast for bilayer graphene on 310 nm oxide, according to Figure 4.11.

Using the method of Section 4.5.2, I have calculated that there is no single reasonable value for graphene's index of refraction that would give 12-13% contrast for a monolayer, but only 19-20% for a bilayer. However, as discussed in published reports of graphene's optical contrast, there is good reason to suspect differences in the index of refraction of monolayer and multilayer graphene [141-143],[146]. Because of this, it seems reasonable to conclude that the second contrast peaks of the CVD-grown graphene in Figure 4.13(c) correspond to regions of bilayer graphene.

Figure 4.15 shows an optical micrograph and histograms of another sample of CVD-grown graphene, again alongside the same samples of mechanically-exfoliated graphene. This CVD-grown sample came from a completely separate growth batch from the sample shown in Figure 4.13, and was transferred to the same batch of SiO_2 wafer, with oxide thickness of $309.21\ \text{nm} \pm \sigma = 1.4\ \text{nm}$. In the region shown, this sample of CVD-grown graphene has a much higher uniformity of optical contrast than the previous sample. Again, it has a prominent peak at around 12-13% contrast, probably corresponding to monolayer graphene, and much weaker peaks at higher contrast, probably corresponding to multilayer graphene, although it is difficult to pinpoint their positions precisely.

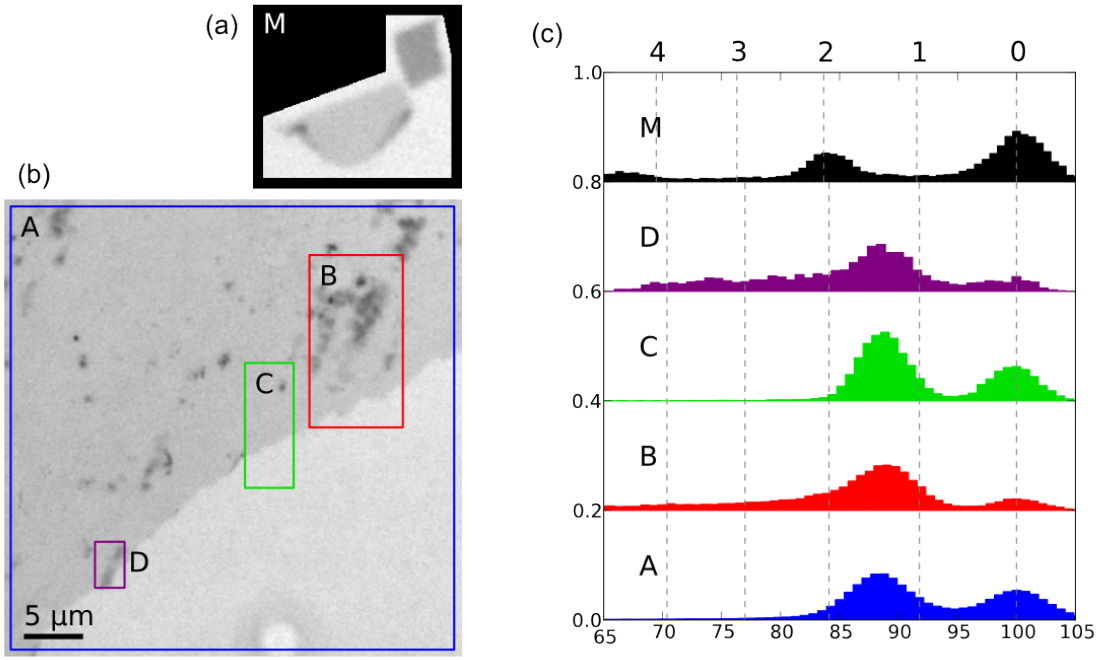

Figure 4.15: Optical micrographs of (a) mechanically-exfoliated graphene (bilayer and four-layer islands) and (b) another sample of CVD-grown graphene, under a 600 nm filter. (c) Normalized histograms of the optical contrast of the correspondingly-labeled regions of (a) and (b). Constructed in the same way as Figure 4.13.

I also measured the optical contrast of both the samples shown in Figure 4.13 and Figure 4.15 under 550 nm filters. However, I found substantial variations in the optical contrast within the CVD-grown samples. For example, I found region H of Figure 4.13 (a small "island" of graphene away from the main flake) to have a contrast that was significantly lower than that of regions E-G. As I discussed in Section 4.5.1, graphene's contrast under 550 nm light is much more sensitive to small variations in oxide thickness than under 600 nm light.

4.6.3 Possible effect of impurities on graphene contrast

As I have shown, my CVD-grown graphene samples show evidence of multilayer graphene in their optical contrast. This result is surprising, given that other researchers have found *low-pressure* CVD growth on copper to produce monolayer graphene almost exclusively [122],[95],[126]. Furthermore, Ruoff and colleagues have explained this result as a consequence of the surface adsorption mechanism by which carbon is deposited on copper; unlike nickel, copper has a very low solubility to carbon at the CVD growth temperature (over 1000°C), so carbon cannot dissolve in it and then precipitate out to form multilayer graphene [125].

As mentioned previously, many of the regions of multilayer graphene on my CVD-grown samples run in parallel bands distributed similarly to the polishing grooves in the copper substrates (see Figure 4.11). I emphasize again that these regions of higher contrast are seen *after* etching the copper and transferring the graphene to SiO_2 substrates.

I have already discussed the sensitivity of optical contrast measurements to the thickness of the oxide substrate (Section 4.5.1) and shown that the differential contrast of additional graphene layers on my CVD-grown samples is within the range predicted by the transfer-matrix method, given the considerable variation of graphene's index of refraction (Section 4.5.2).

I considered a third source of possible inaccuracies in my optical contrast measurements: the possible presence of impurities above or below the transferred graphene on the SiO_2 substrates. For example, a thin layer of water or solvent might be

trapped under the graphene during the transfer process, the graphene might not lie sufficiently flat on the surface in some places, leaving a thin layer of air, or a layer of residual PMMA might remain on top of the graphene. In the case of residual PMMA, the residue would have to be much, much thinner than the 200 nm layer I originally deposited, since at that thickness it is easily detected via Raman spectroscopy [147].

This work was inspired in part by a conversation with Professor Yong Chen of Purdue University, in which he suggested that non-uniform adhesion of graphene to the substrate might explain my optical contrast data. He and his colleagues have argued that non-uniform adhesion may be responsible for variations in the optical contrast and Raman spectra of CVD-grown graphene [134].

In order to estimate the effect of transparent impurities on the optical contrast of graphene, I extended the three-layer model of Blake et al. [65] to include a fourth impurity layer, using one of the two structures in Figure 4.16:

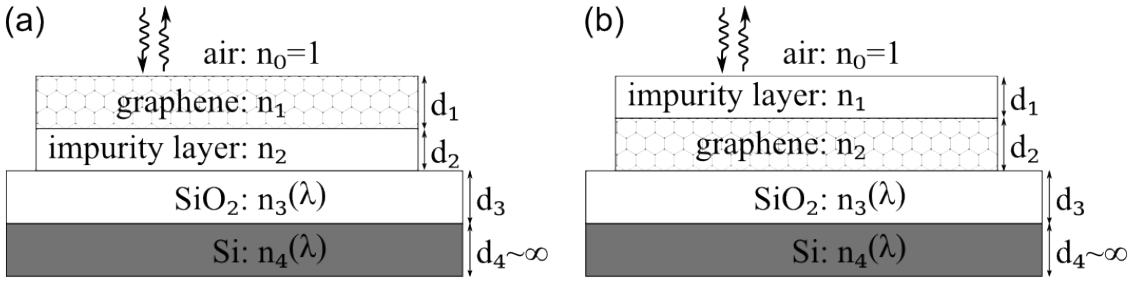

Figure 4.16: Four-layer structures used to model the optical contrast of graphene on oxidized silicon substrates, in the presence of (a) transparent impurities below the graphene or (b) transparent impurities above the graphene.

Again, using the transfer-matrix method derived in Section 4.2.1, I calculated an expression for the intensity reflectance coefficient of a four-layer structure. This formula is substantially lengthier than that of a three-layer structure (Equation 4.8):

$$\begin{aligned} A &= r_{01} + r_{12}e^{2j\phi_1} + r_{23}e^{2j(\phi_1+\phi_2)} + r_{34}e^{2j(\phi_1+\phi_2+\phi_3)} + r_{12}r_{23}r_{34}e^{2j(\phi_1+\phi_3)} \\ &\quad + r_{01}r_{12}r_{23}e^{2j\phi_2} + r_{01}r_{12}r_{34}e^{2j(\phi_2+\phi_3)} + r_{01}r_{23}r_{34}e^{2j\phi_3} \\ B &= 1 + r_{01}r_{12}e^{2j\phi_1} + r_{01}r_{23}e^{2j(\phi_1+\phi_2)} + r_{01}r_{34}e^{2j(\phi_1+\phi_2+\phi_3)} \\ &\quad + r_{01}r_{12}r_{23}r_{34}e^{2j(\phi_1+\phi_3)} + r_{12}r_{23}e^{2j\phi_2} + r_{12}r_{34}e^{2j(\phi_2+\phi_3)} + r_{23}r_{34}e^{2j\phi_3} \\ R &= |A/B|^2 \end{aligned} \tag{4.23}$$

The interlayer amplitude reflection coefficients, r_{ij}, and the optical path differences, ϕ_i, are calculated for normal incidence in the same fashion as in Section 4.3. Using Equation 4.3, and assuming $n_g = 2.0 - 1.1\,j$ for graphene's index of refraction (from Ni et al. [141]), I calculated the effect of up to 4 nm of air or water underneath graphene on 309 nm SiO_2, and the effect of up to 4 nm of PMMA on top of graphene on 309 nm SiO_2. For the indices of refraction of air, water, and PMMA, I used 1.0, 1.33, and 1.49 respectively. The results, again under illumination by light of wavelength 600 nm, are shown in Figure 4.17. It is important to understand that the *contrast* shown in the

figure is the relative change in reflectance between the complete four-layer structure, and the bare substrate without the impurity layer. That is, in analogy to the three-layer case in Equation 4.1, I define the contrast as:

$$C = \frac{I_{\text{w/graphene+impurity}} - I_{\text{substrate}}}{I_{\text{substrate}}} = \frac{R(n_1 = n_2 = 1) - R(n_G, n_{\text{impurity}})}{R(n_1 = n_2 = 1)} \tag{4.24}$$

As Figure 4.17 demonstrates, a layer of air under the graphene has an almost negligible effect on its contrast, while water below and PMMA above have somewhat larger effects. In all cases, thin layers of these impurities act to *decrease* the contrast of graphene on 309 nm SiO_2 (for slightly thinner oxides, e.g. 290 nm or 300 nm, they may actually increase the contrast, however).

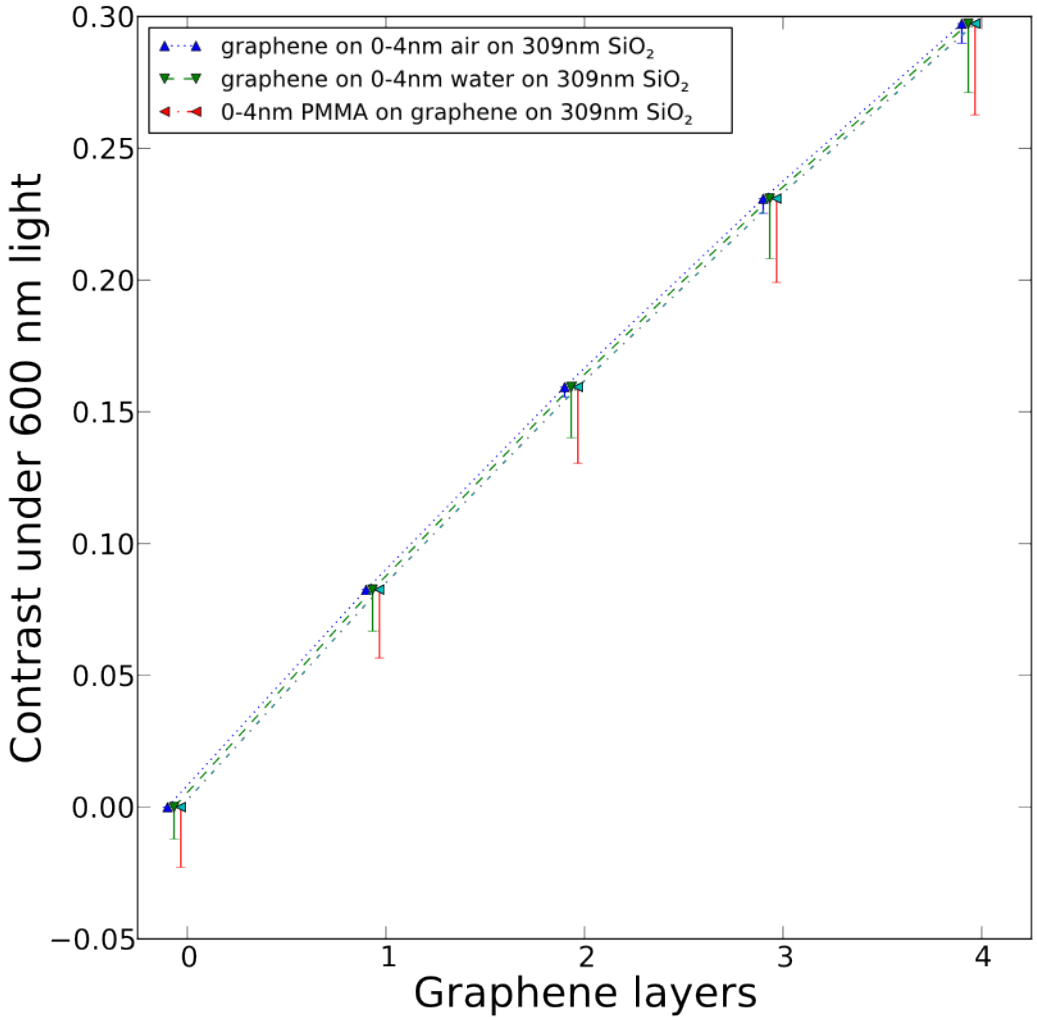

Figure 4.17: Contrast of 1-4 layer graphene on 309 nm SiO_2 with 600 nm illumination, with an air or water layer underneath (as in Figure 4.16(a)) or a PMMA layer above (as in Figure 4.16(b)). The curves show the contrast of the graphene without the impurity layer, with $n_g = 2.0 - 1.1\,j$ as the index of refraction of graphene. The error bars show the range of contrasts with 0-4 nm of the impurity layer.

More importantly, Figure 4.17 shows that for few-layer graphene, the effect of adding a transparent impurity layer is nearly independent of the thickness of the graphene. That is, adding 2.5 nm of water below monolayer graphene changes the contrast by nearly the same amount as adding 2.5 nm of water below 3-layer graphene, for example.

As a result, the presence of these transparent impurities may *shift* the contrast of graphene but it will not significantly affect the *spacing* of the contrast between graphene of different layer thicknesses. In other words, the range of differential contrasts shown in Figure 4.11 remains valid even with thin impurity layers. Thin layers of impurities therefore cannot explain the multiple contrast peaks which I observe on CVD-grown graphene. The presence of graphene multilayers remains the best explanation for the variable optical contrast that I have observed.

4.7 Conclusions

Using the transfer-matrix method of thin-film optics, I have calculated the expected optical contrast of graphene and graphene multilayers on SiO_2 substrates. I have considered and quantified numerous sources of error and uncertainty in the measured contrast, and showed how to minimize them through judicious choices of oxide thickness and optical filters. I measured the optical contrast at various wavelengths of my graphene samples, grown via chemical vapor deposition on copper, and of reference samples of mechanically-exfoliated graphene.

From these optical contrast measurements, I found evidence of multilayer graphene in my CVD-grown samples. This result is very surprising, given several reports

of *low-pressure* CVD growth on copper, which has been found to produce monolayer graphene almost exclusively [95],[122],[126]. Consequently, I turned to two other characterization techniques, Raman spectroscopy and atomic force microscopy, in order to find further evidence supporting the conclusion of multilayer growth, as discussed in Chapter 5.

5. Raman and atomic force microscopy study of CVD-grown graphene

5.1 Motivation

In Chapter 4, I introduced the transfer-matrix method of thin-film optics, and explained how it could be used to identify graphene on insulating substrates and to detect variations in the thickness of graphene multilayers, despite considerable sample-to-sample variation in graphene's optical properties. From optical contrast, I found evidence of multilayer graphene in my samples of graphene grown via atmospheric-pressure chemical vapor deposition (CVD) on copper foils.

These results differ sharply from published reports of *low-pressure* CVD growth on copper, which has been found to produce monolayer graphene almost exclusively [122],[126],[95]. Lee et al., however, found some evidence of bilayer graphene from atmospheric-pressure CVD growth [122], but did not explore this in depth. As discussed in Section 3.8.1, Ruoff and colleagues have shown that, in low-pressure CVD, graphene forms on Cu exclusively by surface adsorption of carbon, a process which is self-limited to a single monolayer [125].

To further study the properties of my CVD-grown graphene, including regions of multilayer graphene, I used Raman spectroscopy. I previously introduced Raman spectroscopy in Section 3.6.1, and explained the prominent Raman peaks of mechanically-exfoliated graphene in Section 3.6.2.

5.2 Raman D and 2D modes

The Raman *D* mode of graphene appears only in small or highly-defected crystals of graphene or graphite. It is not Raman active in extended crystals because it involves double-resonant scattering of a single phonon with non-zero crystal momentum ($q \neq 0$). This mode is suppressed in extended defect-free lattices, where crystal momentum is conserved, and so it can be used to detect structural or electronic disorder [97],[148], [104].

The Raman *2D* mode, on the other hand, is present in large, low-defect samples of graphene, along with the ubiquitous *G* peak of graphitic materials [97],[96]. The *2D* mode occurs due to a double-resonance, two-phonon process. In extended crystals, single-phonon Raman modes are insensitive to the energy of the incident laser, because the phonon crystal momentum is fixed at $q = 0$, and thus the phonon energy does not vary with laser energy. However, in a two-phonon process the phonons can have non-zero, opposite crystal momenta, q and $-q$, since their sum still adds to zero.

As discussed in Section 3.3, the tight-binding model predicts a nearly linear low-energy dispersion for graphene's electronic band structure. This linear dispersion around the *K* and *K′* points of the first Brillouin zone (where the valence and conduction bands touch) is depicted schematically in Figure 5.1:

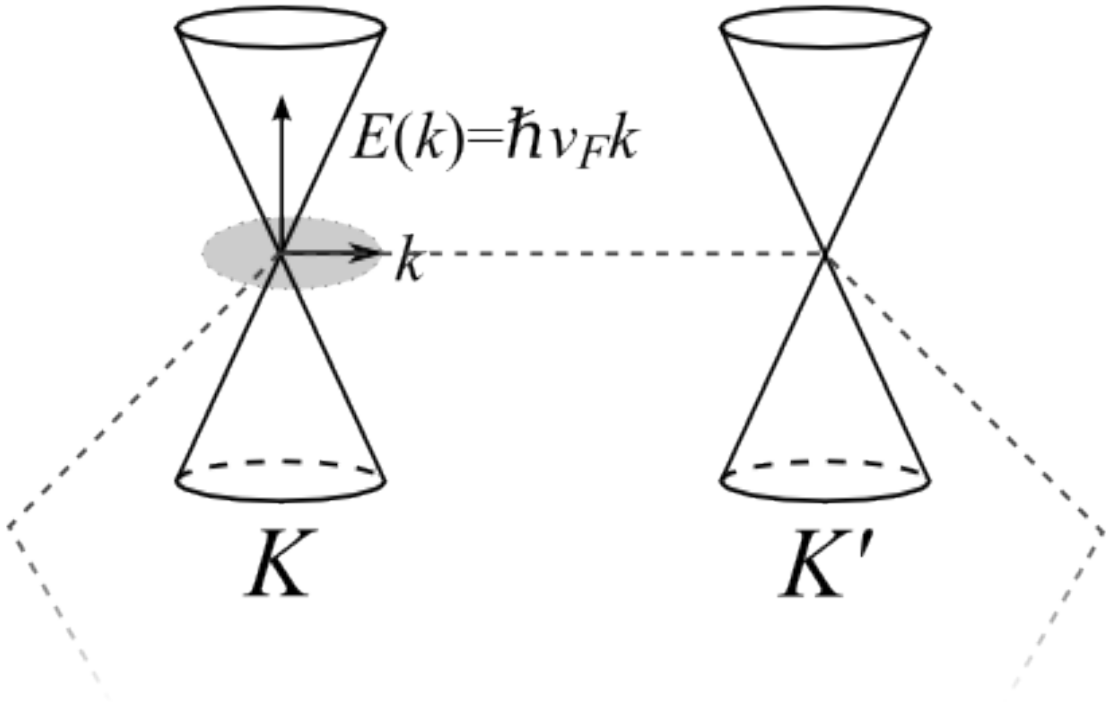

Figure 5.1: Low-energy electronic band structure of graphene. The valence and conduction bands meet at the K and K′ points of the hexagonal first Brillouin zone, and near these points the energy is nearly linear with respect to crystal momentum, ***k****, that is* $E(\boldsymbol{k})=\hbar v_F|\boldsymbol{k}|$ *where* v_F *is the Fermi velocity. This is a more schematic version of Figure 3.2.*

In the Raman *2D* process, a photon of energy E_{laser} excites an electron vertically from the valence to the conduction band, leaving behind a hole in the valence band. The energies of the electron and the hole are $\pm E_{laser}/2$, respectively. Due to the linear dispersion, their momenta are $k=\pm E_{laser}/2\hbar v_F$. The electron and phonon each scatter from near the *K* point to near the *K′* point (known as intervalley scattering), or vice versa. The double resonance condition is satisfied, maximizing the scattering probability, when

the electron and phonon scatter to points with precisely the opposite crystal momenta [148],[149], which gives phonons with momenta,

$$\begin{aligned} q &= (k_{K'} + E_{laser}/2\hbar v_F) - (k_K - E_{laser}/2\hbar v_F) \\ &= (k_K - k_{K'}) - E_{laser}/\hbar v_F \end{aligned} \tag{5.1}$$

Normally, there is no dispersion of either Brillouin zone-center ($q = 0$) or zone-boundary optical Raman modes. The phonon dispersion around the *K* and *K′* points in graphene is due to a Kohn anomaly, a point of high electron-phonon coupling [150]. This gives a dispersion with respect to laser energy of the *2D* Raman mode which is in good agreement with experimental results [148]:

$$\frac{\partial \omega_{2D}}{\partial E_{laser}} \approx 106 \text{ cm}^{-1}/\text{eV} \tag{5.2}$$

This is twice the dispersion of the *D* band, which is a single-phonon double-resonance process that occurs only in the presence of defects [148].

The *2D* band of graphene (as well as the *D* band) is sensitive to changes in graphene's electronic and phonon structure [148],[97],[103]. For example, Berciaud et al. found a pronounced difference in the relative intensity of the *2D* and *G* bands in monolayer graphene, depending on whether it was supported by a substrate or suspended over a trench; they speculate that this is due to changes in the phonon dispersion in free-standing graphene [149].

As I discussed previously in Section 3.6.2, Ferrari et al. carefully measured the Raman spectra of AB-stacked mechanically-exfoliated graphene of 1-10 layer thickness, and found systematic changes in the *2D* band with layer number [97]. They attributed these changes primarily to the electronic band structure of multilayer graphene. In particular, the valence and conduction bands of monolayer graphene split into *four* bands

in bilayer, AB-stacked graphene, which has four atoms per unit cell (two in each layer). These give four different slightly different possible values for the phonon momenta exchanged in the *2D* process, explaining the four characteristic sub-peaks of the Raman *2D* band in bilayer graphene [97].

5.3 Raman on CVD-grown graphene

As described in Section 3.9, I grew graphene on copper foils using atmospheric-pressure chemical vapor deposition, and transferred the graphene to SiO_2 substrates. Having found evidence of multilayer graphene via optical contrast measurements on many of my samples, I returned to measure their Raman spectra in order to see if it would provide further evidence for their multilayer characteristics.

Figure 5.2(b) shows Raman spectra for the same sample of CVD-grown graphene whose optical contrast properties were shown in Figure 4.13, alongside the Raman spectrum of a mechanically-exfoliated graphene bilayer for comparison. To produce these spectra, I used a Horiba J-Y Raman microscope equipped with a green 514 nm argon laser, taking care to reduce the laser power to minimize the effects of sample heating [97],[151]. The spatial resolution of the instrument is approximately 1 μm.

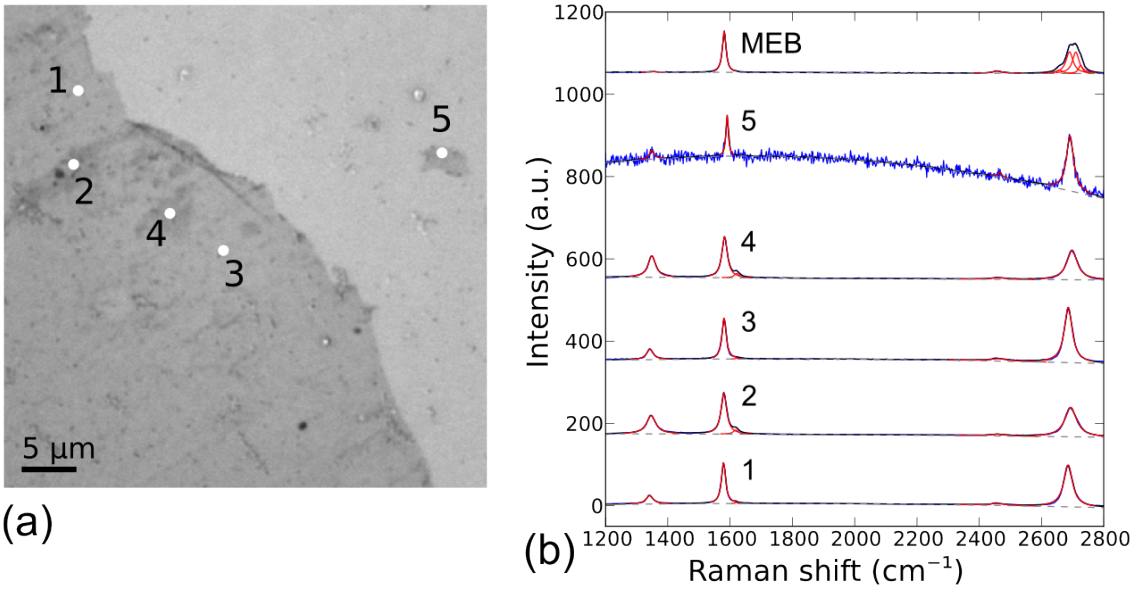

Figure 5.2: (a) Contrast-stretched optical micrograph of CVD-grown graphene illuminated by 600 nm light (same image shown in Figure 4.13(a)) (b) Raman spectra of the points indicated on the sample in (a), along with a Raman spectrum of a mechanically-exfoliated graphene bilayer on SiO_2 substrate for comparison. All spectra were taken using a Horiba J-Y Raman microscope and 514 nm laser at low power. Blue curves in (b) show actual measured data, while red curves show Lorentzian fits to the Raman peaks.

In Figure 5.2(b), I also show fits to the *D*, *G*, and *2D* peaks of the Raman spectra. I fit these spectra using a quadratic background ($I_{BG}(f) = A f^2 + B f + C$) and a scaled Lorentzian distribution for each peak,

$$I(f; f_0, W, I_0) = \frac{I_0}{1 + \left(\frac{f - f_0}{W}\right)^2} \tag{5.3}$$

The spectra in Figure 5.2(b) show substantial variations. I believe that spots 1, 3, and 5 are single-layer graphene, based on their optical contrast, while spots 2 and 4 are bilayer graphene. Spots 1, 3, and 5 show higher *2D*-peak intensity than *G*-peak intensity, that is $I_{2D}/I_G > 1$, while this is reversed for spots 2 and 4. Spots 2 and 4 also show slightly higher center position of their *2D* peaks, and broader peaks ($W \approx 40$ cm^{-1} versus about 30 cm^{-1} for spots 1, 3, and 5). The fitting parameters for all of these spectra are listed in Table 1 at the end of this chapter.

Several other reports of multilayer CVD-grown graphene (primarily on nickel) have used the I_{2D}/I_G ratio to distinguish multilayer and single-layer graphene [122], [128],[94], but this may be unreliable because it is sensitive to the adhesion of the graphene to the substrate [103] and to doping from charged impurities in the substrate [152].

In Figure 5.3, I show Raman spectra for another sample of CVD-grown graphene; this is the sample whose optical contrast properties were shown in Figure 4.15. Spectra were produced in the same fashion as described above for the previous sample (shown in Figure 5.2). I believe that spots 6 and 7 are single-layer graphene, based on their optical contrast, while 9 and 10 are bilayer graphene. Again, I find that $I_{2D}/I_G > 1$ for spots 6 and 7, while $I_{2D}/I_G < 1$ for spots 8 and 9. Spots 8 and 9 also show up-shifted and broader *2D* peaks compared to spots 6 and 7.

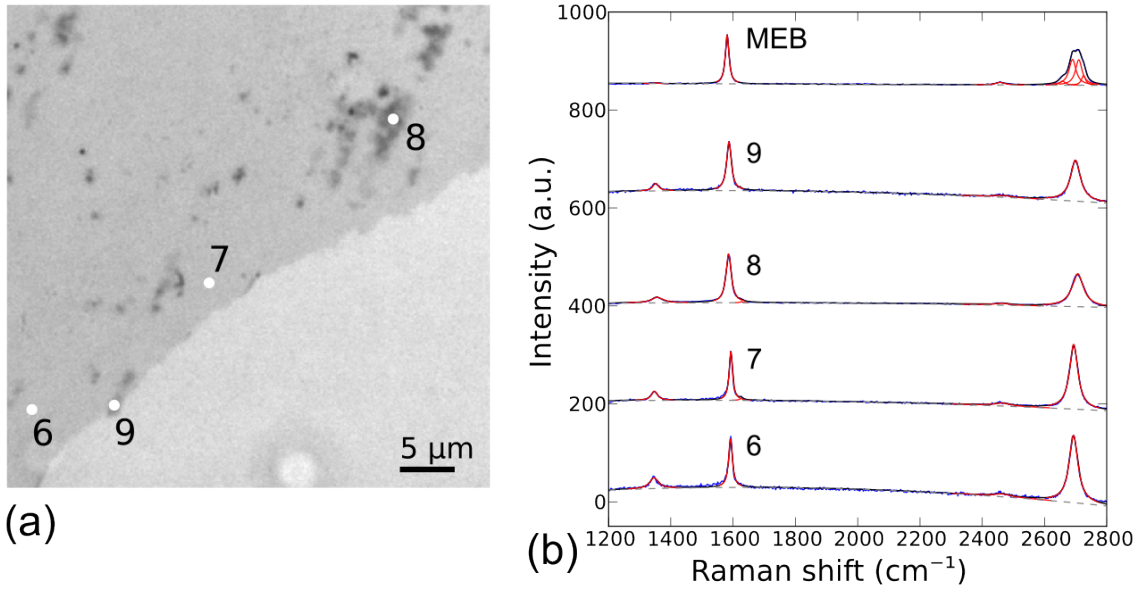

Figure 5.3: Contrast-stretched optical micrograph of CVD-grown graphene illuminated by 600 nm light (same image shown in Figure 4.15(a)) (b) Raman spectra of the points indicated on the sample in (a), along with a Raman spectrum of a mechanically-exfoliated graphene bilayer on SiO_2 substrate for comparison. As in Figure 5.2, all spectra were taken with a 514 nm laser at low power.

All the Raman spectra of CVD-grown graphene, described above, show substantial *D* peaks, $I_D/I_G \approx 0.1-0.4$ in their 514 nm Raman spectra, indicating structural or electronic disorder. Reports of CVD-grown graphene have generally showed higher *D* peak intensity than is found in high-purity mechanically exfoliated samples [122],[134], although my samples have higher *D* peaks than most. Interestingly, the Raman spectra of the higher-contrast spots in Figure 5.2 have higher-intensity *D* peaks than the lower-contrast spots (see Table 1), while all the spots in Figure 5.3 seem to have similar *D* peak intensity.

To illustrate the systematic variation of the Raman spectra between the spots with low optical contrast, and the spots with higher optical contrast, in Figure 5.4 I have plotted the *2D* peak positions, *2D* peak widths, and I_{2D}/I_G for the Raman spectra of spots 1-9, visually distinguishing the spectra taken from low-contrast and high-contrast spots. While it is difficult to draw any strong conclusions from such a small sample size, the plots show that there is little overlap in these parameters between the two groups. In particular, Figure 5.4(c) shows a large difference in the I_{2D}/I_G Raman intensity ratios of the low-contrast and high-contrast spots.

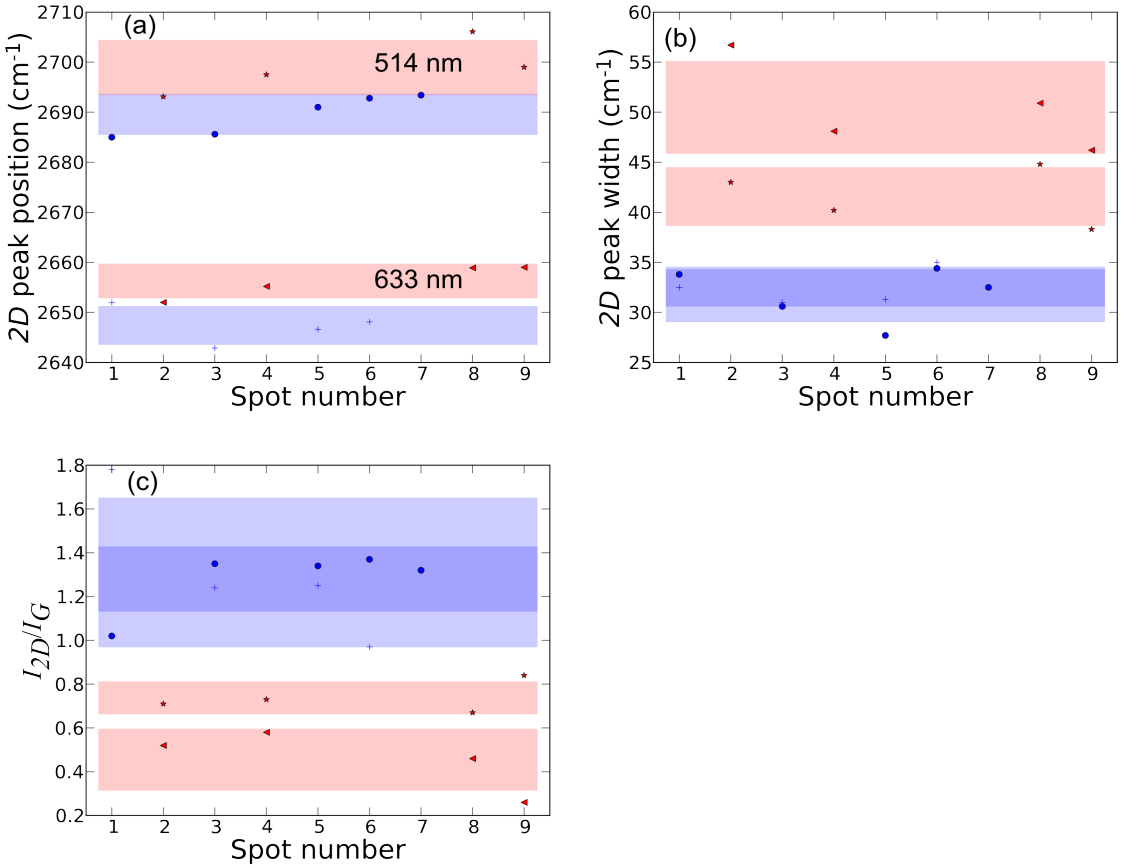

Figure 5.4: (a) 2D peak positions, (b) 2D peak widths, and (c) relative intensity of 2D peaks for the Raman spectra taken at the spots indicated in Figure 5.2 and Figure 5.3. Blue circles (514 nm) and crosses (633 nm) indicate points which I believe to be monolayer graphene, based on their optical contrast, while red stars (514 nm) and triangles (633 nm) indicate points which I believe to be multilayer graphene. Colored bands indicate $\langle x \rangle \pm \sigma_x$ *range for each parameter, grouped by contrast and laser wavelength. All data are taken from Table 1.*

5.4 Evidence for misoriented multilayers

One of the most surprising features of the Raman spectra of my CVD-grown graphene is the *absence* of the asymmetrical *2D* band seen in multilayer, AB-stacked graphene (such as the bilayer sample whose spectrum I have added to Figure 5.2 and Figure 5.3 for comparison with the CVD samples). As discussed in Section 5.2, this multi-peaked *2D* band is well-understood in terms of the differences between the electronic band structure of single-layer and multilayer graphene.

This is a surprising result, and calls into question my contrast-based identification of regions of multilayer graphene. In fact, when I began to synthesize and characterize CVD-grown graphene, I was puzzled by the wide variation in Raman spectra and optical contrast which I observed. The asymmetrical *2D* band is not only absent from the spectra which I have presented above in Section 5.3: in over 6 months of studying graphene grown on copper foils, and inspecting hundreds of Raman spectra, I have *never* seen a clearly asymmetrical *2D* band.

In fact, similar Raman spectra have been previously observed in multilayer graphene. Poncharal et al. measured the Raman spectra of two flakes of monolayer graphene and the region where these two overlapped on their SiO_2 substrate [101]. They observed a monolayer-like Raman spectrum in the overlap region, which they termed misoriented graphene (it is also sometimes known as turbostratic graphene). In Figure 5.5(b-c) I reproduce the Raman spectra summarizing their findings:

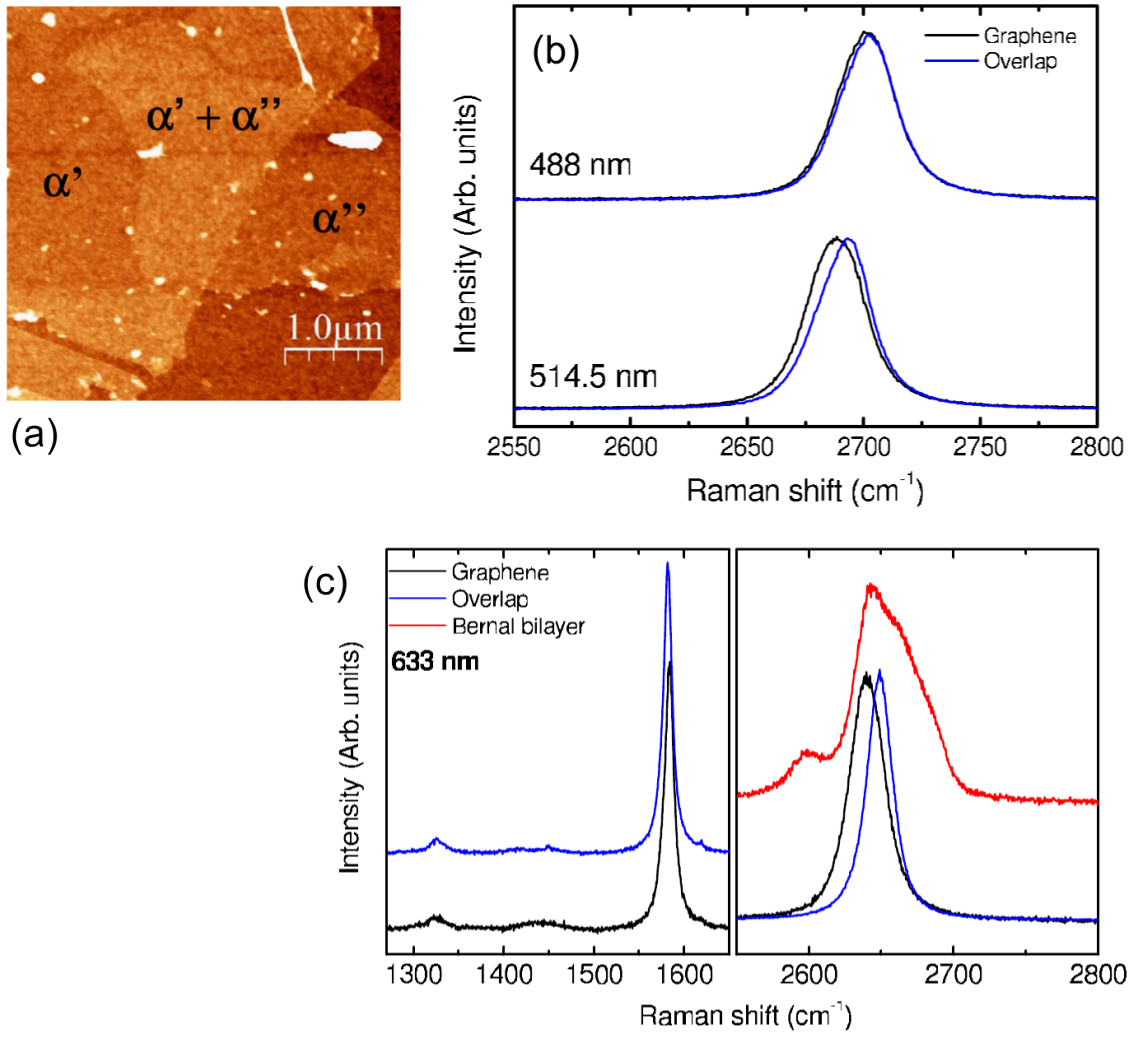

Figure 5.5: Study of Raman spectra of misoriented graphenes by Poncharal et al. (a) Atomic force microscopy (AFM) topography image of two overlapping samples of monolayer graphene on SiO_2, marked α' and α'' individually. (b) Comparison of the Raman 2D peaks of the monolayer graphene regions and their overlap, with 488 nm and 514 nm lasers. (c) Comparison of the Raman G and 2D peaks of monolayer graphene, overlap region, and Bernal (AB-stacked) bilayer graphene, with 633 nm laser. (From [101])

The results of Poncharal et al. in Figure 5.5(b-c) show that the center position of the Raman *2D* peak is higher in the bilayer overlap region than in the monolayer graphene (6 cm^{-1} higher with 514 nm laser, 9 cm^{-1} higher with 633 nm). They also observed an up-shift in the *G* peak center position of the bilayer overlap region. The authors explain the monolayer-like Raman spectrum of the misoriented graphene bilayer by its reduced interlayer coupling, compared to an AB-stacked bilayer [101]. Because the two layers of the misoriented bilayer are rotated with respect to one another at some unknown angle, as shown in Figure 5.6, this structure does not possess the extended symmetry of an AB-stacked bilayer, in particular its 4-atom unit cell. Since the four Raman *2D* sub-peaks of an AB bilayer come from its distinct electronic band structure (see Section 5.2), they do not appear in the misoriented sample.

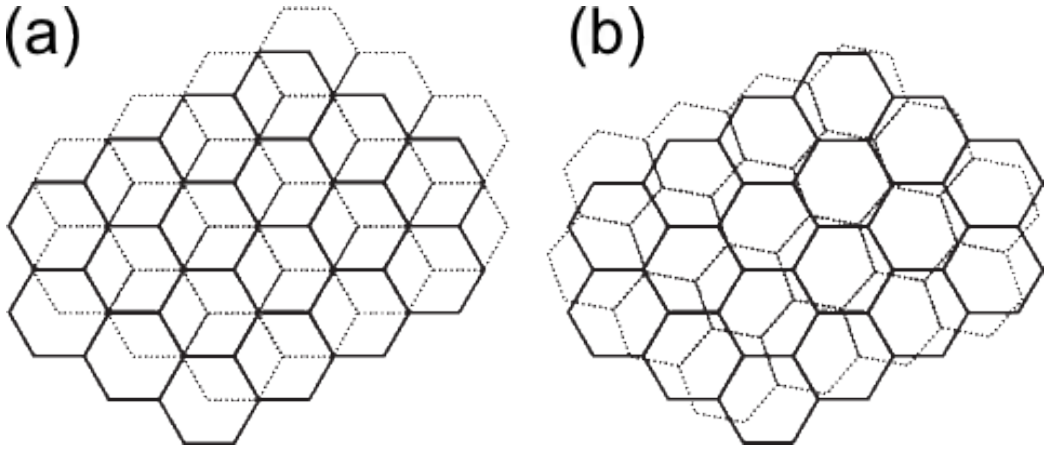

Figure 5.6: Stacking of (a) AB-stacked or Bernal graphene bilayer and (b) misoriented graphene bilayer, viewed along the c-axis, perpendicular to the individual graphene planes. (From [98].)

My results on CVD-grown graphene resemble those of Poncharal et al. in many ways. With both 514 nm and 633 nm lasers, I find Raman *2D* peak center positions about

8 cm^{-1} higher in the spectra of points with higher optical contrast, than in the spectra of points with lower optical contrast; this can be seen in the mean values of Figure 5.4(a). Poncharal et al. did not find increased *2D* peak width in their misoriented graphene bilayer, in contrast to my observations. However, a single *2D* peak with a width of about 40 cm^{-1} *has* been reported for turbostratic graphite, by Pimenta et al. [104].

5.4.1 Similar results in other forms of graphene

Single-layer-like Raman spectra have also been observed in epitaxial graphene grown on the carbon face $(000\bar{1})$ of silicon carbide (see Section 3.7.4 for a discussion of this synthesis technique) [153],[154]. The multilayer, rotationally-disordered character of these samples has been confirmed via electron diffraction and other techniques [102].

I have also observed mechanically-exfoliated graphene samples produced in my group, which appear to contain overlapping flakes of different thicknesses, which also have monolayer-like spectra similar to those seen by Poncharal et al.

Similar Raman spectra have been shown by Lee et al. and by Cao et al., which are to my knowledge the only published reports of graphene grown via atmospheric-pressure CVD on copper [122],[134]. Both report substantial variations in I_{2D}/I_G while retaining the single-peaked *2D* band, and they identify the regions with lower values of this ratio as probable bilayer or multilayer graphene. Neither, however, remarks on the significance of this result to the stacking order of the multilayer graphene. In their report on one-few layer graphene grown via atmospheric-pressure CVD on nickel, De Arco et al. show similar Raman spectra as well, include a broadened, upshifted, symmetrical *2D* band [128]. They attempt to fit this to the four *2D* sub-peaks of AB-stacked bilayer graphene,

however. This seems questionable to me, since the relative intensities and positions of their sub-peaks differ significantly from those reported by Ferrari et al. [97].

5.5 Atomic force microscopy

In order to further study the thickness of graphene grown via chemical vapor deposition on copper, I have also performed atomic force microscopy (AFM) scans of several samples of CVD-grown graphene transferred onto SiO_2 substrates. In tapping-mode atomic force microscopy, a sharp probe mounted on an oscillating cantilever is scanned across the surface of the sample being studied. The amplitude of the oscillations is affected by the interaction of the surface with the approaching tip. A feedback loop adjusts the height of the tip to maintain a constant amplitude. This approach typically gives a more reliable measurement of the sample's surface topography in ambient conditions, where a layer of water may be adsorbed on the surface, causing stick-slip interactions with the tip in contact-mode AFM.

5.5.1 Caveats for graphene

Tapping mode AFM can provide very high-resolution topography images of a sample, a few nm in-plane (limited by the tip size and shape) and 0.1 nm vertically for the Veeco DI-5000 AFM which I have used. Although AB-stacked graphite has a well-known interlayer spacing of 0.34 nm, it is difficult to use AFM to precisely measure the thickness of few-layer graphene on SiO_2 substrates. Novoselov et al. and Gupta et al. have measured offsets of 0.3-1 nm in the thickness of monolayer mechanically-exfoliated graphene on SiO_2, an effect that may be due to an adsorbed water layer on the substrate

[144],[68]. Recently, Nemes-Incze et al. demonstrated substantial variations (up to a factor of 4) in the height of few-layer graphene on SiO_2 measured by ambient tapping-mode AFM [155]. They attribute this to a delicate balance between long-range attractive and short-range repulsive interactions between the tip and the sample, which may be different for graphene and SiO_2. They advise that an atomic force microscope should be calibrated to ensure that repulsive interactions dominate in order to more reliably measure the thickness of few-layer graphene [155].

5.5.2 Graphene steps

Despite the difficulty of reliably measuring the total thickness of graphene via AFM, it remains a very sensitive technique which can be used to detect small changes in sample topography. For graphene-to-graphene steps, it reliably resolves the interlayer spacing of 0.34 nm. In order to detect multilayer graphene, I performed tapping-mode AFM scans around the edges of CVD-grown graphene transferred onto SiO_2 substrates.

It has been difficult to find large, flat areas around the edges of the graphene flakes which were not contaminated with particles (likely PMMA from the transfer process), but I did manage to locate a few, although they did not correspond precisely to regions where I made Raman or optical contrast measurements. Figure 5.7(a) is a tapping-mode AFM image which I took near the edge of a piece of CVD-grown graphene transferred to SiO_2. A step from the SiO_2 substrate to the graphene flake is visible, with a height measured to be 2.0 nm, as shown in Figure 5.7(b). After the initial step from the SiO_2 substrate, there is another step with a height measured to be 1.0 nm, indicating one or more additional monolayers of graphene.

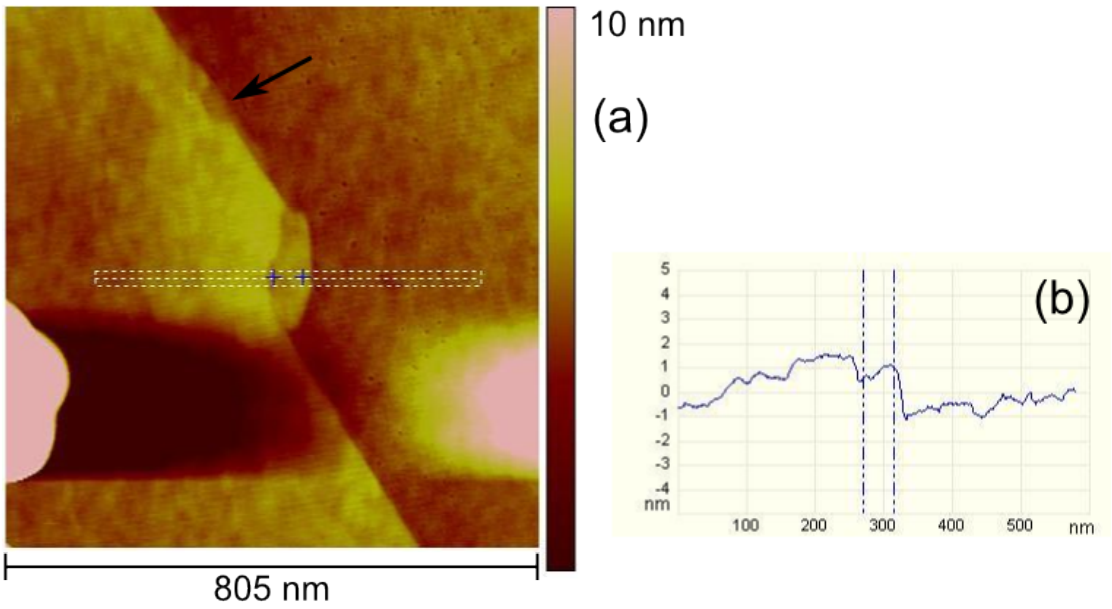

Figure 5.7: (a) Tapping-mode ambient AFM topography image of graphene step edges. This is a sample of CVD-grown graphene transferred from copper to nominal 300 nm SiO_2. (b) Line profile of sample height along the length of the dashed box in (a), averaged across its width. A step from the SiO_2 substrate to the graphene is visible, followed by a second step indicating one or more monolayers of graphene on top of the first. The arrow in (a) indicates another such step visible nearby on this sample. Crosses in (a) and dashed vertical lines in (b) indicate edges of the first step from SiO_2 to graphene.

The presence of such steps around the edges of flakes of CVD-grown graphene flakes is further evidence for regions of multilayer thickness.

5.6 Conclusions

I have grown large sheets of graphene using atmospheric-pressure chemical vapor deposition, described in Section 3.9, a synthesis technique which uses comparatively low-cost copper foil substrates. While my samples appear to contain higher levels of defects than those grown via low-pressure CVD, they show a number of interesting features.

Optical contrast measurements of my CVD-grown graphene show substantial regions of relatively uniform contrast, in line with the predictions of the transfer-matrix method (described in Section 4.2.1) and published reports of the optical characteristics of single-layer graphene. However, they also reveal areas of increased optical contrast, which seem to correspond to multilayer graphene. Unlike AB-stacked multilayer graphene, regions of multilayer graphene on my CVD-grown samples consistently show only a single-peaked Raman *2D* band. Their Raman spectra differ from those of monolayer graphene, however, in a shift and broadening of this *2D* peak, in line with many published reports of misoriented multilayer graphene (see Section 5.4). When graphene layers are rotationally disordered, the extended three-dimensional symmetry of the lattice is broken, and the electronic structure more closely resembles that of monolayer graphene [104].

At present, there is no known growth mechanism that can explain the formation of multilayer graphene on copper. As demonstrated by Ruoff and colleagues, low-pressure CVD (~ 500 mTorr) on copper forms graphene exclusively by surface adsorption, a self-limiting process which produces only a single monolayer [125]. In private conversations

with Ruoff, I have verified that his low-pressure CVD synthesis experiments employ the same commercially-available copper foil substrates which I have used.

My results shed light on the formation of graphene on copper at high pressure. Because the layers of CVD-grown graphene are not stacked in a regular fashion, it seems likely that they do not form via a layer-by-layer epitaxial process of nucleation and island growth, as observed at low pressure. Furthermore, regions of multilayer graphene often seem to fall in parallel bands distributed similarly to polishing grooves on the original copper substrates, suggesting an important role for the substrate topography in their formation. This contrasts with reports of CVD-grown graphene extending across many crystalline grains of copper in low-pressure growth [95],[135].

5.7 Future work

To further investigate the mechanisms of graphene formation on copper and other metal substrates, it would be useful to perform chemical vapor deposition at intermediate pressure, above the 500 mTorr range used for low-pressure CVD. This could reveal a sharp or gradual transition between exclusively monolayer growth, and multilayer growth. Blocking studies, in which growth is stopped before a complete monolayer has formed, could also provide insight by revealing the shape and structure of isolated graphene islands and possible interactions with sharp edges or depressions in the substrate.

To my knowledge, no such experimental results have yet been published. However, Luigi Colombo of Texas Instruments has begun work in this area, studying the

growth dynamics of graphene on copper foils in collaboration with Ruoff and other researchers.

If atmospheric-pressure growth of low-defect, exclusively monolayer graphene on copper can be perfected, this may be the simplest and lowest-cost synthesis method available. This could hasten commercialization of graphene-based electronic devices, especially for large-area applications such as transparent conducting films, where only modest electronic transport performance is required to compete with existing materials such as indium tin oxide.

5.8 Raman data summary

	Laser	*G* peak		*D* peak			*2D* peak			*D′* peak	
Spot	λ (nm)	f_0 (cm^{-1})	W	f_0	W	I/I_G	f_0	W	I/I_G	f_0	I/I_G
1	514	1579.0	15.9	1341.9	26.1	0.21	2685.0	33.8	1.02	2456.4	0.05
	633	1582.5	13.6	1322.3	37.5	0.48	2652.0	32.5	1.78	2459.3	0.09
2	514	1580.0	21.5	1346.7	33.1	0.44	2693.1	43.0	0.71	2455.6	0.04
	633	1582.6	21.7	1327.3	38.8	1.20	2652.0	56.7	0.52	2467.1	0.06
3	514	1580.7	15.9	1342.8	25.1	0.25	2685.6	30.6	1.35	2459.4	0.06
	633	1586.3	10.6	1322.4	23.9	0.60	2642.9	31.0	1.24	2453.1	0.06
4	514	1582.4	21.0	1349.0	28.6	0.53	2697.5	40.2	0.73	2457.7	0.04
	633	1584.7	20.6	1329.4	31.2	1.40	2655.2	48.1	0.58	2469.8	0.06
5	514	1590.5	9.1	1348.8	16.6	0.22	2691.0	27.7	1.34	2466.4	0.13
	633	1589.0	11.2	1325.1	24.6	0.50	2646.6	31.3	1.25	2459.9	0.10
6	514	1591.7	14.5	1346.1	33.2	0.22	2692.8	34.4	1.37	2463.1	0.06
	633	1592.8	12.3	1324.8	24.9	0.47	2648.1	35.0	0.97	2475.3	0.04
7	514	1592.8	12.9	1347.8	23.8	0.19	2693.4	32.5	1.32	2462.6	0.06
8	514	1585.8	20.1	1355.3	40.9	0.12	2706.1	44.8	0.67	2461.5	0.04
	633	1584.0	20.3	1331.3	47.1	0.28	2658.9	50.9	0.46	2467.7	0.04
9	514	1586.8	18.1	1351.5	22.4	0.15	2699.0	38.3	0.84	2463.5	0.04
	633	1584.9	15.9	1330.5	36.0	0.18	2659.0	46.2	0.26	2466.0	0.02
MEB	514	1581.0	14.2	1352.8	15.2	0.01				2457.5	0.05
	633	1581.2	12.4			0.00				2471.5	0.04

Table 1: Summary of the parameters used to fit the peaks of the Raman spectra discussed in this chapter. All peak center frequencies, f_0, and peak widths, W, are in units of cm^{-1}, while relative peak intensity, I/I_G, is a unitless quantity. Data for the 2D peak of the mechanically-exfoliated bilayer sample are not listed, because it cannot be fit by a single Lorentzian.

Glossary of acronyms

AFM	Atomic force microscopy
CMOS	Complementary metal-oxide semiconductor
CVD	Chemical vapor deposition
FET	Field-effect transistor
HOPG	Highly-oriented pyrolitic graphite
IC	Integrated circuit
ITO	Indium tin oxide
LCD	Liquid crystal display
MOSFET	Metal-oxide-semiconductor field-effect transistors
MWNT	Multi-walled carbon nanotube
NA	Numerical aperture
NMOS	*N*-channel metal-oxide semiconductor
P3HT	Poly(3-hexylthiophene)
PMMA	Poly[methyl methacrylate]
PMOS	*P*-channel metal-oxide semiconductor
RCTL	Resistor-capacitor transmission line
SAM	Self-assembled monolayer
SCCM	Simple cubic centimeters per minute
SWNT	Single-walled carbon nanotube
TEM	Transmission electron microscopy
TFT	Thin-film transistor
UDR	Universal dielectric response

Bibliography

[1] C. Jacoboni, C. Canali, G. Ottaviani, and A. Alberigi Quaranta, "A review of some charge transport properties of silicon," *Solid-State Electronics*, vol. 20, Feb. 1977, pp. 77-89.

[2] T. Dürkop, S.A. Getty, E. Cobas, and M.S. Fuhrer, "Extraordinary Mobility in Semiconducting Carbon Nanotubes," *Nano Letters*, vol. 4, Jan. 2004, pp. 35-39.

[3] K.I. Bolotin, K.J. Sikes, J. Hone, H.L. Stormer, and P. Kim, "Temperature-Dependent Transport in Suspended Graphene," *Physical Review Letters*, vol. 101, 2008, p. 096802.

[4] B. Van Zeghbroeck, *Principles of Semiconductor Devices*, 2007.

[5] M.C.J.M. Vissenberg and M. Matters, "Theory of the field-effect mobility in amorphous organic transistors," *Physical Review B*, vol. 57, May. 1998, p. 12964.

[6] J.H. Worne, J.E. Anthony, and D. Natelson, "Transport in organic semiconductors in large electric fields: From thermal activation to field emission," *Applied Physics Letters*, vol. 96, 2010, p. 053308.

[7] A.E. Southard, "Exploration of Novel Methods for the Fabrication and Characterization of Organic Field-effect Transistors and Examination of Factors Influencing OFET Performance," PhD thesis, University of Maryland, College Park, 2009.

[8] A. Yu, "Electron tunneling and contact resistance of metal-silicon contact barriers," *Solid-State Electronics*, vol. 13, Feb. 1970, pp. 239-247.

[9] A.R. Hosseini, M.H. Wong, Y. Shen, and G.G. Malliaras, "Charge injection in doped organic semiconductors," *Journal of Applied Physics*, vol. 97, 2005, p. 023705.

[10] Y.S. Lee, J.H. Park, and J.S. Choi, "Electrical characteristics of pentacene-based Schottky diodes," *Optical Materials*, vol. 21, Jan. 2003, pp. 433-437.

[11] J.G. Laquindanum, H.E. Katz, A.J. Lovinger, and A. Dodabalapur, "Morphological Origin of High Mobility in Pentacene Thin-Film Transistors," *Chemistry of Materials*, vol. 8, Jan. 1996, pp. 2542-2544.

[12] Y. Yamashita, "Organic semiconductors for organic field-effect transistors," *Science and Technology of Advanced Materials*, vol. 10, 2009, p. 024313.

[13] T. Hasegawa and J. Takeya, "Organic field-effect transistors using single crystals," *Science and Technology of Advanced Materials*, vol. 10, 2009, p. 024314.

[14] C.D. Dimitrakopoulos and D.J. Mascaro, "Organic thin-film transistors: A review of recent advances," *IBM Journal of Research and Development*, vol. 45, 2001, p. 11.

[15] M. Kitamura and Y. Arakawa, "Pentacene-based organic field-effect transistors," *Journal of Physics: Condensed Matter*, vol. 20, 2008, p. 184011.

[16] H. Klauk, M. Halik, U. Zschieschang, G. Schmid, W. Radlik, and W. Weber, "High-mobility polymer gate dielectric pentacene thin film transistors," *Journal of Applied Physics*, vol. 92, 2002, p. 5259.

[17] Jyh-Ling Lin, Wen-Jyh Sah, and Si-Chen Lee, "Amorphous-silicon thin-film transistors with very high field-effect mobility," *Electron Device Letters, IEEE*, vol. 12, 1991, pp. 120-121.
[18] O.D. Jurchescu, J. Baas, and T.T.M. Palstra, "Effect of impurities on the mobility of single crystal pentacene," *Applied Physics Letters*, vol. 84, 2004, p. 3061.
[19] S.K. Park, T.N. Jackson, J.E. Anthony, and D.A. Mourey, "High mobility solution processed 6,13-bis(triisopropyl-silylethynyl) pentacene organic thin film transistors," *Applied Physics Letters*, vol. 91, 2007, p. 063514.
[20] E. Gomar-Nadal, B.R. Conrad, W.G. Cullen, and E.D. Willams, "Effect of Impurities on Pentacene Thin Film Growth for Field-Effect Transistors," *The Journal of Physical Chemistry C*, vol. 112, 2008, pp. 5646-5650.
[21] M.E. Gershenson, V. Podzorov, and A.F. Morpurgo, "Colloquium: Electronic transport in single-crystal organic transistors," *Reviews of Modern Physics*, vol. 78, 2006, p. 973.
[22] C.D. Dimitrakopoulos, A.R. Brown, and A. Pomp, "Molecular beam deposited thin films of pentacene for organic field effect transistor applications," *Journal of Applied Physics*, vol. 80, 1996, p. 2501.
[23] F. Meyer zu Heringdorf, M.C. Reuter, and R.M. Tromp, "Growth dynamics of pentacene thin films," *Nature*, vol. 412, 2001, pp. 517-520.
[24] F. Meyer zu Heringdorf, M. Reuter, and R. Tromp, "The nucleation of pentacene thin films," *Applied Physics A: Materials Science & Processing*, vol. 78, Mar. 2004, pp. 787-791.
[25] A.C. Mayer, R. Ruiz, R.L. Headrick, A. Kazimirov, and G.G. Malliaras, "Early stages of pentacene film growth on silicon oxide," *Organic Electronics*, vol. 5, Sep. 2004, pp. 257-263.
[26] R. Ruiz, B. Nickel, N. Koch, L.C. Feldman, R.F. Haglund, A. Kahn, and G. Scoles, "Pentacene ultrathin film formation on reduced and oxidized Si surfaces," *Physical Review B*, vol. 67, Mar. 2003, p. 125406.
[27] R. Ruiz, B. Nickel, N. Koch, L.C. Feldman, R.F. Haglund, A. Kahn, F. Family, and G. Scoles, "Dynamic Scaling, Island Size Distribution, and Morphology in the Aggregation Regime of Submonolayer Pentacene Films," *Physical Review Letters*, vol. 91, 2003, p. 136102.
[28] T.A. Witten and L.M. Sander, "Diffusion-Limited Aggregation, a Kinetic Critical Phenomenon," *Physical Review Letters*, vol. 47, Nov. 1981, p. 1400.
[29] M. Kolb, R. Botet, and R. Jullien, "Scaling of Kinetically Growing Clusters," *Physical Review Letters*, vol. 51, 1983, p. 1123.
[30] M. Muthukumar, "Mean-Field Theory for Diffusion-Limited Cluster Formation," *Physical Review Letters*, vol. 50, Mar. 1983, p. 839.
[31] R. Ruiz, D. Choudhary, B. Nickel, T. Toccoli, K. Chang, A.C. Mayer, P. Clancy, J.M. Blakely, R.L. Headrick, S. Iannotta, and G.G. Malliaras, "Pentacene Thin Film Growth," *Chemistry of Materials*, vol. 16, Nov. 2004, pp. 4497-4508.
[32] S.H. Jin, K.D. Jung, H. Shin, B. Park, and J.D. Lee, "Grain size effects on contact resistance of top-contact pentacene TFTs," *Synthetic Metals*, vol. 156, Feb. 2006, pp. 196-201.

[33] G. Horowitz and M.E. Hajlaoui, “Grain size dependent mobility in polycrystalline organic field-effect transistors,” *Synthetic Metals*, vol. 122, May. 2001, pp. 185-189.
[34] M. Shtein, J. Mapel, J.B. Benziger, and S.R. Forrest, “Effects of film morphology and gate dielectric surface preparation on the electrical characteristics of organic-vapor-phase-deposited pentacene thin-film transistors,” *Applied Physics Letters*, vol. 81, 2002, p. 268.
[35] S.M. Sze and K.K. Ng, *Physics of Semiconductor Devices*, Wiley-Interscience, 2006.
[36] I. Yagi, K. Tsukagoshi, and Y. Aoyagi, “Modification of the electric conduction at the pentacene/SiO_2 interface by surface termination of SiO_2,” *Applied Physics Letters*, vol. 86, 2005, p. 103502.
[37] J.W.H. Smith and I.G. Hill, “Influence of SiO_2 dielectric preparation on interfacial trap density in pentacene-based organic thin-film transistors,” *Journal of Applied Physics*, vol. 101, 2007, p. 044503.
[38] G. Horowitz, R. Hajlaoui, and P. Delannoy, “Temperature Dependence of the Field-Effect Mobility of Sexithiophene. Determination of the Density of Traps,” *Journal de Physique III*, vol. 5, 1995, p. 17.
[39] T. Holstein, “Studies of polaron motion : Part I. The molecular-crystal model,” *Annals of Physics*, vol. 8, Nov. 1959, pp. 325-342.
[40] D. Emin, “Correlated Small-Polaron Hopping Motion,” *Physical Review Letters*, vol. 25, Dec. 1970, p. 1751.
[41] D.R. Lenski, A. Southard, and M.S. Fuhrer, “Frequency-dependent complex conductivity of an organic thin-film transistor,” *Applied Physics Letters*, vol. 94, Jun. 2009, pp. 232103-3.
[42] D. de Leeuw and E. Cantatore, “Organic electronics: Materials, technology and circuit design developments enabling new applications,” *Materials Science in Semiconductor Processing*, vol. 11, Oct. 2008, pp. 199-204.
[43] P.F. Baude, D.A. Ender, M.A. Haase, T.W. Kelley, D.V. Muyres, and S.D. Theiss, “Pentacene-based radio-frequency identification circuitry,” *Applied Physics Letters*, vol. 82, Jun. 2003, pp. 3964-3966.
[44] A. Dodabalapur, “Organic and polymer transistors for electronics,” *Materials Today*, vol. 9, Apr. 2006, pp. 24-30.
[45] S.K. Saha, T.K. Mandal, B.M. Mandal, and D. Chakravorty, “ac conduction in conducting poly pyrrole-poly vinyl methyl ether polymer composite materials,” *Journal of Applied Physics*, vol. 81, Mar. 1997, pp. 2646-2650.
[46] K. Prem Nazeer, M. Thamilselvan, D. Mangalaraj, S.K. Narayandass, and J. Yi, “Direct and High Frequency Alternating Current Conduction Mechanisms in Solution Cast Polyaniline Films,” *Journal of Polymer Research*, vol. 13, Feb. 2006, pp. 17-23.
[47] M. Barra, M. Biasiucci, A. Cassinese, P. D’Angelo, A.C. Barone, A. Carella, and A. Roviello, “Direct current and alternating current electrical transport properties of regioregular poly[3-(4-alkoxyphenyl)-thiophenes],” *Journal of Applied Physics*, vol. 102, 2007, p. 093712.

[48] J.F. Rouleau, J. Goyette, T.K. Bose, R. Singh, and R.P. Tandon, “Transport studies in H3PO4-doped polyaniline,” *Physical Review B*, vol. 52, 1995, p. 4801.
[49] J.C. Dyre, “The random free-energy barrier model for ac conduction in disordered solids,” *Journal of Applied Physics*, vol. 64, 1988, pp. 2456-2468.
[50] T.B. Schrøder and J.C. Dyre, “Scaling and Universality of ac Conduction in Disordered Solids,” *Physical Review Letters*, vol. 84, 2000, pp. 310-313.
[51] A.K. Jonscher, “The 'universal' dielectric response,” *Nature*, vol. 267, Jun. 1977, pp. 673-679.
[52] B.H. Hamadani, C.A. Richter, J.S. Suehle, and D.J. Gundlach, “Insights into the characterization of polymer-based organic thin-film transistors using capacitance-voltage analysis,” *Applied Physics Letters*, vol. 92, 2008, p. 203303.
[53] P. Chow and K. Wang, “A new AC technique for accurate determination of channel charge and mobility in very thin gate MOSFET's,” *Electron Devices, IEEE Transactions on*, vol. 33, Sep. 1986, pp. 1299-1304.
[54] S.J. Zilker, C. Detcheverry, E. Cantatore, and D.M. de Leeuw, “Bias stress in organic thin-film transistors and logic gates,” *Applied Physics Letters*, vol. 79, 2001, p. 1124.
[55] D. Knipp, R.A. Street, A. Völkel, and J. Ho, “Pentacene thin film transistors on inorganic dielectrics: Morphology, structural properties, and electronic transport,” *Journal of Applied Physics*, vol. 93, 2003, p. 347.
[56] J.B. Chang and V. Subramanian, “Effect of active layer thickness on bias stress effect in pentacene thin-film transistors,” *Applied Physics Letters*, vol. 88, 2006, p. 233513.
[57] M. Matters, D. de Leeuw, P. Herwig, and A. Brown, “Bias-stress induced instability of organic thin film transistors,” *Synthetic Metals*, vol. 102, Jun. 1999, pp. 998-999.
[58] C.M. Osburn and D.W. Ormond, “Dielectric Breakdown in Silicon Dioxide Films on Silicon,” *Journal of The Electrochemical Society*, vol. 119, May. 1972, pp. 591-597.
[59] W. Lerch, G. Roters, P. Münzinger, R. Mader, and R. Ostermeir, “Wet rapid thermal oxidation of silicon with a pyrogenic system,” *Materials Science and Engineering B*, vol. 54, Jun. 1998, pp. 153-160.
[60] P.V. Necliudov, M.S. Shur, D.J. Gundlach, and T.N. Jackson, “Contact resistance extraction in pentacene thin film transistors,” *Solid-State Electronics*, vol. 47, Feb. 2003, pp. 259-262.
[61] G.B. Blanchet, C.R. Fincher, M. Lefenfeld, and J.A. Rogers, “Contact resistance in organic thin film transistors,” *Applied Physics Letters*, vol. 84, 2004, p. 296.
[62] H. Xu, S. Zhang, S.M. Anlage, L. Hu, and G. Grüner, “Frequency- and electric-field-dependent conductivity of single-walled carbon nanotube networks of varying density,” *Physical Review B*, vol. 77, Feb. 2008, p. 075418.
[63] E.W. Montroll and G.H. Weiss, “Random Walks on Lattices. II,” *Journal of Mathematical Physics*, vol. 6, 1965, p. 167.
[64] R.J. Baker and Baker, R. Jacob, *CMOS: Circuit Design, Layout, and Simulation, Third Edition*, Wiley-IEEE, 2011.

[65] P. Blake, E.W. Hill, A.H. Castro Neto, K.S. Novoselov, D. Jiang, R. Yang, T.J. Booth, and A.K. Geim, "Making graphene visible," *Applied Physics Letters*, vol. 91, 2007, p. 063124.
[66] A. Dato, Z. Lee, K. Jeon, R. Erni, V. Radmilovic, T.J. Richardson, and M. Frenklach, "Clean and highly ordered graphene synthesized in the gas phase," *Chemical Communications (Cambridge, England)*, Oct. 2009, pp. 6095-6097.
[67] A.K. Geim and Novoselov, K. S., "The rise of graphene," *Nature Materials*, vol. 6, 2007, pp. 183–191.
[68] K. S. Novoselov, A.K. Geim, S.V. Morozov, D. Jiang, Y. Zhang, S.V. Dubonos, I.V. Grigorieva, and A.A. Firsov, "Electric Field Effect in Atomically Thin Carbon Films," *Science*, vol. 306, Oct. 2004, pp. 666-669.
[69] P.R. Wallace, "The Band Theory of Graphite," *Physical Review*, vol. 71, May. 1947, p. 622.
[70] J. Chen, C. Jang, S. Xiao, M. Ishigami, and M.S. Fuhrer, "Intrinsic and extrinsic performance limits of graphene devices on SiO_2," *Nat Nano*, vol. 3, Apr. 2008, pp. 206-209.
[71] S. Adam, E.H. Hwang, V.M. Galitski, and S. Das Sarma, "A self-consistent theory for graphene transport," *Proceedings of the National Academy of Sciences*, vol. 104, Nov. 2007, pp. 18392 -18397.
[72] J. Chen, C. Jang, S. Adam, M.S. Fuhrer, E.D. Williams, and M. Ishigami, "Charged-impurity scattering in graphene," *Nat Phys*, vol. 4, May. 2008, pp. 377-381.
[73] F. Xia, D.B. Farmer, Y. Lin, and P. Avouris, "Graphene Field-Effect Transistors with High On/Off Current Ratio and Large Transport Band Gap at Room Temperature," *Nano Letters*, vol. 10, Feb. 2010, pp. 715-718.
[74] P. Rhodes, "Fermi-Dirac Functions of Integral Order," *Proceedings of the Royal Society of London. Series A. Mathematical and Physical Sciences*, vol. 204, Dec. 1950, pp. 396 -405.
[75] P. Avouris, Z. Chen, and V. Perebeinos, "Carbon-based electronics," *Nat Nano*, vol. 2, Oct. 2007, pp. 605-615.
[76] A.B. Sproul and M.A. Green, "Improved value for the silicon intrinsic carrier concentration from 275 to 375 K," *Journal of Applied Physics*, vol. 70, 1991, pp. 846–854.
[77] E.H. Hwang, S. Adam, and S. Das Sarma, "Carrier Transport in Two-Dimensional Graphene Layers," *Physical Review Letters*, vol. 98, May. 2007, p. 186806.
[78] M.S. Fuhrer, C.N. Lau, and A.H. MacDonald, "Graphene: Materially Better Carbon," *MRS Bulletin*, vol. 35, Apr. 2010, pp. 289-295.
[79] V. Barone, O. Hod, and G.E. Scuseria, "Electronic Structure and Stability of Semiconducting Graphene Nanoribbons," *Nano Letters*, vol. 6, Dec. 2006, pp. 2748-2754.
[80] K. Nakada, M. Fujita, G. Dresselhaus, and M.S. Dresselhaus, "Edge state in graphene ribbons: Nanometer size effect and edge shape dependence," *Physical Review B*, vol. 54, Dec. 1996, p. 17954.

[81] Y. Son, M.L. Cohen, and S.G. Louie, “Energy Gaps in Graphene Nanoribbons,” *Physical Review Letters*, vol. 97, Nov. 2006, p. 216803.
[82] M.Y. Han, B. Özyilmaz, Y. Zhang, and P. Kim, “Energy Band-Gap Engineering of Graphene Nanoribbons,” *Physical Review Letters*, vol. 98, May. 2007, p. 206805.
[83] X. Wang, Y. Ouyang, X. Li, H. Wang, J. Guo, and H. Dai, “Room-Temperature All-Semiconducting Sub-10-nm Graphene Nanoribbon Field-Effect Transistors,” *Physical Review Letters*, vol. 100, May. 2008, p. 206803.
[84] Y. Zhang, T. Tang, C. Girit, Z. Hao, M.C. Martin, A. Zettl, M.F. Crommie, Y.R. Shen, and F. Wang, “Direct observation of a widely tunable bandgap in bilayer graphene,” *Nature*, vol. 459, Jun. 2009, pp. 820-823.
[85] E. McCann and V.I. Fal'ko, “Landau-Level Degeneracy and Quantum Hall Effect in a Graphite Bilayer,” *Physical Review Letters*, vol. 96, Mar. 2006, p. 086805.
[86] K.S. Novoselov, E. McCann, S.V. Morozov, V.I. Fal'ko, M.I. Katsnelson, U. Zeitler, D. Jiang, F. Schedin, and A.K. Geim, “Unconventional quantum Hall effect and Berry's phase of 2π in bilayer graphene,” *Nat Phys*, vol. 2, Mar. 2006, pp. 177-180.
[87] E. McCann, “Asymmetry gap in the electronic band structure of bilayer graphene,” *Physical Review B*, vol. 74, Oct. 2006, p. 161403.
[88] J.B. Oostinga, H.B. Heersche, X. Liu, A.F. Morpurgo, and L.M.K. Vandersypen, “Gate-induced insulating state in bilayer graphene devices,” *Nat Mater*, vol. 7, Feb. 2008, pp. 151-157.
[89] A.B. Kuzmenko, E. van Heumen, F. Carbone, and D. van der Marel, “Universal Optical Conductance of Graphite,” *Physical Review Letters*, vol. 100, Mar. 2008, p. 117401.
[90] R.R. Nair, P. Blake, A.N. Grigorenko, K.S. Novoselov, T.J. Booth, T. Stauber, N.M.R. Peres, and A.K. Geim, “Fine Structure Constant Defines Visual Transparency of Graphene,” *Science*, vol. 320, Jun. 2008, p. 1308.
[91] K. Nishio, T. Sei, and T. Tsuchiya, “Preparation and electrical properties of ITO thin films by dip-coating process,” *Journal of Materials Science*, vol. 31, 1996, pp. 1761-1766.
[92] Y. Djaoued, V.H. Phong, S. Badilescu, P.V. Ashrit, F.E. Girouard, and V.-. Truong, “Sol-gel-prepared ITO films for electrochromic systems,” *Thin Solid Films*, vol. 293, Jan. 1997, pp. 108-112.
[93] X. Li, Y. Zhu, W. Cai, M. Borysiak, B. Han, D. Chen, R.D. Piner, L. Colombo, and R.S. Ruoff, “Transfer of Large-Area Graphene Films for High-Performance Transparent Conductive Electrodes,” *Nano Letters*, vol. 9, Dec. 2009, pp. 4359-4363.
[94] K.S. Kim, Y. Zhao, H. Jang, S.Y. Lee, J.M. Kim, K.S. Kim, J. Ahn, P. Kim, J. Choi, and B.H. Hong, “Large-scale pattern growth of graphene films for stretchable transparent electrodes,” *Nature*, vol. 457, Feb. 2009, pp. 706-710.
[95] S. Bae, H.K. Kim, X. Xu, J. Balakrishnan, T. Lei, Y.I. Song, Y.J. Kim, B. Ozyilmaz, J. Ahn, B.H. Hong, and S. Iijima, “30-Inch Roll-Based Production of High-Quality Graphene Films for Flexible Transparent Electrodes,” *arXiv:0912.5485*, Dec. 2009.

[96] F. Tuinstra and J.L. Koenig, "Raman Spectrum of Graphite," *The Journal of Chemical Physics*, vol. 53, 1970, p. 1126.
[97] A.C. Ferrari, J.C. Meyer, V. Scardaci, C. Casiraghi, M. Lazzeri, F. Mauri, S. Piscanec, D. Jiang, K.S. Novoselov, S. Roth, and A.K. Geim, "Raman Spectrum of Graphene and Graphene Layers," *Physical Review Letters*, vol. 97, Nov. 2006, pp. 187401-4.
[98] Y. Hao, Y. Wang, L. Wang, Z. Ni, Z. Wang, R. Wang, C.K. Koo, Z. Shen, and J.T.L. Thong, "Probing Layer Number and Stacking Order of Few-Layer Graphene by Raman Spectroscopy," *Small*, vol. 6, 2010, pp. 195-200.
[99] C. Thomsen and S. Reich, "Double Resonant Raman Scattering in Graphite," *Physical Review Letters*, vol. 85, Dec. 2000, p. 5214.
[100] M.S. Dresselhaus, G. Dresselhaus, A. Jorio, A.G. Souza Filho, and R. Saito, "Raman spectroscopy on isolated single wall carbon nanotubes," *Carbon*, vol. 40, 2002, pp. 2043-2061.
[101] P. Poncharal, A. Ayari, T. Michel, and J. Sauvajol, "Raman spectra of misoriented bilayer graphene," *Physical Review B*, vol. 78, 2008, p. 113407.
[102] J. Hass, F. Varchon, J.E. Millán-Otoya, M. Sprinkle, N. Sharma, W.A. de Heer, C. Berger, P.N. First, L. Magaud, and E.H. Conrad, "Why Multilayer Graphene on 4H-SiC(0001-bar) Behaves Like a Single Sheet of Graphene," *Physical Review Letters*, vol. 100, Mar. 2008, p. 125504.
[103] S. Berciaud, S. Ryu, L.E. Brus, and T.F. Heinz, "Probing the Intrinsic Properties of Exfoliated Graphene: Raman Spectroscopy of Free-Standing Monolayers," *Nano Letters*, vol. 9, Jan. 2009, pp. 346-352.
[104] M.A. Pimenta, G. Dresselhaus, M.S. Dresselhaus, L.G. Cançado, A. Jorio, and R. Saito, "Studying disorder in graphite-based systems by Raman spectroscopy," *Physical Chemistry Chemical Physics*, vol. 9, 2007, p. 1276.
[105] B.G. Demczyk, Y.M. Wang, J. Cumings, M. Hetman, W. Han, A. Zettl, and R.O. Ritchie, "Direct mechanical measurement of the tensile strength and elastic modulus of multiwalled carbon nanotubes," *Materials Science and Engineering A*, vol. 334, Sep. 2002, pp. 173-178.
[106] L. Jiao, L. Zhang, X. Wang, G. Diankov, and H. Dai, "Narrow graphene nanoribbons from carbon nanotubes," *Nature*, vol. 458, Apr. 2009, pp. 877-880.
[107] J. Sakamoto, J. van Heijst, O. Lukin, and A. Schlüter, "Two-Dimensional Polymers: Just a Dream of Synthetic Chemists?," *Angewandte Chemie International Edition*, vol. 48, 2009, pp. 1030-1069.
[108] J. Cai, P. Ruffieux, R. Jaafar, M. Bieri, T. Braun, S. Blankenburg, M. Muoth, A.P. Seitsonen, M. Saleh, X. Feng, K. Mullen, and R. Fasel, "Atomically precise bottom-up fabrication of graphene nanoribbons," *Nature*, vol. 466, Jul. 2010, pp. 470-473.
[109] K.V. Emtsev, A. Bostwick, K. Horn, J. Jobst, G.L. Kellogg, L. Ley, J.L. McChesney, T. Ohta, S.A. Reshanov, J. Rohrl, E. Rotenberg, A.K. Schmid, D. Waldmann, H.B. Weber, and T. Seyller, "Towards wafer-size graphene layers by atmospheric pressure graphitization of silicon carbide," *Nat Mater*, vol. 8, Mar. 2009, pp. 203-207.

[110] C. Berger, Z. Song, T. Li, X. Li, A.Y. Ogbazghi, R. Feng, Z. Dai, A.N. Marchenkov, E.H. Conrad, P.N. First, and W.A. de Heer, "Ultrathin Epitaxial Graphite: 2D Electron Gas Properties and a Route toward Graphene-based Nanoelectronics," *The Journal of Physical Chemistry B*, vol. 108, Dec. 2004, pp. 19912-19916.

[111] C. Berger, Z. Song, X. Li, X. Wu, N. Brown, C. Naud, D. Mayou, T. Li, J. Hass, A.N. Marchenkov, E.H. Conrad, P.N. First, and W.A. de Heer, "Electronic Confinement and Coherence in Patterned Epitaxial Graphene," *Science*, vol. 312, May. 2006, pp. 1191-1196.

[112] T. Ohta, F. El Gabaly, A. Bostwick, J.L. McChesney, K.V. Emtsev, A.K. Schmid, T. Seyller, K. Horn, and E. Rotenberg, "Morphology of graphene thin film growth on SiC(0001)," *New Journal of Physics*, vol. 10, 2008, p. 023034.

[113] T. Shen, J.J. Gu, M. Xu, Y.Q. Wu, M.L. Bolen, M.A. Capano, L.W. Engel, and P.D. Ye, "Observation of quantum-Hall effect in gated epitaxial graphene grown on SiC (0001)," *Applied Physics Letters*, vol. 95, Oct. 2009, pp. 172105-172105-3.

[114] A. Tzalenchuk, S. Lara-Avila, A. Kalaboukhov, S. Paolillo, M. Syvajarvi, R. Yakimova, O. Kazakova, JanssenT. J. B. M., V. Fal'ko, and S. Kubatkin, "Towards a quantum resistance standard based on epitaxial graphene," *Nat Nano*, vol. 5, Mar. 2010, pp. 186-189.

[115] J. Jobst, D. Waldmann, F. Speck, R. Hirner, D.K. Maude, T. Seyller, and H.B. Weber, "Quantum oscillations and quantum Hall effect in epitaxial graphene," *Physical Review B*, vol. 81, May. 2010, p. 195434.

[116] J.S. Moon, D. Curtis, M. Hu, D. Wong, C. McGuire, P.M. Campbell, G. Jernigan, J.L. Tedesco, B. VanMil, R. Myers-Ward, and others, "Epitaxial-graphene RF field-effect transistors on Si-face 6H-SiC substrates," *IEEE electron device letters*, vol. 30, Jun. 2009, pp. 650–652.

[117] Y. Lin, C. Dimitrakopoulos, K.A. Jenkins, D.B. Farmer, H. Chiu, A. Grill, and P. Avouris, "100-GHz Transistors from Wafer-Scale Epitaxial Graphene," *Science*, vol. 327, Feb. 2010, p. 662.

[118] C. Oshima and A. Nagashima, "Ultra-thin epitaxial films of graphite and hexagonal boron nitride on solid surfaces," *Journal of Physics: Condensed Matter*, vol. 9, Jan. 1997, p. 1.

[119] P.W. Sutter, J. Flege, and E.A. Sutter, "Epitaxial graphene on ruthenium," *Nat Mater*, vol. 7, May. 2008, pp. 406-411.

[120] S.G. Wang, E.K. Tian, and C.W. Lung, "Surface energy of arbitrary crystal plane of bcc and fcc metals," *Journal of Physics and Chemistry of Solids*, vol. 61, Aug. 2000, pp. 1295-1300.

[121] H.T. Jeong, S.D. Park, and T.K. Ha, "Evolution of shear texture according to shear strain ratio in rolled FCC metal sheets," *Metals and Materials International*, vol. 12, 2006, pp. 21-26.

[122] Y. Lee, S. Bae, H. Jang, S. Jang, S. Zhu, S.H. Sim, Y.I. Song, B.H. Hong, and J. Ahn, "Wafer-Scale Synthesis and Transfer of Graphene Films," *Nano Letters*, vol. 10, Feb. 2010, pp. 490-493.

[123] K. Asai, K. Takane, Y. Nagayasu, S. Iwamoto, E. Yagasaki, and M. Inoue, "Decomposition of methane in the presence of carbon dioxide over Ni catalysts," *Chemical Engineering Science*, vol. 63, Oct. 2008, pp. 5083-5088.
[124] W. Zhou, Z. Han, J. Wang, Y. Zhang, Z. Jin, X. Sun, Y. Zhang, C. Yan, and Y. Li, "Copper Catalyzing Growth of Single-Walled Carbon Nanotubes on Substrates," *Nano Letters*, vol. 6, Dec. 2006, pp. 2987-2990.
[125] X. Li, W. Cai, L. Colombo, and R.S. Ruoff, "Evolution of Graphene Growth on Ni and Cu by Carbon Isotope Labeling," *Nano Letters*, vol. 9, Dec. 2009, pp. 4268-4272.
[126] X. Li, W. Cai, J. An, S. Kim, J. Nah, D. Yang, R. Piner, A. Velamakanni, I. Jung, E. Tutuc, S.K. Banerjee, L. Colombo, and R.S. Ruoff, "Large-Area Synthesis of High-Quality and Uniform Graphene Films on Copper Foils," *Science*, vol. 324, Jun. 2009, pp. 1312-1314.
[127] S. Fan, L. Liu, and M. Liu, "Monitoring the growth of carbon nanotubes by carbon isotope labelling," *Nanotechnology*, vol. 14, 2003, pp. 1118-1123.
[128] L.G. De Arco, Y. Zhang, A. Kumar, and C. Zhou, "Synthesis, Transfer and Devices of Single- and Few-Layer Graphene by Chemical Vapor Deposition," *IEEE Transactions on Nanotechnology*, 2009.
[129] A. Reina, X. Jia, J. Ho, D. Nezich, H. Son, V. Bulovic, M.S. Dresselhaus, and J. Kong, "Large Area, Few-Layer Graphene Films on Arbitrary Substrates by Chemical Vapor Deposition," *Nano Letters*, vol. 9, Jan. 2009, pp. 30-35.
[130] W. Liu, C. Chung, C. Miao, Y. Wang, B. Li, L. Ruan, K. Patel, Y. Park, J. Woo, and Y. Xie, "Chemical vapor deposition of large area few layer graphene on Si catalyzed with nickel films," *Thin Solid Films*, vol. In Press, Corrected Proof.
[131] Q. Yu, J. Lian, S. Siriponglert, H. Li, Y.P. Chen, and S. Pei, "Graphene segregated on Ni surfaces and transferred to insulators," *Applied Physics Letters*, vol. 93, 2008, p. 113103.
[132] A. Reina, S. Thiele, X. Jia, S. Bhaviripudi, M. Dresselhaus, J. Schaefer, and J. Kong, "Growth of large-area single- and Bi-layer graphene by controlled carbon precipitation on polycrystalline Ni surfaces," *Nano Research*, vol. 2, Jun. 2009, pp. 509-516.
[133] H.J. Park, J. Meyer, S. Roth, and V. Skákalová, "Growth and properties of few-layer graphene prepared by chemical vapor deposition," *Carbon*, vol. 48, Apr. 2010, pp. 1088-1094.
[134] H. Cao, Q. Yu, L.A. Jauregui, J. Tian, W. Wu, Z. Liu, R. Jalilian, D.K. Benjamin, Z. Jiang, J. Bao, S.S. Pei, and Y.P. Chen, "Electronic transport in chemical vapor deposited graphene synthesized on Cu: Quantum Hall effect and weak localization," *Applied Physics Letters*, vol. 96, 2010, p. 122106.
[135] X. Li, W. Cai, J. An, S. Kim, J. Nah, D. Yang, R. Piner, A. Velamakanni, I. Jung, E. Tutuc, S.K. Banerjee, L. Colombo, and R.S. Ruoff, "Large-Area Synthesis of High-Quality and Uniform Graphene Films on Copper Foils," *Science*, vol. 324, Jun. 2009, pp. 1312-1314.

[136] H. Scheibe, D. Drescher, and P. Alers, “Raman characterization of amorphous carbon films,” *Fresenius' Journal of Analytical Chemistry*, vol. 353, 1995, pp. 695-697.
[137] K.S. Novoselov, A.K. Geim, S.V. Morozov, D. Jiang, Y. Zhang, S.V. Dubonos, I.V. Grigorieva, and A.A. Firsov, “Electric Field Effect in Atomically Thin Carbon Films,” *Science*, vol. 306, Oct. 2004, pp. 666-669.
[138] B. Sernelius, “Lecture Notes 13 for Electrodynamics: Reflection from a metallic surface,” Feb. 2005.
[139] E. Hecht, *Optics*, Addison Wesley, 2001.
[140] E.D. Palik, Ed., *Handbook of Optical Constants of Solids*, Academic Press, 1991.
[141] Z.H. Ni, H.M. Wang, J. Kasim, H.M. Fan, T. Yu, Y.H. Wu, Y.P. Feng, and Z.X. Shen, “Graphene Thickness Determination Using Reflection and Contrast Spectroscopy,” *Nano Letters*, vol. 7, 2007, pp. 2758-2763.
[142] X. Wang, Y.P. Chen, and D.D. Nolte, “Strong anomalous optical dispersion of graphene: complex refractive index measured by Picometrology,” *Optics Express*, vol. 16, Dec. 2008, pp. 22105-22112.
[143] H.S. Skulason, P.E. Gaskell, and T. Szkopek, “Optical reflection and transmission properties of exfoliated graphite from a graphene monolayer to several hundred graphene layers,” *Nanotechnology*, vol. 21, 2010, p. 295709.
[144] A. Gupta, G. Chen, P. Joshi, S. Tadigadapa, and Eklund, “Raman Scattering from High-Frequency Phonons in Supported n-Graphene Layer Films,” *Nano Letters*, vol. 6, Dec. 2006, pp. 2667-2673.
[145] D. Olsen, C. Dou, X. Zhang, L. Hu, H. Kim, and E. Hildum, “Radiometric Calibration for AgCam,” *Remote Sensing*, vol. 2, 2010, pp. 464–477.
[146] X. Wang, M. Zhao, and D.D. Nolte, “Optical contrast and clarity of graphene on an arbitrary substrate,” *Applied Physics Letters*, vol. 95, 2009, p. 081102.
[147] F. Pallikari, G. Chondrokoukis, M. Rebelakis, and Y. Kotsalas, “Raman spectroscopy: A technique for estimating extent of polymerization in PMMA,” *Materials Research Innovations*, vol. 4, 2001, pp. 89-92.
[148] R. Saito, A. Grüneis, G.G. Samsonidze, V.W. Brar, G. Dresselhaus, M.S. Dresselhaus, A. Jorio, L.G. Cançado, C. Fantini, M.A. Pimenta, and A.G.S. Filho, “Double resonance Raman spectroscopy of single-wall carbon nanotubes,” *New Journal of Physics*, vol. 5, 2003, pp. 157-157.
[149] D.L. Mafra, G. Samsonidze, L.M. Malard, D.C. Elias, J.C. Brant, F. Plentz, E.S. Alves, and M.A. Pimenta, “Determination of LA and TO phonon dispersion relations of graphene near the Dirac point by double resonance Raman scattering,” *Physical Review B*, vol. 76, Dec. 2007, p. 233407.
[150] S. Piscanec, M. Lazzeri, F. Mauri, A.C. Ferrari, and J. Robertson, “Kohn Anomalies and Electron-Phonon Interactions in Graphite,” *Physical Review Letters*, vol. 93, Oct. 2004, p. 185503.
[151] I. Calizo, A.A. Balandin, W. Bao, F. Miao, and C.N. Lau, “Temperature Dependence of the Raman Spectra of Graphene and Graphene Multilayers,” *Nano Letters*, vol. 7, 2007, pp. 2645-2649.

[152] C. Casiraghi, S. Pisana, K.S. Novoselov, A.K. Geim, and A.C. Ferrari, "Raman fingerprint of charged impurities in graphene," *Applied Physics Letters*, vol. 91, 2007, p. 233108.
[153] C. Faugeras, A. Nerrière, M. Potemski, A. Mahmood, E. Dujardin, C. Berger, and W.A. de Heer, "Few-layer graphene on SiC, pyrolitic graphite, and graphene: A Raman scattering study," *Applied Physics Letters*, vol. 92, 2008, p. 011914.
[154] J.A. Robinson, M. Wetherington, J.L. Tedesco, P.M. Campbell, X. Weng, J. Stitt, M.A. Fanton, E. Frantz, D. Snyder, B.L. VanMil, G.G. Jernigan, R.L. Myers-Ward, C.R. Eddy, and D.K. Gaskill, "Correlating Raman Spectral Signatures with Carrier Mobility in Epitaxial Graphene: A Guide to Achieving High Mobility on the Wafer Scale," *Nano Letters*, vol. 9, 2009, pp. 2873-2876.
[155] P. Nemes-Incze, Z. Osváth, K. Kamarás, and L. Biró, "Anomalies in thickness measurements of graphene and few layer graphite crystals by tapping mode atomic force microscopy," *Carbon*, vol. 46, Sep. 2008, pp. 1435-1442.

DANIEL R. LENSKI

lenski@umd.edu · (301) 375-0586
8306 49th Ave, College Park, MD 20740

Education

University of Maryland, Department of Physics 2003-2010
Title of PhD dissertation: "Materials for large-area electronics: Characterization of pentacene and graphene thin films by ac transport, Raman spectroscopy, and optics"

Cornell University, College of Arts and Sciences 1999-2003
Bachelor of Arts in Physics and Linguistics, *cum laude*

Work experience

University of Maryland Department of Physics, College Park, MD 2003-2010
Research Assistant

- Construct and analyze semiconductor devices using novel organic materials (graphene, carbon nanotubes, and organic semiconductors)
- Collaboratively develop device models, write and publish peer-reviewed articles, and share expertise and materials with colleagues
- Regularly present results to local colleagues and larger audiences at national conferences
- Maintain scanning electron microscope (Philips XL-30) for Maryland physics department

The Princeton Review, Washington, DC 2007-2010
Physics and Math Teacher

- Teach physics review course to pre-med students preparing for MCAT exam
- Rapidly communicate challenging concepts in clear, intuitive, memorable ways
- Regularly receive superlative evaluations from students
- Selected for superior performance to teach courses around East Coast and Puerto Rico

Seagate Technology, Pittsburgh, PA 2008
Research and Development Intern

- Initiated and developed software to visualize models of magnetic write heads
- Trained colleagues in the use of these tools (since adopted by others at Seagate)
- Researched and simulated magnetic write head structures to improve future hard drive performance and miniaturization
- Designed, tested, and ran hard drive write head simulations on parallel computer cluster
- Extensively used, developed, and debugged Magpar micromagnetics software

SpeechWorks, Inc., Ithaca, NY 2001-2002
Programmer

- Profiled, optimized, and debugged speech synthesis software engine, resulting in net 30% performance gain in 2 months
- Created software for design and evaluation of speech synthesis quality
- Supported manager in assessing feasibility and quality of significantly different synthesis techniques proposed for the long-term evolution of our product

(cont.)

Cornell University Department of Physics, Ithaca, NY 2002-2003
Undergraduate Teaching Assistant

- Taught introductory mechanics, electricity and magnetism, and waves and optics
- Assisted students with homework and laboratory questions for 5-10 hours per week
- Prepared laboratory experiments and guided students in carrying them out
- Graded quizzes and exams and reviewed problematic material with students

Other experience

Course project for "Industrial Research in Data-Storage Technology" 2007

- Final paper, "Flash memory as a competitor to hard disk drives," presented to storage industry executives. I addressed technical challenges to continued miniaturization and cost-per-bit reduction for both magnetic and solid-state devices. Based on cost scaling, I predicted a division of the storage market between high-capacity magnetic drives and embedded solid-state storage over the next 5 years.

Course projects for "Digital Electronics Design" 2007

- This course covered digital electronics design using electronics development boards based on Altera FPGAs, and the Verilog hardware definition language. Among other projects, I implemented a pipelined 32-bit RISC CPU with several integrated peripherals.

Course project for "Graduate Electronics Laboratory" 2005

- Designed, built, and programmed a low-noise digital micro-voltmeter. My device was based on a microcontroller and high-precision operational amplifier. Since no affordable programming hardware was available, I also built an EEPROM programmer and wrote software to operate it under Linux. I tested my design and documented it in a final paper.

Techniques and skills

- Micromagnetic design and simulation using Magpar software
- Semiconductor fabrication, including thermal and electron-beam evaporation, electron-beam lithography, photolithography, chemical vapor deposition, and RF sputtering
- Semiconductor analysis and characterization, including DC and AC transport measurements, automated probe station operation, GPIB control and automation of laboratory instruments, and high vacuum system design and maintenance
- Digital electronics design, including AVR and PIC microcontrollers and Altera FPGAs
- Microscopy, including optical microscopy, atomic force microscopy, Raman spectroscopy, scanning electron microscopy, and transmission electron microscopy
- Programming languages: Python, Perl, C, C++, Verilog, x86 and MIPS assembly
- Mathematical and numerical software: Numeric Python and Scientific Python (NumPy/SciPy), MATLAB, ParaView, Mathematica
- Machine tool operation (mill and lathe)
- Foreign languages: fluent in French, proficient in Spanish

Publications

- *In preparation:* D. R. Lenski and M. S. Fuhrer. "Raman and optical characterization of multilayer turbostratic graphene grown via chemical vapor deposition."

(cont.)

- D. R. Lenski, A. Southard, and M. S. Fuhrer. "Frequency-dependent complex conductivity of an organic thin-film transistor." *Applied Physics Letters* **94.23** (2009): 232103-3.
- H. Pandana, K. H. Aschenbach, D. R. Lenski, M. S. Fuhrer, J. Khan, and R. D. Gomez. "A Versatile Biomolecular Charge-Based Sensor Using Oxide-Gated Carbon Nanotube Transistor Arrays." *Sensors Journal, IEEE* **8.6** (2008): 655-660.

Conference presentations

- D. R. Lenski and M. S. Fuhrer, "Growth of multi-layer turbostratic graphene on copper by ambient-pressure chemical vapor deposition," *Graphene Week, April 19-23*, 2010.
- D. R. Lenski and M. S. Fuhrer, "Raman study of turbostratic graphene grown via chemical vapor deposition on metals," *American Physical Society, APS March Meeting 2010, March 15-19, 2010, abstract #W20.006*, 2010.
- D. R. Lenski, A. Southard, and M. S. Fuhrer, "RC Transmission Line Characterization of Organic Semiconductors," *American Physical Society, APS March Meeting, March 16-20, 2009, abstract# L19.011*, 2009.
- D. R. Lenski, A. Southard, and M. S. Fuhrer, "Impedance Spectroscopy of Organic Thin Film Transistors and Contacts," *American Physical Society, 2008 APS March Meeting, March 10-14, 2008, abstract# S22.008*, 2008.
- D. R. Lenski, A. Southard, and M. S. Fuhrer, "RC Transmission Line Characterization of Organic Thin Film Transistors," *American Physical Society, APS March Meeting, March 5-9, 2007, abstract# U25.002*, 2007.
- D. R. Lenski, A. Curtin, and M. S. Fuhrer, "Thermopower of Pentacene Thin-film Transistors," *American Physical Society, APS March Meeting, March 13-17, 2006, abstract# W28.012*, 2006.

Leadership and activities

Homeless Children's Playtime project volunteer 2010-present

- Supervise children and provide a structured play environment at a local homeless shelter, for 2 hours each week

Distance running 2009-present

- Qualified for the Boston Marathon
- Marathon personal best: 2:54:10 (Marine Corps Marathon, October 2009)
- Ten mile personal best: 58:31 (Cherry Blossom Ten Miler, April 2010)

Cycling 2004-present

- Active member of Potomac Pedalers road cycling club
- Bicycle commuter and advocate for over 6 years
- Have built, repaired, or restored over 10 bicycles

Alpha Phi Omega service fraternity, Gamma chapter 2001-2003
New Member Coordinator, 2003

- Successfully led recruitment, training, and induction of approximately 20 new members
- Volunteered 20-30 hours per semester in local community service projects